REALISTIC MICROMECHANICAL MODELING AND SIMULATION OF TWO-PHASE HETEROGENEOUS MATERIALS

A Dissertation
Presented to
The Academic Faculty

by

Arun Sreeranganathan

In Partial Fulfillment
of the Requirements for the Degree
Doctor of Philosophy in the
School of Materials Science and Engineering

Georgia Institute of Technology
August 2008

REALISTIC MICROMECHANICAL MODELING AND SIMULATION OF TWO-PHASE HETEROGENEOUS MATERIALS

Approved by:

Dr. Arun M. Gokhale, Advisor
School of Materials Science & Engineering
Georgia Institute of Technology

Dr. Kimberly E. Kurtis
School of Civil & Environmental Engineering
Georgia Institute of Technology

Dr. Kenneth A. Gall
School of Materials Science & Engineering
Georgia Institute of Technology

Dr. Naresh N. Thadhani
School of Materials Science & Engineering
Georgia Institute of Technology

Dr. Hamid Garmestani
School of Materials Science & Engineering
Georgia Institute of Technology

Date Approved: May 12, 2008

To you, the reader, hoping that you will find something useful in these pages

ACKNOWLEDGEMENTS

My time at Georgia Tech as a graduate student has been a great learning experience both as a researcher and as a person, for which I have many to thank.

First of all, my sincere gratitude goes to Professor Arun Gokhale for his invaluable guidance and support in completing this dissertation, for his patience during times when my progress was slow, and for his trust in me. Many in Dr. Gokhale's research group have contributed to this research. Gautam Patel, Joel Harris, Soon Gi Lee, Scott Lieberman, Yuxiong Mao, Harpreet Singh, and Shenjia Zhang deserve mention for their support. I must also thank my committee members, Dr. Ken Gall, Dr. Hamid Garmestani, Dr. Kimberly Kurtis, and Dr. Naresh Thadhani for their guidance and support. Dr. Ken Gall has been extremely helpful, providing me with access to his nano-indentation equipment and guiding me whenever I had questions related to instrumented indentation.

This work would not have been possible without the knowledge I gained through attending classes taught by some remarkable teachers in Georgia Tech, including, but not limited to, Dr. Arun Gokhale, Dr. David McDowell, Dr. Jianmin Qu, Dr. James Craig, Dr. Hamid Garmestani, and Dr. Naresh Thadhani. Thanks are also due to numerous others in the Georgia Tech community: Scott Kasprzak for help with nano-indentation, Susan Bowman who always seemed to have the information that I needed at her fingertips, and other MSE staff including Jasmin Frett-Hodge, Jyoti Ghosh, Mechelle Kitchings, and Marlene White, who have helped with administrative dealings.

Financial support for this research came through research grants from Air Force Office of Scientific Research (AFOSR grant numbers FA95550-05-1-0062 and F49620-01-1-0045), and Division of Materials Research, U.S. National Science Foundation (NSF grant number DMR0404668). The support is gratefully acknowledged. I am thankful to Dr. Seshacharyulu Tamirisakandala and Dr. Jonathan Spowart at the Air Force Research Laboratory for providing some of the experimental results given in this dissertation. This work was also partially supported by the National Center for Supercomputing Applications under TG-DMR070047N and utilized the SGI Altix cluster, Cobalt.

This research has benefited greatly by help from unexpected sources whom I have been fortunate to meet during technical conferences. Dr. Seid Koric at National Center for Supercomputing Applications, UIUC who expedited my application for the use of computational resources at NCSA to run the large-scale 3D simulations carried out in this research deserves special mention. I am also grateful to Dr. Philippe Young at Exeter University, UK for providing me with a trial version of the finite element meshing software, Simpleware, which has been used in this research.

Most importantly, I thank my wife, Sreeja, for the unflinching trust and love she has bestowed upon me from the day we met. I would also like to thank my parents and my brother back home who have been very supportive throughout my life. Finally, I thank all of my family members, friends, and strangers who have knowingly or unknowingly helped me on the way.

TABLE OF CONTENTS

LIST OF TABLES

Page

LIST OF FIGURES

Page

SUMMARY

This dissertation research focuses on micromechanical modeling and simulations of two-phase heterogeneous materials exhibiting anisotropic and non-uniform microstructures with long-range spatial correlations. Completed work involves development of methodologies for realistic micromechanical analyses of materials using a combination of stereological techniques, two- and three-dimensional digital image processing, and finite element based modeling tools. The methodologies are developed via its applications to two technologically important material systems, namely, discontinuously reinforced aluminum composites containing silicon carbide particles as reinforcement, and boron modified titanium alloys containing *in situ* formed titanium boride whiskers. Microstructural attributes such as the shape, size, volume fraction, and spatial distribution of the reinforcement phase in these materials were incorporated in the models without any simplifying assumptions. Instrumented indentation was used to determine the constitutive properties of individual microstructural phases. Micromechanical analyses were performed using realistic 2D and 3D models and the results were compared with experimental data. Results indicated that 2D models fail to capture the deformation behavior of these materials and 3D analyses are required for realistic simulations. The effect of clustering of silicon carbide particles and associated porosity on the mechanical response of discontinuously reinforced aluminum composites was investigated using 3D models. Parametric studies were carried out using computer simulated microstructures incorporating realistic microstructural attributes. The intrinsic merit of this research is the development and integration of the required enabling

techniques and methodologies for representation, modeling, and simulations of complex geometry of microstructures in two- and three-dimensional space facilitating better understanding of the effects of microstructural geometry on the mechanical behavior of materials. The methodologies developed in this research are applicable to a wide variety of heterogeneous materials such as metal matrix composites, cast alloys with randomly distributed porosity, ceramics with controlled porosity, and concrete, to name a few.

CHAPTER 1

INTRODUCTION

1.1 Motivation, Rationale and Objectives

Modeling and simulation of the mechanical response of materials with complex microstructures is a challenging multi-scale problem requiring expertise in a wide range of fields ranging from quantum mechanics to continuum mechanics depending on the length scale that is being studied. This dissertation research focuses on a small segment of the problem, namely the linking of micro-macro scales where continuum mechanics theories are assumed to be valid. An entire branch of mechanics of materials, named micromechanics, is devoted to the development and use of analytical and numerical methods to predict the macroscopic mechanical behavior of heterogeneous materials such as composites from an understanding of their microstructure. The origin of micromechanics as a rigorous scientific field of study may be traced back to the pioneering work by Eshelby, who analytically determined the elastic state of a system containing an ellipsoidal inhomogeneity in an infinite domain [1].

Microstructural attributes such as the shape, size, volume fraction, and spatial distribution of the reinforcement phase are known to directly affect the macroscopic behavior of composite materials. A large number of permutations of these attributes exist for composites enabling the tailorability of properties for such materials. Consequently, the primary objective of micromechanics is to develop predictive models for the macroscopic behavior of composite materials so as to reduce the need for physical experimentation. While analytical models developed by Eshelby, Mori, Tanaka, and

others have paved the way in this direction [2], such closed-form solutions often require simplifying assumptions about shape, size, and spatial distribution of microstructural phases. For realistic prediction of the macroscopic behavior of composite materials, it is imperative that no such simplifying assumptions are made in the model. Advancements in numerical modeling tools such as finite element method (FEM) have led to their widespread use as an alternative to analytical models. Sophisticated and efficient models to simulate realistic material behavior continue to be developed in this area of active research. Though numerous studies have been reported in the literature on the incorporation of realistic microstructures in micromechanical models, almost all such studies involve isotropic uniform random microstructures. But a number of widely used composite material systems exhibit controlled anisotropy and spatial non-uniformity depending on the desired behavior for the end product. Consequently, it is of interest to develop methodologies for realistic micromechanical modeling of such anisotropic non-uniform microstructures.

The key factor identified in this dissertation as a requirement for realistic modeling of heterogeneous material systems is the incorporation of microstructural attributes such as the shape, size, volume fraction, and spatial distribution (e.g., anisotropy, non-uniformity, short- and long-range spatial correlations) of the reinforcement phase in the models without any simplifying assumptions. Extensive and innovative use of image analysis tools, statistical descriptors, and finite element modeling tools are required for achieving this goal. Completed work involves development of methodologies for realistic micromechanical analyses of materials using a combination of stereological techniques, two- and three-dimensional digital image processing, and finite

element based modeling tools. The methodologies are developed via its applications to two technologically important material systems exhibiting anisotropic and/or non-uniform microstructures, namely, discontinuously reinforced aluminum (DRA) composites containing silicon carbide (SiC) particles as reinforcement, and boron modified titanium alloys containing *in situ* formed titanium boride (TiB) whiskers. The specific tasks completed in the present research are as follows:

- Determination of constitutive properties of individual phases in the microstructure using instrumented indentation as phenomenological constitutive properties data such as those obtained from standard tensile test are not always available and/or applicable for micromechanical studies
- Systematic selection of a representative volume element (RVE) for the micromechanical models taking into account the short-range and long-range heterogeneities of the microstructure under consideration
- Incorporation of realistic 2D and 3D microstructures in finite element based simulations of uniaxial loading of these materials
- Parametric studies using realistic microstructures to enable materials design

1.2 Organization of Thesis

This thesis is organized in such a way that each chapter, for the most part, is self-contained and focuses on a specific aspect of the research. Chapter 2 summarizes the state of the art in the fields related to this research. While the emphasis is on the incorporation of realistic microstructural models in finite element based micromechanical studies, the reader is also introduced to the material systems under investigation, two-point correlation functions, and the use of instrumented indentation for determining the

constitutive properties of small microstructural volumes. Chapter 3 details the instrumented indentation experiments and simulations performed as a part of this research to determine the constitutive properties of the different microstructural phases in the material systems under study. Two- and three-dimensional finite element based micromechanical analyses of realistic microstructural models are described in chapters 4 and 5, respectively. These chapters include detailed description of methodologies developed for the systematic selection of RVE in both 2D and 3D space, along with the finite element analyses results and comparison with experimental data. In chapter 6, parametric studies conducted using realistic virtual microstructures are discussed, demonstrating the potential of simulation techniques developed at the author's group at Georgia Tech in achieving true computational based material design and development. Finally, chapter 7 concludes this thesis with a summary of the completed research and recommendations for future work.

CHAPTER 2

BACKGROUND AND LITERATURE REVIEW

2.1 Introduction

Correlation of material microstructures with their macroscopic properties is of fundamental importance to materials scientists for understanding the vast spectrum of existing materials as well as for developing new materials. Material microstructures, often a complex ensemble of defects and multiple phases resulting from the processing of the material, directly affect the properties and thereby, the usability of the material. This microstructure-properties relationship is also of interest to researchers working in various other disciplines such as civil engineering, geology, pathology, etc. Accordingly, quantitative characterization and modeling of microstructures are becoming increasingly important in all of these disciplines due to the thrust towards accurate prediction of materials behavior under external stimuli and the design of new materials with desired properties. In this aspect, computational micromechanics, which deals with computer based numerical modeling of the mechanical behavior of structural materials based on their microstructures, has garnered significant interest among researchers. The current research is primarily aimed at developing and integrating microstructure-based computational methodologies for the modeling and simulation of deformation behavior of two-phase heterogeneous materials.

2.2 Microstructure Length Scales

The mechanical response of materials to external stimuli is dictated by a multitude of microstructural features, and interactions among them, spanning over length scales

ranging from a few nanometers to meters. Various classification schemes are suggested in the literature to describe the length scales involved, depending on the microstructural attributes that are significant at each stage [3-5]. In general, the length scales in a microstructure can be divided into nano- (atomic bonds, molecular dynamics), micro- (inclusions, particles) and macro-levels (component size). Features with characteristic lengths intermediate to these levels have been identified as meso-level in more detailed classification schemes. Schmauder, for instance, has suggested using meso-I level for representing intermediate features between nano- and micro-levels and meso-II level for features with characteristic length scales in between micro- and macro-levels [3]. Needleman defined the mesoscale as the length scale ranging from a fraction of a micrometer to 100μm or so [6]. The existence of this microstructural hierarchy across wide length scales makes it difficult to use a single approach for modeling of material microstructures. Figure 2.1 shows the classification of length scales in a typical structural material and some of the common numerical methods used for modeling the material behavior at each stage.

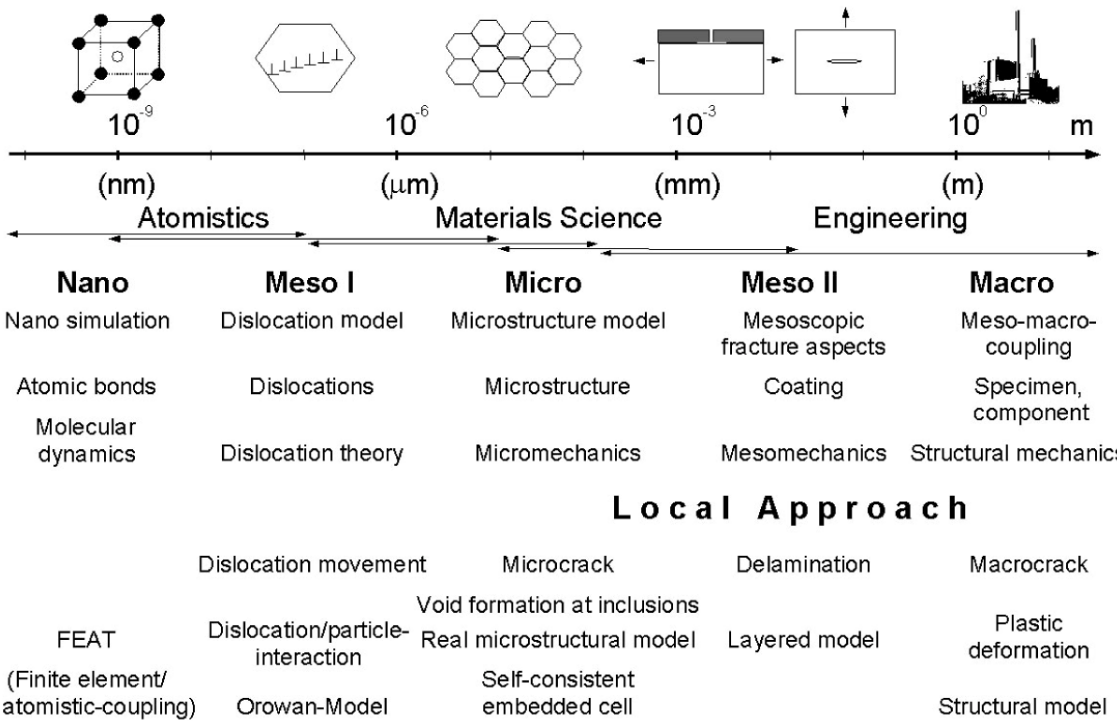

Figure 2.1: Classification of length scales in a typical structural material (Reprinted from [3], with permission from Annual Reviews)

The idea of continuum is nothing but a practical approximation which breaks down for all materials at some point of length scale. At the nanometer or atomistic level, quantum mechanical descriptions are necessary to accurately model the material behavior. But at much larger engineering length scales, a continuum approach is preferred as it is impractical to inflate the atomistic models to the component level. The challenge in any computational materials approach therefore lies in identifying an accurate method to model the material behavior at each length scale as well as linkage of these models without any contradictions. A multiscale sequential modeling approach, where the material input data for each stage is obtained from the detailed modeling at a smaller length scale, has been proved successful for materials where the deformation behavior can be distinctly characterized at different length scales [7-9]. From a structural

point of view, the macroscopic properties of a given material are most easily influenced by the geometric and spatial attributes of microstructural features in the micro-level (grain size, spatial distribution of second phase particles, etc.). The prediction of macroscopic mechanical constitutive behavior based on the microscale attributes of a material, the so-called 'homogenization' procedure, has been an area of intensive research for the last several decades. Homogenization techniques, aimed at replacing an actual inhomogeneous complex body by a fictitious homogeneous one which behaves globally in the same way, dates back to 1887 when the first "rule of mixtures" was proposed by Voight to predict the average elastic moduli of a linearly elastic composite [10, 11]. Under the assumption of a uniform strain in all the constituents of the composite material, he analytically determined the overall moduli and overall compliances of the composite. A uniform stress approach was proposed by Reuss in 1929 to obtain the average moduli of composite materials [11]. Hill pointed out that the Voight approximation and the Reuss approximation are in fact the upper and lower bounds of the true average elastic moduli [12, 13]. A number of other analytical bounds and estimates have been proposed over the years, details of which can be found elsewhere [11, 14]. The advent of advanced composite materials in 1960s fueled a renewed interest in the homogenization techniques resulting in the foundation of the field 'continuum micromechanics' which aimed at obtaining improved estimates for the overall mechanical behavior as well as the microscale behavior of heterogeneous materials. A homogenization theory based on more rigorous mathematical foundations was proposed in the 1970s. Based on the method of two-scale asymptotic expansion, this homogenization theory allowed for the derivation of effective properties of a

heterogeneous material as well as the local micromechanical properties from an overall structural response. These processes are respectively called homogenization and localization. Detailed mathematical derivations of the theory and its application to various systems of governing equations can be found in [15]. Through the use of asymptotic series expansions in ε, a scale parameter, of stress and displacement fields, the homogenization techniques allow for the coupling of micro- and macroscopic levels. The scale parameter ε is a ratio between the characteristic length scale in the micro-scale and macro-scale. In other words, ε represents the length scale of a Representative Volume Element of the microstructure under consideration.

2.2.1 Representative Volume Element

Hill introduced the concept of Representative Volume Element (RVE) in 1963 as a means of systematic transition from the microscale that is heterogeneous in nature to the homogeneous macroscale. He defined an RVE as a sample that (a) is structurally entirely typical of the whole mixture on average, and (b) contains a sufficient number of inclusions for the apparent overall moduli to be effectively independent of the surface values of traction and displacement, so long as these values are 'macroscopically uniform.' That is, they fluctuate about a mean with a wavelength small compared with the dimensions of the sample, and the effects of such fluctuations become insignificant within a few wavelengths of the surface. The contribution of this surface layer to any average can be made negligible by taking the sample large enough [13]. Nemat-Nasser and Hori defined an RVE for a material point of a continuum mass as a material volume which is statistically representative of the infinitesimal material neighborhood of that material point [14]. Accordingly, an RVE must be large enough to include a substantial

number of the microscopic heterogeneities to be a statistical representative of the whole microstructure. At the same time, it should remain small enough to be considered as a volume element of continuum mechanics. Figure 2.2 schematically shows the concept of an RVE for a microscopically heterogeneous material.

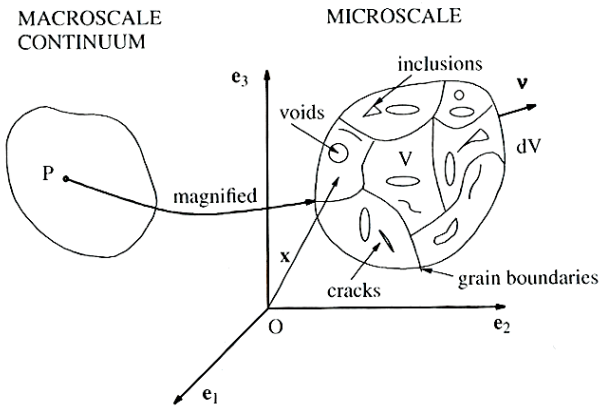

Figure 2.2: Schematic of an RVE for a heterogeneous material (Reprinted from [14], with permission from Elsevier)

According to Drugan and Willis, an RVE is the smallest material volume element of the composite for which the usual spatially constant (overall modulus) macroscopic constitutive representation is a sufficiently accurate model to represent mean constitutive response [16]. Hence the RVE serves as a dividing boundary between continuum theories and microscopic theories. An RVE thus represents the limit of heterogeneity. For scales larger than the RVE, the heterogeneities are smeared out to obtain an equivalent homogeneous medium. This requires that the characteristic length, say *d*, of the micro-constituents under consideration (whose properties and shape are judged to have direct effects on the overall response and properties of the continuum) to be orders of magnitude smaller than the typical dimension, say *D*, of the RVE. Also, for the classical

continuum mechanics principles to apply, D must be sufficiently smaller than the characteristic dimension L of the macroscopic component. Moreover, d should be greater than a lower length bound l_o beyond which the continuum mechanics is no longer valid [10]. Hence, for an RVE to be meaningful

$$l_o << d << D << L \tag{1}$$

It should be noted that only the relative dimensions are of importance here. The absolute dimensions of an RVE could be anything from a few microns to tens of meters depending on the length scale of the heterogeneities in the material under consideration. For example, while an RVE of few microns size might suffice for a material microstructure containing uniform random distribution of sub-micron size inclusions, the RVE for a concrete block might be of the order of tens of centimeters owing to the larger scale heterogeneities present. Unless otherwise specified, the term 'microstructure' in the current research refers to the structure that is observed using an optical microscope with an objective lens magnification of not more than 100x.

The selection of RVE is one among the most important decisions to be made in the modeling of random heterogeneous microstructures. The stochastic behavior of material microstructures must be taken into account while identifying an RVE. Though rigorous mathematical foundations have been laid out for the selection of RVE, most of the reported studies on microstructure modeling, except for a few [17-19], assume without any quantitative studies a unit cell or a single microstructural field of view to be representative of the whole microstructure. This introduces a serious bias in the simulation of microstructures, particularly for those microstructures with long-range heterogeneity that cannot be contained in a single field of view. Consequently, the

simulated mechanical response obtained from such small windows of microstructures may not be representative of the overall mechanical response of the material. Also, it is necessary to consider the local stress/strain distributions and the behavior of the material under different loading directions while choosing an RVE. Most of the reported studies on microstructure modeling consider only the elastic modulus and the global average stress/strain behavior to validate the choice of RVE. Completed research in this dissertation involves systematic selection of RVE for both 2D and 3D microstructures.

2.3 Numerical Analyses of Heterogeneous Material Microstructures

2.3.1 Unit Cell Approach

Developments in the field of finite element method (FEM) for modeling and simulation of material behavior along with the availability of increased computational power in the last few decades have resulted in the use of numerical methods as the preferred approach in micromechanics research. Early numerical analyses of multiphase materials have followed a unit cell approach, which assumes the microstructure to be periodic with repeating unit cells. A simple unit cell model for a continuous fiber reinforced composite contains a round fiber surrounded by a matrix layer, which when analyzed with appropriate periodic boundary conditions gives the overall behavior of the material. The initial studies reported in this field are on fiber-reinforced composites under transverse loading since an inexpensive 2D finite element analysis (FEA) with plane strain elements can mimic the behavior of actual 3D microstructure in this case. Several numerical studies have been reported on the influence of fiber shape and clustering on the transverse mechanical behavior of fiber reinforced composites [20-23]. Adams studied unidirectional boron fiber reinforced aluminum (Al-B) composite using a simple

geometric cell containing the matrix and inclusion with appropriate boundary conditions in finite element framework under plane strain conditions [20]. A rectangular fiber arrangement was shown to be in good agreement with the experimental data. Brockenbrough et al. investigated the effect of different fiber shapes and fiber distributions on longitudinal, transverse, and shear loading behavior of continuous fiber composites [21]. The fiber distribution was found to have an effect only in the plastic regime of the deformation behavior of the composite. They reported that a square arrangement of the fibers represents two extremes of strengthening with the maximum strength occurring when the composite is loaded in a 0^0 direction of the nearest neighbors, and the minimum strength at 45^0 loading. A regular triangular fiber arrangement was found to lie between these limits and best described, though grossly underestimated, the transverse mechanical behavior of a realistic continuous fiber reinforced composite with randomly oriented fibers. They concluded that both the fiber distribution and fiber shape affect the transverse constitutive behavior of the composite but the fiber distribution has a stronger effect at lower volume fractions. Bao and his coworkers used axisymmetric finite element cell models to study the influence of particle volume fraction and shape on the overall behavior of composites containing uniformly distributed, aligned non-deforming reinforcements with identical size and shape in an elastic-plastic matrix [24]. The stress-strain behavior of the matrix material was characterized by elastic-perfectly plastic behavior or by power-law hardening behavior of the Ramberg-Osgood type. They imagined the composite as an array of axisymmetric hexagonal cells each containing a spherical inclusion in the center of the cell. The hexagonal cross section was further approximated by a circle to enable easier analysis. It

was shown that a simple relationship could be obtained to approximate the uniaxial stress-stress behavior of the composite if the matrix material followed a Ramberg-Osgood type power-law hardening behavior. The influence of various significant parameters such as particle volume fraction, shape, and orientation on the overall behavior of particulate reinforced composites has been investigated by several authors [25-27]. Li et al. characterized the flow behavior of Al/SiC_p composites using axisymmetric unit cell models by systematically varying the parameters that they expected to have an effect on the composite behavior namely, volume fraction and aspect ratio of the reinforcement as well as the hardening exponent of the elastic-plastic matrix material [26]. They showed that an empirical equation derived from the FE numerical results could predict the flow behavior of a composite with spherical or cylindrical inclusions. The cylindrical particle was shown to be a far more effective reinforcing agent than the spherical particle. Qin et al. studied the effect of particle shape on ductility of SiC_p reinforced Al6061 composites [27]. 2D models with spherical, hexagon, square, triangle, and shuttle-spaced particles were analyzed using finite element method to show that the particle shape has a great effect on thermal residual stress and strain fields in composites.

The unnatural constraint governing the matrix material between inclusion and simulation cell border, which resulted in an unrealistic strength increase, was pointed out as one of the reasons behind the discrepancy between experiments and calculations based on simple cell models [21, 24]. To overcome this, an embedded cell model where the unit cell is surrounded by additional 'equivalent composite material' was introduced [3, 28, 29] as shown in Figure 2.3.

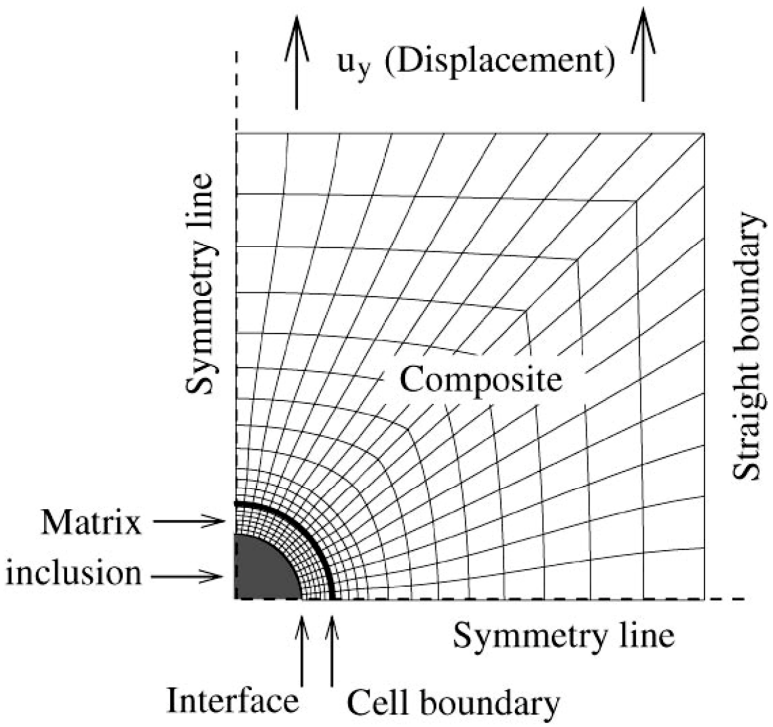

Figure 2.3: Schematic of embedded cell model (Reprinted from [3], with permission from Annual Reviews)

The embedding allows for the effect of the rest of the material on the behavior of the cell. The embedding method is a self-consistent procedure, which requires several iterations. An initially assumed stress-strain curve is first assigned to the embedding composite in order to perform the first iteration. An improved stress-strain curve of the composite will be obtained by analyzing the average mechanical behavior of the embedded cell. This procedure is repeated until the calculated stress-strain curve from the embedded cell is almost identical to that from the previous iteration. It was shown that the convergence of the iteration is reached after 4 to 5 iterations, independent of the initial assumed mechanical behavior of the embedding composite [29]. Farrisey et al. compared the accuracy and efficiency of different analytical and finite element models in predicting the limit flow stress of composite materials reinforced with randomly distributed spherical

particulate inclusions [30]. The modified Oldroyd model proposed by Poech [31], an analytical model which seeks to replace a matrix and inclusion which have undergone both elastic and plastic deformation with a simple elastic system at the same stress and strain, was compared with axisymmetric unit cell model as well as with a 3D embedded finite element model. Two material systems were considered; silver matrix with 58% nickel inclusions representing the case of a soft inclusion in a similarly soft matrix, and martensite-austenite system with 42% austenite in the martensitic matrix representing the case of a hard inclusion in soft matrix. It was shown that the 3D embedded cell model gave a very good approximation of the material behavior in both elastic and plastic regions for the martensite-austenite system. For the Ni-Ag case, none of the models gave a clear prediction of the material behavior but the 3D embedded cell model again gave the closest approximation. The modified Oldroyd model was shown to give a quick and fairly reasonable approximation of the strengthening behavior of composites. Bao developed a micromechanical model for brittle particle reinforced metal matrix composite sustaining damage by implementing an axisymmetric three phase damage cell model, consisting of a cracked particle in a cylindrical matrix cell embedded in an undamaged composite cylinder, in finite element framework [32]. The three phase model allowed for the simulation of material behavior when only few of the particles are cracked, within the convenience of a unit cell model. He developed empirical relationships for limit flow stress of the composite that best fit the numerical results in terms of damaged particle percentage and total volume fraction of particles. Unit cell models with the cells containing more than one inclusion represent a further development in this area [21, 33-36]. These models assume periodic arrangement of fiber/particle

groups as opposed to single fiber/particle in classical unit cell models and thus allow for more realistic modeling of microstructures. Chen and his colleagues, for instance, analyzed unit cell models with 15% vol. SiC particles of different sizes inhomogeneously distributed in Al-6061 matrix to study the effect of particle morphology on mechanical response of composites [35]. Three models were considered with different particle morphologies; angular particles with sharp corners, angular particles with most of the sharp corners deleted, and circular particles. It was shown that while the overall stress-strain curves were quite similar under non-damage assumption, the particle morphology significantly affected the local stress concentration in the material. Largest stresses were observed in the angular particles with sharp corners oriented along the load axis. Segurado et al. studied the effect of reinforcement spatial distribution on uniaxial loading in a metal matrix composite reinforced with 15 vol. % of spheres using 3D FE simulations [37]. Homogeneous microstructures were made up of a random dispersion of spheres. The microstructure of the inhomogeneous materials was idealized as an isotropic random dispersion of spherical regions which represent cluster. They controlled the degree of homogeneity by the local reinforcement volume fraction within each cluster. It was concluded that while the influence of reinforcement clustering on the overall composite behavior was weak, the average maximum principal stress in the spheres were appreciably higher in the inhomogeneous model. Mishnaevsky carried out 3D finite element simulations of the formation and damage evolution of Al/SiC_p composites with random, regular, clustered, and gradient arrangement of SiC particles with spherical geometry [38]. They concluded that the flow stress of the composite and the strain hardening coefficient increase with the varying particle arrangements in the order regular

> clustered > random > gradient microstructures. Shen and Lissenden simulated deformation in Al/SiC_p composite using a multiparticle 3D model artificially generated using 41 idealized 24-faceted particles randomly located and oriented in space [39]. They carried out FE analysis on 2D models as well, obtained from the planar sections through the 3D model. It was reported that while both the 2D and 3D models predicted the same macroscopic stress-strain response, the microscopic stress and strain distributions differed in the two models.

2.3.2 Implementation of Realistic Microstructure Models in FEM

Most of the material microstructures are stochastic in nature, i.e., the microstructures of these materials are almost always random in all three dimensions. Also, the geometry and spatial distribution of phases in a microstructure have been shown to significantly affect the mechanical properties of materials both experimentally [40-43] as well as using FE based parametric studies as discussed earlier. The geometry and spatial distribution of phases in a material microstructure are, in turn, determined by the processing conditions. Hence the approximation of these microstructures as uniform periodic arrangement of second phases in a matrix, though useful for parametric studies, does not allow one to accurately capture the deformation behavior of actual materials. Since the geometric information of a microstructure is often given by a microscopic image, a direct interpretation of the geometry is possible by incorporating this image in microstructure modeling studies. In one among the earliest reported works in this field, Fischmeister and his co-workers studied the effect of the ratio of the hardness of the constituents in a two phase coarse microstructure on the plasticity behavior by discretizing a real 2D microstructure of plain carbon steel (ferrite-martensite) into

triangular finite elements [44]. Figure 2.4 shows the Fe-C microstructure with ferrite and martensite phases and the corresponding finite element model used by Fischmeister.

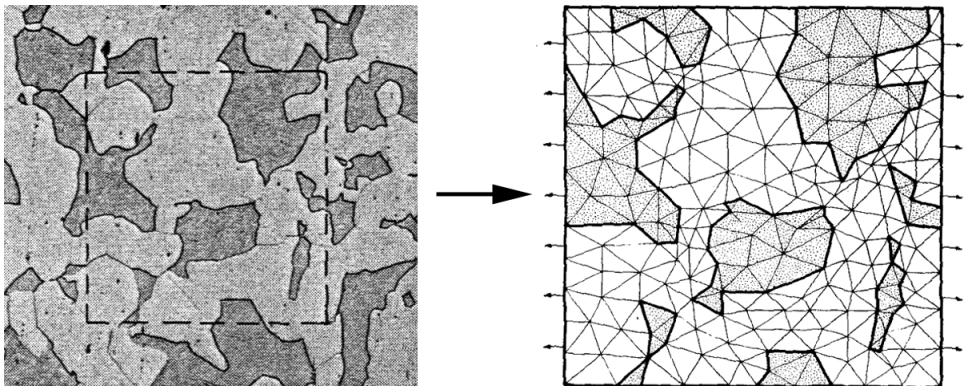

Figure 2.4: Fe-C microstructure and the corresponding finite element model (Reprinted from [44])

Linear work hardening was assumed for both the phases. The calculated stress-strain curves for matrix-inclusion combination with varying hardness ratios κ showed the strong effect of κ on the work hardening rate. Poech, Fischmeister, and others from Max-Planck-Institut für Metallforschung, Stuttgart studied the elastic and plastic stress-strain behavior of a WC-Co alloy using FE analysis of a cut-out from a 2D micrograph [45]. Mesh was generated using a digitizing tablet and the effect of mesh geometry, mesh density, model size, and loading direction were discussed in some detail. The variation in constitutive properties with respect to the microstructural parameters such as volume fraction, shape, and spatial arrangement of the phases were also studied. The stress-strain curves obtained from FE-modeling were reported to be in reasonable agreement with the experimental data. Similar studies were reported by others from the same group on transverse loaded fiber composites [28, 46]. Brockenbrough et al. used a Voronoi tessellation based on particle centers to characterize the spatial distribution of Si particles

in a micrograph from the gage section of a failed Al-10%Si binary alloy tensile specimen [47]. FE analysis was performed on the microstructural model preserving the spatial and size distributions of the particles from the micrograph but replacing the particles with equivalent circles to study the response of the material to uniaxial tension. In agreement with the experiment, larger particles and particles in the clustered region were found to be at higher stress levels.

Ghosh and his co-workers utilized Voronoi cells resulting from Dirichlet tessellation of a planar heterogeneous microstructure to represent the arbitrary distribution of inclusions and developed a novel and efficient numerical method, called the Voronoi Cell Finite Element Method (VCFEM) [48-50]. Dirichlet tessellation is defined as a subdivision of a region, determined by a set of points, such that each point has associated with it a region that is closer to it than to any other. These regions are termed Voronoi cells and may be identified as the basic structural elements of a heterogeneous microstructure. In VCFEM, each Voronoi cell is an element and the analysis needs no further discretization. They coupled the VCFEM for micro-analysis with conventional FEM for macro-analysis to develop a "hierarchical multiple scale" model [48]. Computer generated microstructures with different reinforcement volume fractions and spatial distributions were modeled using VCFEM to study their effect on the mechanical behavior of the heterogeneous material [49]. The VCFEM approach, though applicable only to certain types of microstructures, takes into account the spatial distribution of real microstructures and is economic requiring less computational time than conventional FE methods.

Steinkopff and Sautter suggested two new techniques; a rezoning algorithm for net-adaptation, and the use of multiphase elements, for incorporating the complex details of material microstructures in a finite element framework [51, 52]. The rezoning scheme involves adapting an initial regular FE net to the underlying microstructure cutout by projecting the nodal points onto the phase boundaries of the microstructure. The nodal points are then moved along the phase boundaries to improve the element quality. Since the phase boundaries are defined through the element edges, the rezoning technique allows for accurate modeling of the effects caused by local phase geometry. In the multiphase finite element method, different material properties are assigned to integration points within one element when a phase boundary runs across it, contrary to the traditional methods where the material properties are assigned to individual elements. This allows for the use simple and regular finite element mesh of any arbitrary shape to model complex microstructures as the FE mesh is independent of the phase structure of the material. Though very efficient in modeling complex microstructures, the multiphase approach blurs the phase boundaries in a microstructure and hence cannot be used for modeling of effects caused by very fine details in phase geometry. The authors simulated large plastic deformation in Ag-Ni fiber and particle composites using both the rezoning technique and multiphase element scheme and satisfactory agreement with experimental results were observed. Wulf, Steinkopff, and Fischmeister successfully used the multiphase finite elements (MPFE) along with an automatic element elimination technique (EET) to simulate the crack paths in a real microstructure cutout of Al/SiC_p composite [53]. In element elimination technique, a failure criterion is defined for each material before the analysis. All the components of stress tensors in the elements that

meet this criterion during the analysis are set to null. As a result, all forces in these elements become zero, and they stop transmitting load to neighboring non-eliminated elements. Mishnaevsky et al. modeled crack growth in real 2D microstructure of tool steel using MPFE along with EET [54]. They extended the method to include crack growth simulations on quasi-real microstructures with net-like, band-like and random distributions of both coarse and fine carbide particles with idealized circular geometry. It was concluded that the roughness of the fracture surface is higher for coarse microstructures compared to fine microstructures. The fracture resistance was found to be highest for net-like microstructure and lowest for band-like microstructure.

Hollister and Kikuchi developed Digital Image Based (DIB) modeling technique to study the effects of microstructural morphology of bone in FE simulations [55]. The models were constructed by converting digital voxels from 3D micro-computerized tomography scans directly into linear brick finite elements. It was shown that the DIB modeling, coupled with asymptotic expansion method, enabled the quantitative study of the mechanical behavior of the multiple level structure of bone within the framework of linear elasticity. Terada et al. further investigated the DIB method to study the mechanical behavior of metal matrix composites [56]. They also suggested the manipulation of digital images to realize virtual microstructures with different volume fractions. The method is computationally quite intensive, as each voxel/pixel in the micrograph is converted into a corresponding 3D/2D finite element for the analysis. Yue et al. reported 2D analysis of the mechanical behavior of asphalt concrete using digital image processing based finite element method [57].

Gokhale and Yang introduced a digital image processing technique to incorporate the effect of features at higher length scales on the damage evolution and local fracture processes occurring at lower length scales [7]. The methodology involved a combination of digital image processing techniques such as high-resolution large area montage creation [58], compression of digital microstructural images, and use of the digital image montages for the FE-based simulations of mechanical response. A cascading FE scheme (where the material input data for larger length scale analysis is obtained from the detailed modeling at the smaller length scale) was used to study the multi-length scale microstructure of a common commercial Al-Si-Mg base cast alloy (A356), where the length scale of micropores and silicon particles differed by about two orders of magnitude. Shan and Gokhale used 3D microstructure of A356 alloy reconstructed using serial sectioning technique to perform FE based simulations on the 3D pore structure [59, 60]. Local average stress and strain in the neighborhood of the pores computed from these simulations were used to calculate the void growth rate using McClintock rule. They concluded that the average void growth rate is grossly overestimated by the conventional unit cell models at stress levels significantly higher than the global yield stress. They also showed that the micromechanical response does not vary significantly if the pores are replaced by equivalent ellipsoids. Chawla et al. used serial sectioning to visualize and model a small volume of SiC particle reinforced Al composite [61]. They showed that the Young's modulus and stress-strain behavior of the composite predicted by FE analysis of the 3D model correlated very well with the experimental studies. Geandier and coworkers used X-ray microtomography to reconstruct the 3D microstructure of alumina-chromium composite [62]. The reconstructed microstructure

was incorporated in finite element method to calculate the residual thermal stresses in the material.

Langer, Carter, and others at NIST have developed a public domain C++ based, object oriented FEM software called OOF (named for its object-oriented finite elements) for finite element meshing and analysis of real microstructures to study their macroscopic thermoelastic behavior [63]. OOF consists of two programs: *ppm2oof* and *oof*. The program *ppm2oof* reads a real 2D microstructural image in the portable pixel map (ppm) format, assigns material properties to the microscopic features in the image, and creates a finite element mesh using three nodded triangular elements for subsequent computation. Adaptive mesh routines are used to conform the element edges to the phase boundaries and to refine the element size at the phase interfaces, by means of minimizing a functional E of the mesh which depends on the element's homogeneity and shape. The FE mesh created by *ppm2oof* is taken to *oof* to perform the virtual experiments. A third program named *oof2abaqus* allows for the conversion of the data sets created by *ppm2oof* into input files for Abaqus, a commercial finite element software package. A second version of the program, named OOF2, extended the analysis capabilities of OOF to electromechanical, electrochemical, and viscoplastic systems as well as adding support to more element types [64]. Several groups have reported using OOF to investigate material behavior in a variety of systems [65-78]. Boccaccini [71, 76] and Cannillo [72], for instance, used OOF to study the effect of pores on the macroscopic mechanical behavior of glass and ceramics with controlled porosity. Saigal et al. investigated interface properties on microcracking of iron titanate [65], stresses in aluminum-silicon alloys [68], and residual stresses in glass-infiltrated spinel ceramic composites [67] using OOF.

While a number of studies have involved incorporation of 2D microstructures in FE based micromechanical studies, modeling and simulation of realistic 3D microstructures is still a scarcely researched area. Successful modeling of three-dimensional metallic microstructures require (a) an efficient method to obtain the 3D microstructural data from a sufficiently large volume of the opaque specimen; and (b) a way to incorporate the 3D data thus obtained into the finite element framework and subsequent analysis. The former has been achieved in the past using techniques such as serial sectioning and x-ray tomography as mentioned earlier. Reported studies on the meshing and FE analysis of real 3D microstructures [59, 61] have involved analyses on very small microstructural volumes with no systematic study to ensure that the selected microstructural volume is indeed an RVE. Also, the question of how much more information can be obtained from 3D modeling compared to 2D analyses is still open. Though there have been some studies comparing the 2D and 3D simulations of simple idealized microstructural geometries, no such studies have been reported for realistic microstructural simulations. This is another area of interest in the current research.

2.4 Material Systems

Two different technologically important material systems, discontinuously reinforced aluminum alloys and boron modified titanium alloys, are investigated in this research. The following subsections serve to briefly introduce the two systems.

2.4.1 Discontinuously Reinforced Aluminum alloys

Discontinuously Reinforced Aluminum (DRA) composites are a class of metal matrix composites (MMC) in which an aluminum alloy matrix is reinforced with ceramic particles, whiskers, or short fibers. Arguably the most widely used MMC system, these

materials have found applications in the aerospace, automotive, electronic packaging, and recreational product markets over the last few decades. While various processing routes are available to manufacture DRA composites, Al-6061 alloys reinforced with SiC particles made using powder metallurgy (P/M) processing are the ones investigated in this research. A solid state processing technique, powder blending and consolidation (P/M processing) is one of the most common industrial methods used to produce composites having aluminum matrix [79]. Powders of the alloy and the reinforcement are first blended and that is followed by cold compaction, canning, degassing, and high temperature consolidation steps such as hot isostatic pressing or extrusion.

The process parameters that govern the final microstructure of DRA composites produced via P/M processing route include size/shape distributions of initial powders, compaction pressure, extrusion temperature, extrusion ratio, and relative amounts of the constituent powders. One of the important processing parameters in the production of the DRA composites is the particle size ratio (PSR), which is defined as the ratio of the mean size of the matrix powder particles to the mean size of the reinforcement particles. It is known that PSR is an important factor that affects the spatial homogeneity of the reinforcement phase distribution in the composites manufactured via powder metallurgy route [80]. Increasing the PSR leads to a reduction in the combined surface area of the matrix alloy particles and as this area becomes insufficient for a uniform arrangement of reinforcement particles, clusters of the reinforcement particles are formed in-between the larger matrix particles. An increase in the compaction pressure causes a reduction in the resulting porosity of the composites [81]. As for the extrusion parameters, the increase in extrusion temperature increases the anisotropy in the distribution of the second phase

particles and particle rich clusters, while reducing the overall porosity in the microstructure [82]. Increasing the extrusion ratio causes more uniform distribution of reinforcement particles but increases the microstructural anisotropy [83].

The mechanical properties of the DRA composites depend on (1) volume fraction, (2) mean size, (3) morphologies/shapes, (4) spatial clustering, and (5) orientations/anisotropy of the reinforcement particles as well as on the constitutive behavior of the matrix that can be altered via heat treatment. The microstructural attributes are in turn governed by the process parameters such as (1) size-shape distribution of the initial constituent powder particles, (2) particle size ratio, and (3) powder compaction, extrusion, and heat treatment process conditions. Therefore, there are multi-parameter multi-variate processing-microstructure-properties relationships in these composites.

2.4.2 Boron Modified Ti-6Al-4V Alloys

Addition of small amounts of boron during high temperature processing of titanium alloys has emerged as an effective way to improve the mechanical properties and wear resistance of these alloys, while at the same time maintaining the high strength-to-weight ration and excellent corrosion resistance of titanium. The property improvements are attributed to the *in situ* formation of TiB phase during high temperature processing of these alloys. The titanium rich region of binary Ti-B phase diagram is given in Figure 2.5 which shows the formation of the TiB intermetallic phase from a eutectic reaction.

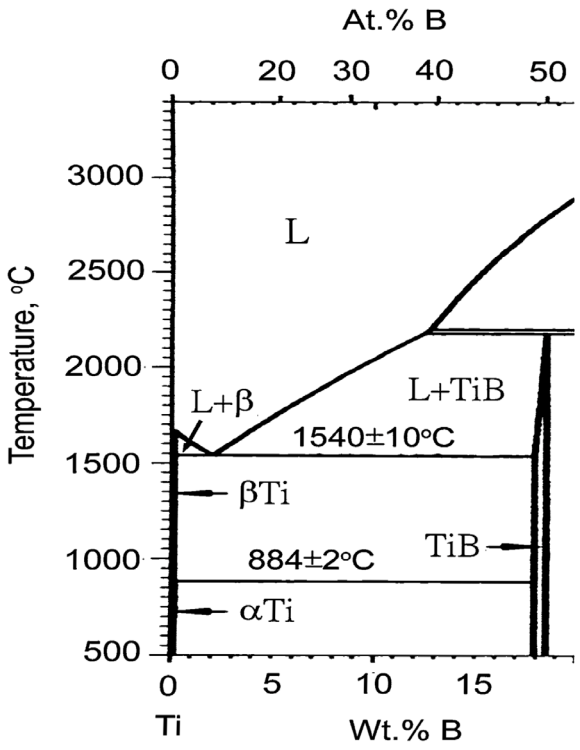

Figure 2.5: Titanium rich region of binary Ti-B phase diagram (Reprinted from [84])

Boron is completely soluble in liquid titanium but is essentially insoluble in the solid titanium phases (high temperature β as well as room temperature α phase). The density of TiB is comparable to that of titanium but the stiffness is about 3-4 times that of conventional titanium. It may be noticed from the phase diagram that for hypereutectic Ti-B alloys, along with the eutectic phase, TiB also forms as a primary phase directly precipitating from the liquid phase. TiB is both thermomechanically stable and essentially insoluble in Ti once they are formed. TiB has excellent crystallographic compatibility with titanium, providing atomically sharp interfaces and chemical compatibility. The coefficient of thermal expansion of TiB is comparable to titanium, which minimizes residual stresses at the interfaces. It has also been shown that TiB is stable only in a titanium matrix, due to the thermodynamics of the reactions forming TiB from titanium

and TiB_2, with TiB more stable than TiB_2 only when excess moles of titanium are present. Single crystals with an orthorhombic B27 structure and a roughly hexagonal cross-section, TiB grow in the form of whiskers with an aspect ratio typically between 4 and 10. Boron-modified titanium alloys have the potential to expand the usage of titanium and are attractive for a variety of applications in the automotive, aerospace, biomedical, and sporting goods industries.

Interest in micromechanical modeling of boron modified titanium alloys stems from the observation of TiB whisker alignment with deformation, showing promise of controlled anisotropy in this material system [85]. In this dissertation, micromechanical studies are carried out on boron modified Ti-6Al-4V alloys made using P/M processing of pre-alloyed powder. Pre-alloying is a rapid solidification process where an alloy melt is rapidly solidified into an alloy powder by inert gas atomization. The pre-alloyed powder can be processed using conventional powder metallurgy processes, including outgassing to remove any volatile impurities and compaction by techniques such as hot isostatic pressing (HIP) to produce near-net shape products or billet preforms. These billet preforms can then be subjected to thermo-mechanical processing (TMP) methods such as forging, rolling, or extrusion to manufacture wrought products. Note the each of these processing steps and associated process parameters affect the microstructure attributes (for example, size, shape, and orientations of TiB whiskers, their volume fraction, etc.), and consequently, the mechanical properties of these materials.

Ti-6Al-4V is the most widely used titanium alloy, accounting for more than half of the overall worldwide titanium tonnage [86]. The aluminum addition stabilizes the hcp α phase, which increases the overall strength of the resultant alloy. The vanadium

addition introduces bcc β phase into the α matrix, increasing ductility and fracture toughness. Ti-6Al-4V is considered an α-rich α+β alloy. In boron modified Ti-6Al-4V alloys, the microstructure consists of *in situ* formed TiB whiskers in a matrix of equiaxed α grains and retained β phase decorating the grain boundaries. It has been shown that the TiB whiskers effectively pin the grain boundaries of the titanium alloy matrix so that a fine grain structure is retained even well above the β-transus and after cooling back into the α+β phase field [87, 88].

2.5 Stereology, Image Analysis and Microstructure Simulations

Detailed quantification of microstructural geometry is an essential pre-requisite for accurate modeling and simulation of material microstructures. Stereology involves the estimation of the properties of three-dimensional microstructural features through unbiased sampling of the three-dimensional microstructural space using geometric test probes such as planes, lines, or points. For opaque materials such as the metallic composites, quantitative metallographic techniques have been developed (and continue to be developed) to estimate 3D microstructural information from 2D sections of the microstructural volume.

2.5.1 Two-point Correlation Functions

A vast majority of heterogeneous material microstructures are stochastic in nature and hence the spatial distributions of various phases can be characterized only in a statistical sense. Statistical descriptors such as nearest neighbor distributions, radial distribution function, *n*-point correlation function and lineal path probability functions are

routinely used in describing spatial patterns like randomness, clustering, short- and long-range interactions between different phases in a microstructure [89-91].

For a two-phase microstructure, a two-point correlation function $P_{ij}(r, \theta, \varphi)$ is the probability that a straight line of length r and angular orientation (θ, φ) randomly placed in a 3D microstructure is such that its first end is in the phase i (where $i = 1$ or 2) and the second end is contained in the phase j (where $j = 1$ or 2). Figure 2.6 shows a schematic of the orientation of a line in 3D space and direction dependent two-point functions.

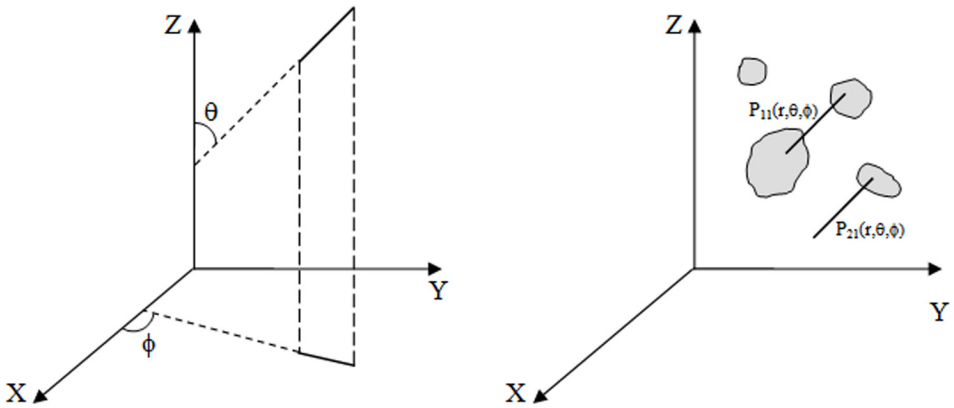

Figure 2.6: Schematic of two-point correlation functions

Note that the probability associated with a two-point correlation function only concerns the events at the end points of the line. For a two-phase microstructure, there are four possible two-point correlation functions, namely $P_{11}(r, \theta, \varphi)$, $P_{22}(r, \theta, \varphi)$, $P_{12}(r, \theta, \varphi)$, and $P_{21}(r, \theta, \varphi)$. However, only one of the four two-point correlation functions is independent [92]. As r approaches zero, $P_{11}(r, \theta, \varphi)$ approaches the value equal to the volume fraction of the particulate phase; as r goes to infinity, it approaches the value equal to the square of the volume fraction of the particulate phase. At other values of the length of the line r, $P_{11}(r, \theta, \varphi)$ depends on the particle shapes/morphologies, the first-

order global microstructural properties, the spatial arrangement of the particles, and morphological anisotropy. The microstructures studied in the present work are of extruded metal matrix composites. In such materials, the extrusion direction represents an axis of symmetry such that the microstructure observed in any metallographic plane containing the extrusion axis is statistically similar to that observed in any other plane containing the extrusion axis. This implies that the two-point correlation function measured in all planes containing extrusion axis would be statistically similar, and therefore independent of φ [91].

2.5.2 Three-Dimensional Microstructure Reconstruction

While stereological techniques allow for the estimation of a number of 3D microstructural parameters through observations on 2D sections, a 2D metallographic section does not contain all of the information concerning the true 3D geometry of the microstructure. Accordingly, reconstruction of 3D microstructures of materials is of great interest to material scientists for understanding and modeling processing-microstructure-properties relationships. A number of techniques such as serial sectioning [59, 61], focused ion beam milling [93], and X-ray tomography [62] have been reported in the literature for 3D reconstruction of opaque material microstructures. Of these, serial sectioning is the most widely used technique when the characteristic length scale of the microstructure is of the order of a micron or higher. Serial sectioning involves successive polishing and imaging of a material specimen using standard metallographic procedures resulting in a stack of images from which the 3D microstructure is digitally reconstructed using computational tools. An efficient and unbiased montage serial sectioning technique has been developed at the author's group in Georgia Tech for the reconstruction of large

volume (~several mm^3), high resolution (~1μm) 3D microstructures [94, 95]. Montage serial sectioning involves capturing large-area high-resolution montage images of the metallographic plane after each polishing step, and the montage 2D sections are subsequently used to reconstruct large 3D volumes.

2.5.3 Realistic Microstructure Simulations

An evident disadvantage of microstructure simulations using real microstructural fields of view is their inability to provide any information on how to improve the properties of a given material. In other words, such simulations based on a real microstructural cutout are useful only for mimicking the mechanical response of a material that already exists. Parametric studies using realistic phase geometries are necessary for real microstructure simulations to be of use in material development studies. While it is relatively straight forward to conduct parametric studies using idealized microstructures involving simplistic phase morphologies and isotropic uniform random distribution, it is quite challenging to incorporate the complex morphological and spatial aspects of real material microstructures in such models. Consequently no such parametric studies have been reported in the literature to the best of author's knowledge. Systematic methodologies for realizing 2D [96-98] and 3D [99] computer simulated microstructures using realistic microstructural feature morphologies, which are statistically similar to real microstructures, have been developed recently by others in author's group at Georgia Tech. The methodology involves capturing the details of microstructural geometry (including spatial clustering) and its variations with process parameters in terms of a small set of simulation parameters using a combination of standard stereological and statistical tools. Statistical descriptors such as lineal-path

probability functions and two-point correlation functions are used to ensure that the geometry of the simulated microstructure is similar to that of the corresponding real microstructure. The simulation parameters are then varied to generate 'virtual' microstructures covering the complete regime of variations in processing conditions of interest. One of the contributions of the current research is the micromechanical simulations of such realistic virtual microstructures to predict the changes in mechanical behavior of these materials with different processing conditions.

2.6 Material Constitutive Properties

The usefulness of a finite element analysis depends to a great extent on the accuracy of the material constitutive properties that one provides as input in the analysis. Most of the reported work on microstructure based numerical studies of composite materials use the constitutive properties obtained from macroscopic experiments (such as that obtained from a tensile test) of individual phases as the input in finite element analysis. Such phenomenological stress-strain data may not always be accurate and/or available for micromechanical studies. Boron modified titanium alloys are an example for such a material system. Because TiB is stable only within a titanium alloy, it is not possible to obtain the constitutive behavior of TiB using a tensile test. Also, as mentioned earlier, TiB whiskers pin the grain boundaries of the titanium alloy matrix resulting in a finer grain size for the matrix. This effectively changes the constitutive behavior of the matrix, with a strengthening of the material arising from Hall-Petch effect [100]. Hence the use of constitutive properties of unreinforced Ti-6Al-4V alloy for finite element based micromechanical studies will be inaccurate. Current research involves the use of instrumented indentation to obtain the local constitutive behavior of such small

microstructural volumes, which in turn are used as input in microstructure based finite element analysis of these materials.

2.6.1 Instrumented Indentation

2.6.1.1 Introduction

Instrumented indentation, which provides a continuous record of the indentation load P as a function of the depth of penetration h of the indenter into the material, is a widely used technique to study the mechanical behavior of small microstructural volumes. The load-displacement curve thus obtained provides a wealth of information on the mechanical properties of the material in addition to the hardness of the material, which is the primary output of traditional indentation tests. Figure 2.7 shows a schematic of the indentation process. As the indenter is driven into the material, both elastic and plastic deformation processes occur, producing a hardness impression that conforms to the shape of the indenter to some contact depth, h_c. The radius of the circle of contact is a. As the indenter is withdrawn, only the elastic portion of the displacement is recovered, which effectively allows the separation of the elastic properties of the material from the plastic.

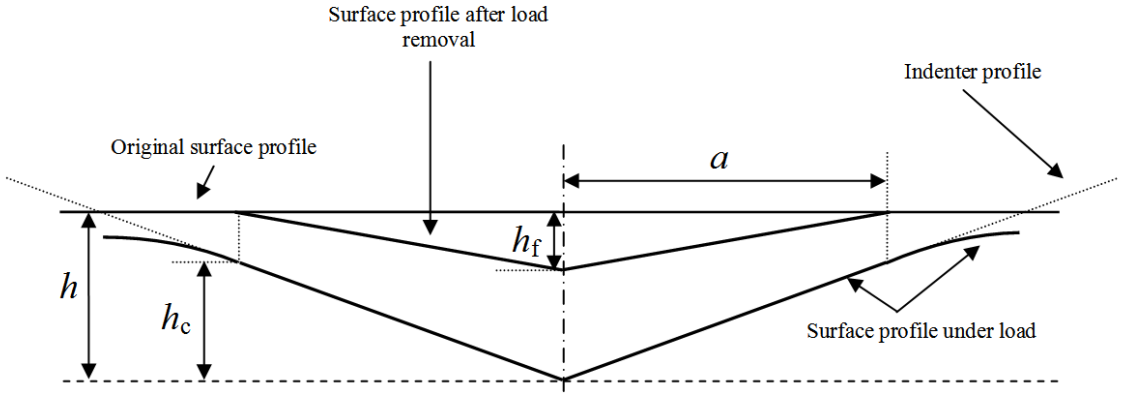

Figure 2.7: Schematic of indentation process [101]

A schematic representation of indentation load (P) versus displacement (h) data obtained during one full cycle of loading and unloading is shown in Figure 2.8. The important quantities are the peak load (P_{max}), the maximum depth (h_{max}), the final or residual depth after unloading (h_f), and the slope of the upper portion of the unloading curve ($S = dP/dh$), known as the contact stiffness.

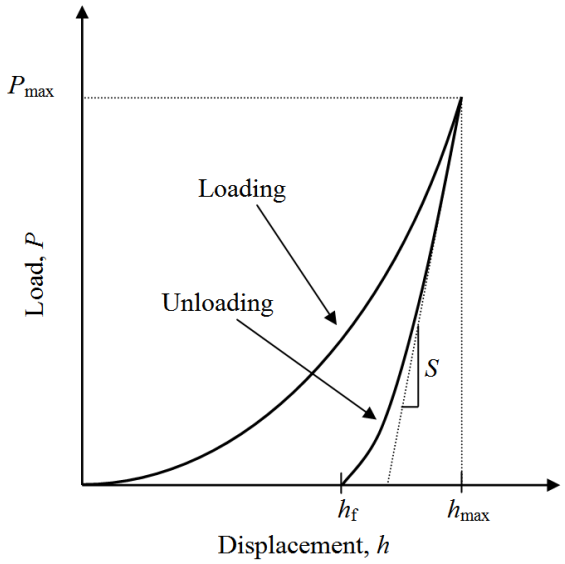

Figure 2.8: Schematic of load-depth curve obtained from instrumented indentation [101]

The elastic modulus is determined using the equation:

$$E_r = \frac{\sqrt{\pi}}{2\beta}\frac{S}{\sqrt{A}} \tag{2}$$

where E_r is the reduced elastic modulus, β is a constant that depends on the geometry of the indenter (β = 1.012 for Vickers pyramid), and A is the projected contact area at the load P. A reduced modulus accounts for the fact that elastic displacements occur in both the indenter and the sample. The elastic modulus of the test material, E, is calculated from E_r using:

$$\frac{1}{E_r} = \frac{1-\nu^2}{E} + \frac{1-\nu_i^2}{E_i} \tag{3}$$

where ν is the Poisson's ratio for the test material, and E_i and ν_i are the elastic modulus and Poisson's ratio, respectively, of the indenter. Accurate measurement of the contact stiffness (S) and the projected contact area under load (A) are necessary to determine the elastic modulus of the material, as can be observed from equation 2. The most widely used method for determining the contact area was developed by Oliver and Pharr which begins by fitting the unloading portion of the load-displacement data to the power-law relation:

$$P = BA(h - h_f)^m \tag{4}$$

where B and m are empirically determined fitting parameters. The contact stiffness (S) is determined as:

$$S = \left(\frac{dP}{dh}\right)_{h=h_{\max}} = Bm(h_{\max} - h_f)^{m-1} \tag{5}$$

The contact depth (h_c), which for elastic contact is less than the total depth of penetration (h_{max}), is estimated using:

$$h_c = h - \varepsilon \frac{P}{S} \tag{6}$$

where ε is a constant that depends on the indenter geometry. Note that equation 6 does not account for the phenomenon of pile-up because its derivation is based strictly on elastic contact in which sink-in always occurs [101].

Instrumented indentation methods are broadly classified into micro- and nano-indentation techniques depending upon the length scale of the indentation test. Nanoindenters are used when the indentation depths involved are in the sub-micron regime. Displacements of as small as 0.1 nm and loads of 0.1 nN can be accurately applied and measured using modern equipments [101]. Microindenters are more suitable when the material behavior of a much larger microstructural volume, in the range of few tens of microns, is to be studied. While the operating regimes are different, the fundamental underlying principles are the same for both micro- and nano- indentation testing. Sharp pyramidal indenters, such as Vickers and Berkovich, are the most commonly used geometries in instrumented indentation [101]. For a sharp indenter, the load-displacement relationship during loading is purely quadratic with a constant curvature, i.e. $P = Ch^2$. This square dependence has been shown to be a direct consequence of the absence of a length scale in sharp indenters using dimensional analysis [102]. For spherical indenters, on the other hand, the curvature of the loading portion of the load-displacement curve is continuously decreased with increasing penetration into the material and hence the load-displacement curve provides more information than that from a sharp indenter, which has a fixed apex angle [103]. Also, while plastic deformation in the material starts almost instantaneously on contact with

sharp indenters, spherical indentation starts with an elastic response followed by yielding and plastic deformation.

2.6.1.2 Reverse Analysis to Deduce Constitutive Properties

Deducing the local stress-strain behavior of a material from the indentation load-displacement curve has been of interest for various researchers [104-107]. This is primarily due to the idea that the constitutive properties of small microstructural volumes such as thin films, which are otherwise not obtainable through phenomenological methods such as the uniaxial tensile test, could be reliably measured using the technique. Determination of the elastic-plastic behavior of the indented material from the load-displacement curve usually involves the assumption that the constitutive behavior of the indented material may be approximated by a power-law strain hardening plastic response beyond the initial yield stress. The stress-strain behavior for a power-law strain hardening material may be written as

$$\sigma = \begin{cases} E\varepsilon & \text{for } \sigma \le \sigma_y \\ R\varepsilon^n & \text{for } \sigma \ge \sigma_y \end{cases} \tag{7}$$

where E is the Young's modulus, R a strength coefficient, n the strain hardening exponent, and σ_y the initial yield stress of the material. Invoking the continuity requirement at yielding, it can be shown that, for $\sigma \ge \sigma_y$

$$\sigma = \sigma_y \left(1 + \frac{E}{\sigma_y} \varepsilon_p \right)^n \tag{8}$$

where ε_p is the true plastic strain. Thus for an isotropic, homogeneous power-law hardening material, four independent parameters (E, ν, σ_y, n) are needed to completely describe the constitutive behavior. Solving the "inverse problem" of deducing the

material properties from an indentation load-displacement curve thus involves either of the following two steps: (1) iteratively modifying the material properties in a finite element model of the indentation until the simulated load-displacement curve matches with the experimental results and use the material properties thus obtained as representative of the indented material or (2) a more general approach where extensive finite element simulations are carried out, for a given indenter angle, with wide ranging material properties to deduce analytical expressions relating the material properties (E, ν, σ_y, n) to the parameters obtained from the load-displacement curve such as the loading curvature, initial slope of the unloading curve, and the ratio of the residual depth to maximum indentation depth. A mathematically deduced quantity named representative strain (and the corresponding representative stress) is frequently used in such analytical expressions to reduce the number of unknown variables [103, 108].

2.6.1.3 Uniqueness of Reverse Analysis

Earlier reported studies on calculating the elastic-plastic material properties from indentation load-displacement curves were based on the assumption that the indentation response was unique for a given material. In other words, it was assumed that there exists one, and only one, set of (E, ν, σ_y, n) that would yield a given load-displacement curve. This uniqueness assumption has been questioned by several research groups and it has been shown that for a given sharp indenter, the exact same indentation response may be obtained from distinct sets of material properties [109, 110]. The dual sharp indenter technique, where the indentation response from two sharp indenters with different apex angles are used to deduce the material properties, has been suggested as an alternative to overcome the issue of non-uniqueness [111]. A recent study has shown that even the use

of dual sharp indenters cannot satisfy the uniqueness requirement [103]. The authors conducted a systematic numerical study to show the existence of so-called “mystical materials”, which yield non-distinguishable load-displacement curves for a wide range of indenter angles despite having distinct constitutive properties. They concluded that for bulk materials, spherical indentations with sufficiently deep penetration (ratio of penetration depth to indenter radius more than 0.3) may be used to get a unique solution.

CHAPTER 3

INSTRUMENTED INDENTATION

3.1 Introduction

Most of the reported work on microstructure based numerical studies of composite materials use the constitutive properties obtained from macroscopic experiments (such as that obtained from a tensile test) of individual phases as the input in finite element analysis. Such phenomenological stress-strain data may not always be accurate and/or available for micromechanical studies. For instance, as mentioned in the previous chapter, TiB is stable only when excess moles of titanium are present and hence it is not possible to manufacture bulk TiB for tensile tests. Also, the TiB whiskers pin the grain boundaries of the titanium alloy matrix resulting in a finer grain size for the matrix, effectively changing the constitutive behavior of the matrix. Instrumented indentation technique was employed to deduce the constitutive properties of different microstructural phases under investigation in this study. As discussed in the previous chapter, the load-displacement curve obtained from instrumented indentation can be used to compute material properties such as the elastic modulus E, yield strength σ_y, and the work hardening parameter, n. Analytical expressions such as Oliver-Pharr method are commonly used to deduce the elastic modulus of the indented material from the load-displacement curve. A fairly accurate estimate of modulus can be obtained if the indented material does not exhibit pile-up around the indent, which includes most ceramics and metals with high work hardening. But the estimation of other material parameters such as σ_y and n (and E for ductile metals exhibiting pile-up) is much more involved and usually

involves reverse analysis using FEM. This chapter details the indentation experiments and simulations carried out as a part of this dissertation to deduce the constitutive properties of Ti-6Al-4V matrix and TiB whiskers in boron modified Ti-6Al-4V alloys, and Al-6061 matrix in DRA composites. Section 3.2 describes the finite element model creation and analysis details. Indentation experiments and reverse analyses using FEM are discussed in the subsequent sections.

3.2 Finite Element Modeling of Indentation

The local constitutive properties of small microstructural volumes are deduced by solving the inverse problem via FEM where the material constitutive properties in a finite element model of the indentation process are incrementally varied until the simulated load-depth curve matches the experimental curve in both loading and unloading regimes. The material constitutive properties that lead to such an agreement can be considered as representative of the local material behavior and can be used as the input in FE based micromechanical studies. Commercial finite element code Abaqus/Standard 6.6-1 was used for the analyses. A brief introduction to the Abaqus software suite is given in the following section before moving to the indentation modeling details.

3.2.1 Abaqus Finite Element Analysis Package

Abaqus is a suite of powerful engineering simulation programs, based on the finite element method, that can solve problems ranging from relatively simple linear analyses to the most challenging nonlinear simulations. It contains an extensive library of elements that can model virtually any geometry and has an equally extensive list of material models that can simulate the behavior of most typical engineering materials. Abaqus consists of two main analysis products - Abaqus/Standard and Abaqus/Explicit.

Abaqus/Standard is a general-purpose analysis product that can solve a wide range of linear and nonlinear problems involving the static, dynamic, thermal, and electrical response of components. Abaqus/Standard solves a system of equations implicitly at each solution "increment." Abaqus/Explicit is a special-purpose analysis product that uses an explicit dynamic finite element formulation. It is suitable for modeling brief, transient dynamic events, such as impact and blast problems, and is also very efficient for highly nonlinear problems involving changing contact conditions, such as forming simulations. In contrast to the implicit solution procedure in Abaqus/Standard, Abaqus/Explicit marches a solution forward through time in small time increments without solving a coupled system of equations at each increment (or even forming a global stiffness matrix). Further details can be found elsewhere [112].

3.2.1.1 Analysis Units

Abaqus has no built-in system of units. It is left to the user to specify all the input data in a consistent set of units. In this dissertation, length, mass, and time are specified in μm, μg, and μs respectively. Units for derived quantities such as force, stress, energy, and density were then determined in a consistent manner. Table 1 gives the set of units used in this dissertation. Note that the time and mass units are of no relevance while performing static analyses using Abaqus/Standard package.

Table 1.1: Set of units used in this dissertation research

Quantity	Length	Mass	Time	Force	Stress	Energy	Density
Units	μm	μg	μs	mN	GPa	nJ	$\mu g/ \mu m^3$

3.2.2 Indentation Modeling

The indentation process involving both spherical and Vickers indenters was modeled using finite element method. In the model, the indenter and the specimen were treated as bodies of revolution in order to simplify the 3D problem into a 2D axisymmetric problem. While this simplification holds true for a spherical indenter, the same cannot be said about Vickers pyramid indenter, the geometry of which is not axisymmetric in an exact sense. But it has been shown by other researchers that the Vickers pyramid could be replaced by an equivalent cone in FE analyses provided the equivalent cone geometry is defined in such a way that the cross-sectional area of the Vickers pyramid and the conical indenter are the same at a given penetration depth, h [113]. As illustrated in Figure 3.1, the equivalent cone cross-section radius r_{eqv} at any given penetration depth is calculated by means of the equation:

$$r_{eqv} = \frac{a}{\sqrt{\pi}} \tag{9}$$

where a is the Vickers pyramid rectangle side length.

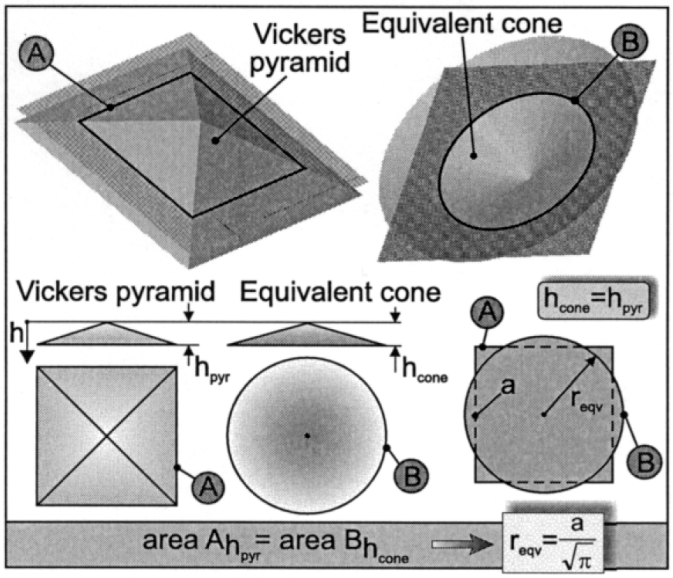

Figure 3.1: Equivalent cone approximation for Vickers pyramid (Reprinted from [113], with permission from Elsevier)

The quasi-static nature of indentation allows for the process to be modeled as a static analysis using Abaqus/Standard. Nonlinear geometry (NLGEOM) was activated to account for the large deformation in the sample immediately underneath the indenter. The diamond indenter was assumed to be perfectly elastic with manufacturer supplied properties of elastic modulus E = 1141 GPa, and Poisson's ratio $\nu = 0.07$. The sample and the indenter were modeled using four-node axisymmetric quadrilateral elements (CAX4). The constitutive model for the specimen was assumed to be elastic-plastic with power-law hardening plastic behavior. Experimentally observed Poisson's ratio of 0.33 was used. Size effects, arising from the geometrically necessary dislocations associated with non-uniform plastic deformation, are sometimes of concern when investigating the deformation behavior during micron or sub-micron level indentation. The intrinsic material length in strain gradient plasticity is given by $\left(\mu/\sigma_y\right)^2 b$ where μ is the shear

modulus, σ_y the yield strength and b, the Burgers vector [114]. For Ti-6Al-4V, the intrinsic material length is of the order of few hundreds of nanometers. As the indentation depth in the present study is 8 μm, which is much larger than the intrinsic material length, such size effects are ignored and continuum plasticity theories are assumed to hold valid. Figure 3.2 shows the indentation model created in Abaqus. The FE mesh is well refined with element edge length of the order of 0.5 μm at the region where it is expected to make contact with the indenter in order to account for the large stress concentration expected to arise during the indentation. Finite surface-to-surface sliding contact was defined between the bottom of the indenter and the specimen top. The top edge of the indenter was constrained to have the same vertical displacement as the top corner of the indenter along the axial symmetry axis, the point P shown in Figure 3.2. The indentation experiment was simulated by applying a downward displacement at the point P which causes the indenter to push into the material. The bottom side of the sample was pinned to avoid rigid body motion. The load-displacement curve was obtained by plotting the reaction force versus the displacement at point P.

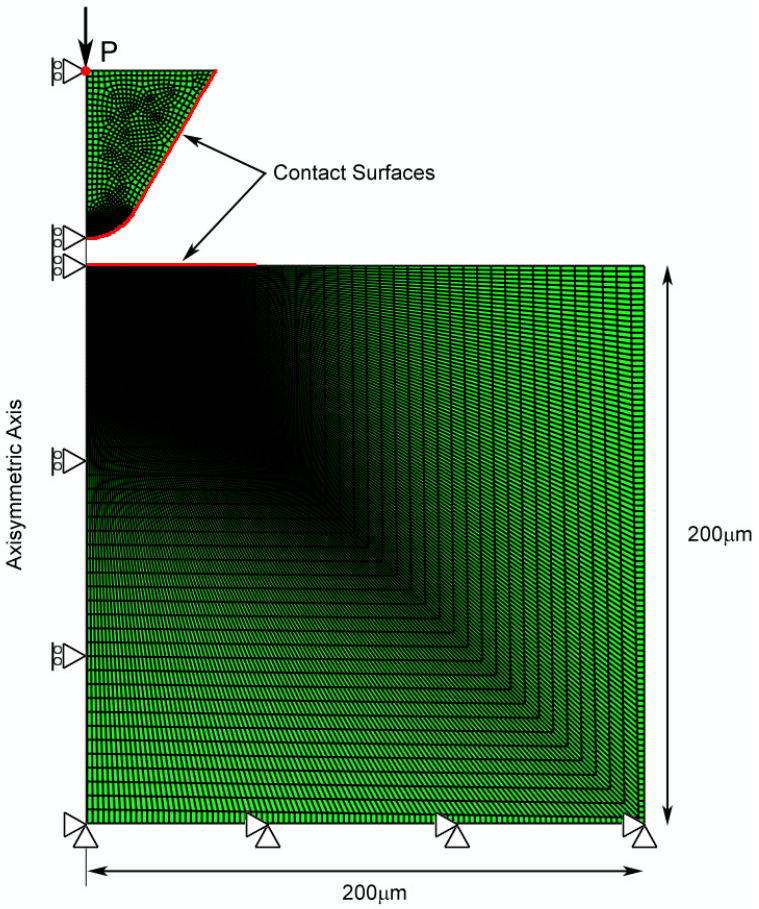

Figure 3.2: Finite element model of spherical indentation process

3.2.2.1 Indenter Tip Geometry

Geometry of the indenter tip must be accurately represented in the FE model for reliable comparison with the experimental results. This is particularly true when the aim is to deduce the constitutive properties of the material through reverse analysis using FEA. Sharp indenters such as the Vickers pyramid have, in reality, a finite radius of curvature at the tip. Figure 3.3 shows the SEM image of the Vickers pyramid indenter used in this research. Radius of the curvature of the tip was determined to be 2.76 μm. Similarly, Figure 3.4 shows the profile of the spherical indenter used in this study, which

is meant to have a radius of 20 μm. It was observed that the actual radius of the tip is 19.28 μm. These values were incorporated in the FE models of indentation.

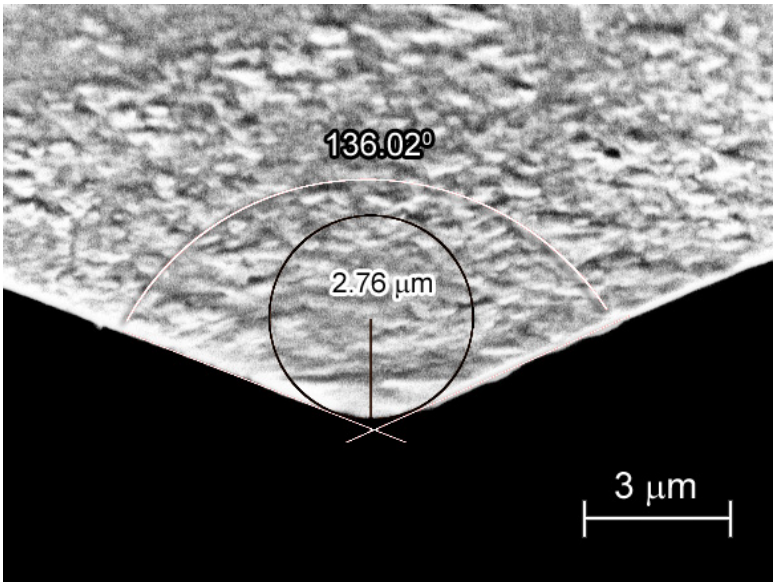

Figure 3.3: SEM image of the Vickers pyramid indenter tip

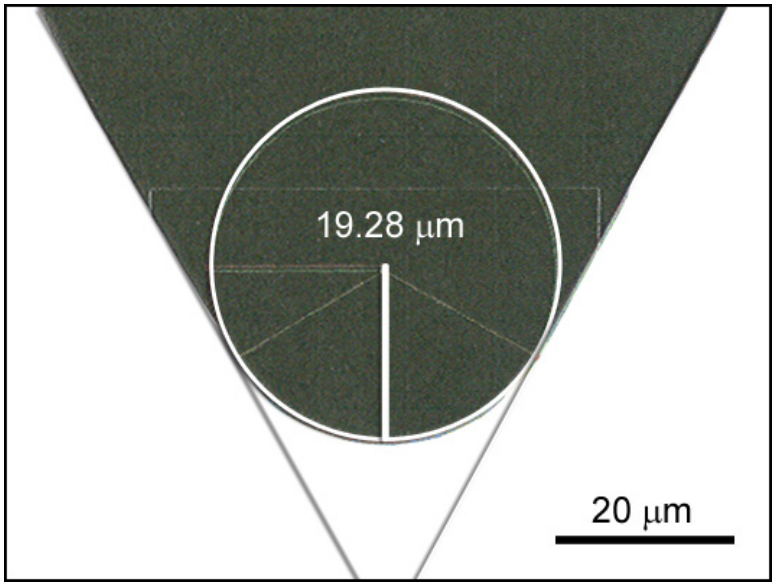

Figure 3.4: Profile of the spherical indenter tip

3.2.2.2 Model Validation

The finite element model was validated by comparing the modeling results of spherical indentation of a perfectly elastic specimen with the analytical results based on Hertzian contact. For a perfectly elastic friction-less contact between a sphere of diameter D_i and a plane surface, the total elastic compression at the point of contact of two bodies (same as penetration depth for indentation) at load P is given by:

$$h = \left(\frac{9}{8}\right)^{1/3} \left(\frac{1}{E_r}\right)^{2/3} \left(\frac{1}{D_i}\right)^{1/3} P^{2/3} \tag{10}$$

where E_r is the reduced modulus as defined in Equation 3 [115]. Figure 3.5 shows the comparison between theoretical and FE simulated load-displacement curves during the loading regime for elastic contact between diamond indenter and an elastic material with modulus E = 110 GPa, and Poisson's ratio ν = 0.33. The finite element model mesh density and boundary conditions are as described in the previous section. There is excellent agreement between the load-displacement curves predicted by the finite element model and Equation 10. Figure 3.6 shows the von Mises stress contour plot on the indented material at maximum load.

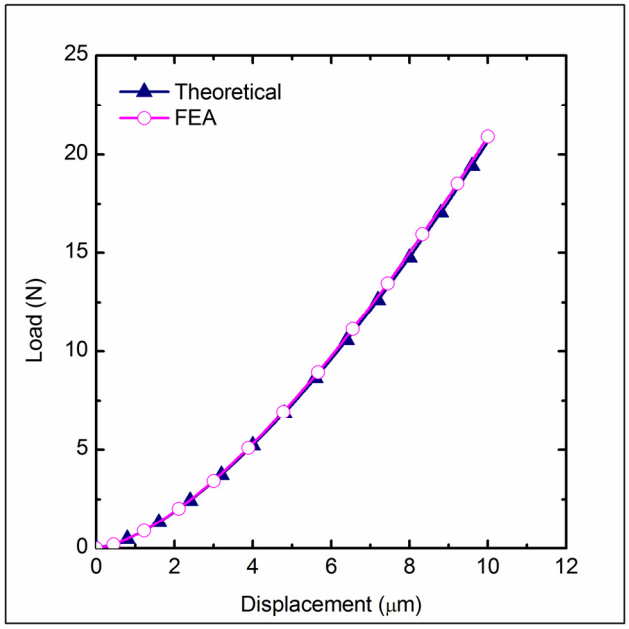

Figure 3.5: Comparison between theoretical and FE simulated load-displacement curves for Hertzian contact

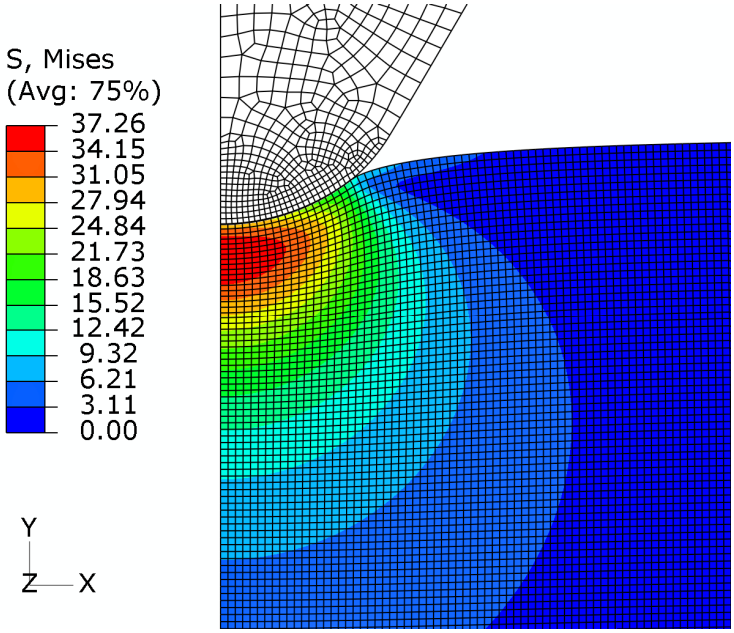

Figure 3.6: von Mises stress (GPa) contour plot on the indented material at maximum load

3.2.2.3 Effect of Friction

Historically, the interface between the indenter and the specimen is assumed to be frictionless in FE modeling studies. It has been suggested by various authors that the frictional coefficient has negligible effect on the indentation load-displacement curve [106, 116-119]. Effect of friction on the load-displacement curve for indentation of an elastic-plastic material was investigated as part of this dissertation. To study the effect of friction, the sample material in the FE model was assumed to be a power-law hardening material with the parameters $E = 100\ GPa$, $\nu = 0.33$, σ_y = 1000 MPa, and $n = 0.1$. While friction was found to have a negligible effect on the indentation load-displacement curve for Vickers pyramid, it was observed that it significantly affects the results for spherical indentation at penetration depths larger than an h/R ratio of ~ 0.2 where h is the penetration depth and R, the indenter radius. This may be attributed to the much larger surface area of a spherical indenter compared to Vickers pyramid. Load-displacement curves for coefficient of friction values ranging from 0 to 0.3 for spherical indenter of 19.28 μm radius and Vickers pyramid are shown in Figures 3.7a and 3.7b respectively. Figure 3.8 shows the percentage deviation in the load at the maximum penetration depth of 10 μm for both spherical and Vickers indenters with varying coefficients of friction.

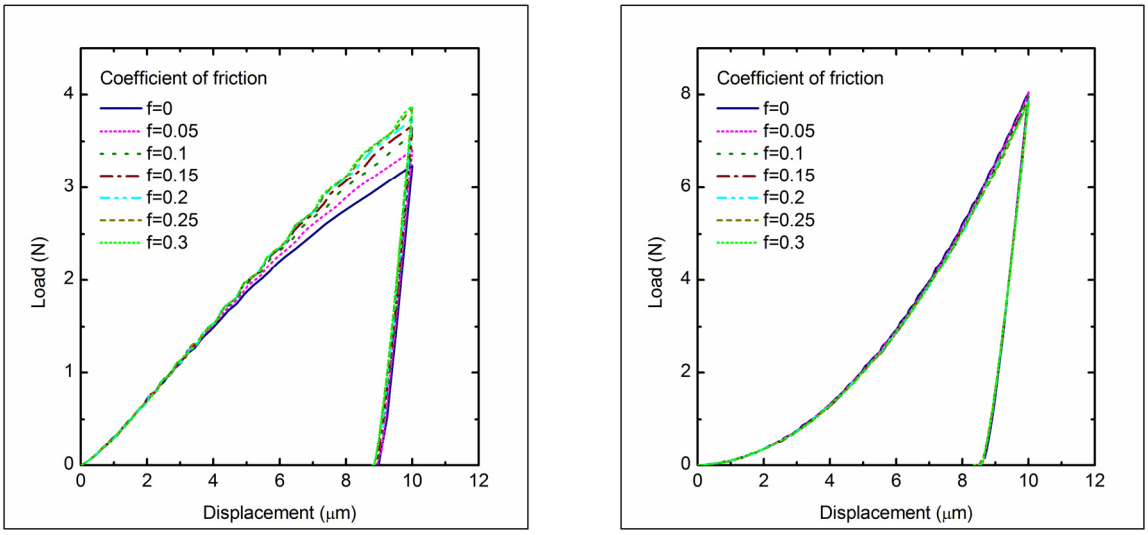

(a) (b)

Figure 3.7: Effect of friction on indentation response using (a) Spherical indenter and (b) Vickers pyramid indenter

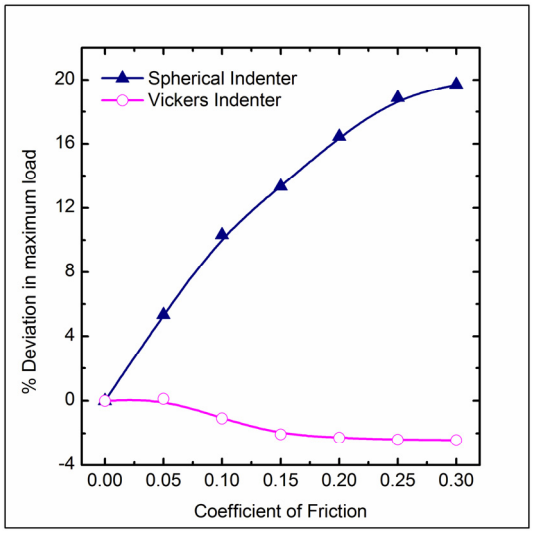

Figure 3.8: Percentage deviations in maximum load for spherical and Vickers indenters with varying coefficients of friction

For a diamond-metal contact, coefficient of friction value is usually taken as 0.15 [103] and accordingly, this value is used in all the analyses conducted as part of this dissertation.

3.3 Constitutive Properties of Ti-6Al-4V Alloy

3.3.1 Processing and Microstructure of Ti-6Al-4V-1B Alloy

The experiments were performed on Ti-6Al-4V-1B alloy (all compositions are in weight percent) supplied by the Air Force Research Laboratory (AFRL). The alloy was produced via a pre-alloyed powder metallurgy approach at Crucible Research Corporation, Pittsburgh, Pennsylvania. In this process, a liquid melt of Ti-6Al-4V containing boron was rapidly solidified using inert gas atomization to produce Ti-6Al-4V-1B powder. The atomized powder was then sieved to obtain –35 mesh size (average particle size of 400μm). Further processing of the powder was performed by Dr. Tamirisakandala and colleagues at AFRL, Wright-Patterson Air Force Base, Ohio. The Ti-6Al-4V-1B powder was packed inside a thick-walled canister of Ti-6Al-4V, vacuum outgassed at 300°C for 24 hours, and sealed. The canister was then heated to 1200°C, soaked for 1 hour, and subsequently blind die compacted in an extrusion chamber heated to 260°C. The billet height was reduced by about 30% at a ram speed of 6.35 mm s^{-1}, and the compact was held at a pressure of 1400 MPa for 180 seconds and subsequently hot extruded at 1100°C with an extrusion ratio of 16.5:1, at a ram speed of 6.35 mm s^{-1}, and air-cooled to room temperature. Specimens were sectioned from the extruded rod, and were prepared for metallographic observations using standard grinding and polishing techniques to obtain a final surface finish of ~0.05μm. The canister of Ti-6Al-4V alloy within which the Ti-6Al-4V-1B powder was packed for further processing (referred to as the 'boron free Ti-6Al-4V' from here on) enables an unbiased evaluation of the effect of TiB whiskers on the mechanical behavior of the Ti-6Al-4V matrix. The boron free Ti-6Al-4V region most closely resembles the properties of an unreinforced Ti-6Al-4V alloy

which has undergone the exact same processing conditions. A backscattered electron micrograph of the sample showing the microstructure of the transverse section of extruded Ti-6Al-4V-1B alloy along with the boron free Ti-6Al-4V region is given in Figure 3.9a. Figure 3.9b shows an optical micrograph along the extrusion direction showing both the regions.

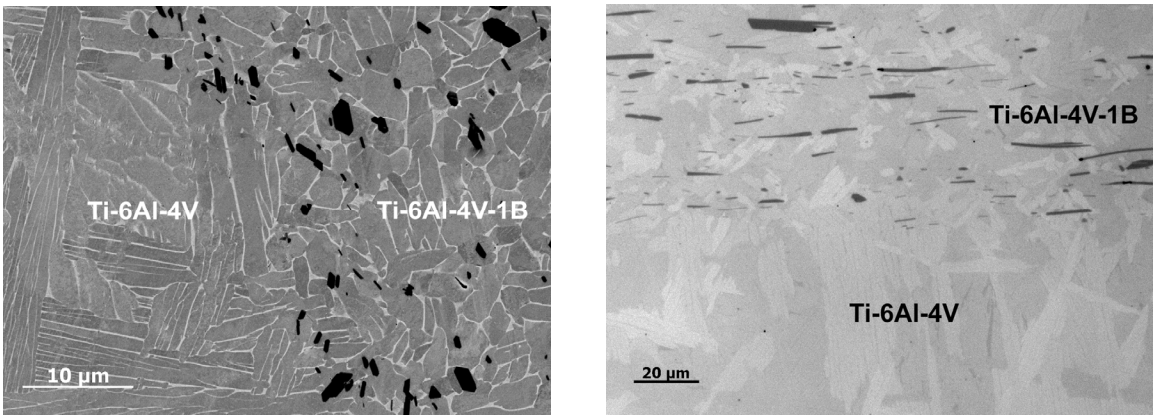

(a) (b)

Figure 3.9: (a) Backscattered electron micrograph of the transverse section and (b) optical micrograph of the longitudinal section of boron modified Ti-6Al-4V sample

The TiB whiskers that formed *in situ*, dark needle shaped phase with an average length of 23.4 µm and width of 3.4 µm, are aligned along the extrusion direction. The volume fraction of TiB whiskers is approximately 6%. The matrix microstructure consists of predominantly equiaxed α grains decorated with retained β phase at the grain boundaries. The TiB whiskers restrict the β grain growth at the extrusion temperature and also act as heterogeneous nucleation sites for the β → α phase transformation, both of which lead to fine grained matrix microstructure evolution. The boron free Ti-6Al-4V

region microstructure consists of lamellar α–β colonies in coarse β grains, which is as expected in Ti-6Al-4V after β processing.

3.3.2 Indentation Experiments

Microindentation experiments were carried out using a micro-hardness tester manufactured by CSM Instruments. The equipment has a load range of 0.03 – 30 N with 0.3 mN resolution and a maximum penetration depth of 200 μm with a depth resolution of 0.3 nm. Two different indenter geometries were used: a diamond Vickers pyramidal indenter (four sided pyramid with 136^0 included angle) and a diamond spherical tip of radius 19.28 μm (as measured after fabrication). It may be noted that spherical indenters are conical shaped with spherical tip of desired radius. Depth-controlled indentations of 8μm depth (which results in a penetration depth to indenter radius ratio of approximately 0.41) were performed on the Ti-6Al-4V matrix region of the extruded Ti-6Al-4V-1B alloy, sectioned and polished along the extrusion direction. The loading and unloading rates were kept the same at 1 N/minute. Twelve indentations were performed on the sample. To compare the indentation response of the matrix with that of unreinforced Ti-6Al-4V, twelve indentations with the same penetration depth and loading/unloading rate were carried out on the boron free Ti-6Al-4V region of the sample. Figures 3.10a and 3.10b show the SEM micrographs of the residual indent on the boron modified Ti-6Al-4V matrix and boron free Ti-6Al-4V region, respectively. Pile-up of material around the indent is clearly visible in both cases. The mean indentation response along with the 95% confidence intervals of both the matrix and the boron free Ti-6Al-4V region are shown in Figure 3.11.

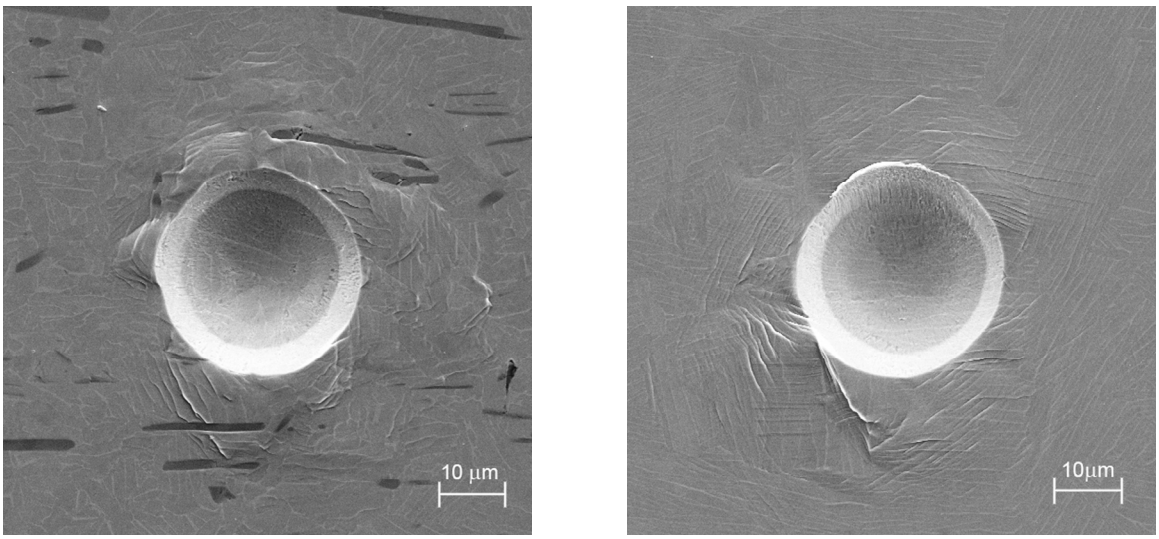

(a) (b)

Figure 3.10: SEM micrographs of the residual indent on (a) boron modified Ti-6Al-4V matrix and (b) boron free Ti-6Al-4V region

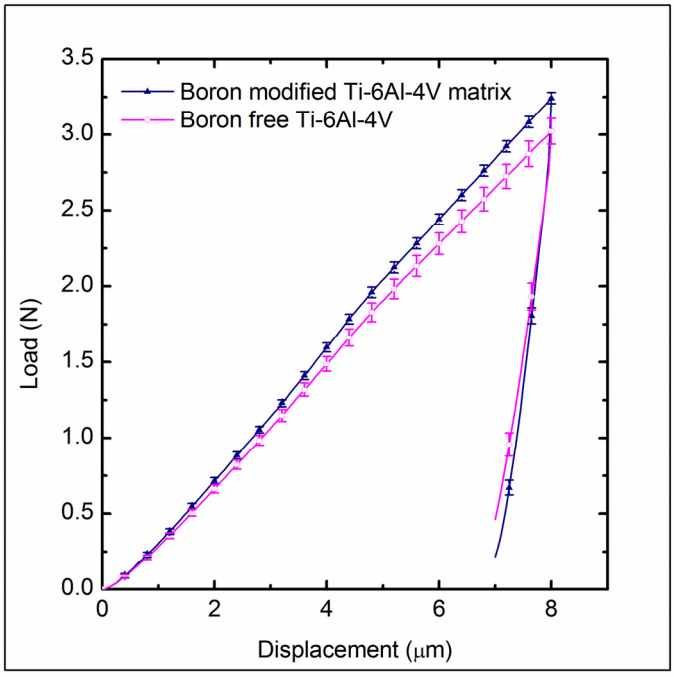

Figure 3.11: Mean indentation response along with the 95% confidence intervals of boron modified Ti-6Al-4V matrix and boron free Ti-6Al-4V region

As could be observed, while the indentation response of the matrix region is very consistent and reproducible, the boron free Ti-6Al-4V region shows more scatter in the indentation response. This may be attributed to the microstructural heterogeneity being of coarser length scale than the indentation area in the boron free region due to the presence of much coarser grains as compared to the matrix region. Further indentations were performed on both the matrix region and the boron free Ti-6Al-4V region using Vickers pyramid. This was done primarily to verify the results obtained using spherical indenter, as discussed later in this section. An optical micrograph of the residual indent from Vickers indenter on the boron modified Ti-6Al-4V matrix is given in Figure 3.12.

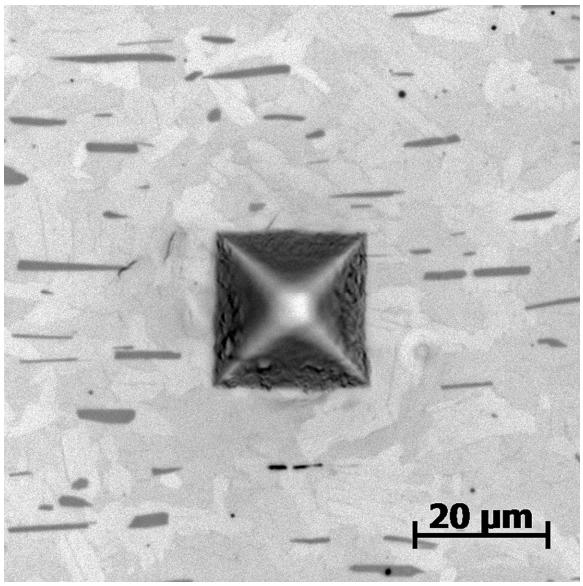

Figure 3.12: Optical micrograph of the residual indent on boron modified Ti-6Al-4V matrix

3.3.3 Constitutive Properties of Ti-6Al-4V Matrix

Local constitutive properties of Ti-6Al-4V matrix were deduced by incrementally varying the material constitutive properties in the FE indentation model until the

simulated load-depth curve matches the experimental curve in both loading and unloading regimes. The FE model was constructed in Abaqus as described in the previous sections. The material parameters $E = 115\ GPa$, $\nu = 0.33$, σ_y = 1025 MPa, and $n = 0.1$ were found to match the experimental indentation response of the Ti-6Al-4V matrix. Figure 3.13a shows both the mean experimental load-displacement curve and the FE simulated curve. These material parameters were used as the input for modeling the indentation response using the Vickers indenter. The indenter was modeled as a cone with a half-apex angle of 70.3^0 which gives the same projected area as the Vickers pyramid. The simulated load-displacement curve using the constitutive properties computed from the reverse analysis of spherical indentation shows excellent agreement with the experimental data as can be seen in Figure 3.13b. Reverse analysis for the boron free Ti-6Al-4V region yielded the material parameter set $E = 115\ GPa$, $\nu = 0.33$, σ_y = 975 MPa, and $n = 0.09$. The comparison of experimental and simulated load-displacement curves for both the spherical and Vickers indenter (simulated using constitutive properties computed from spherical indentation) are given in Figures 3.14a and 3.14b, respectively. It may be noted that the Vickers indentation response for both the boron modified Ti-6Al-4V matrix and boron free Ti-6Al-4V region are quite similar, which shows that Vickers indenter alone cannot be used to deduce the mechanical properties accurately. Contour plots of the equivalent plastic strain distribution on the indented sample at 5 μm indenter penetration depth for both spherical and Vickers indenters are given in Figure 3.15. Note that the matrix deformation behavior is different due to the differences in tip geometry.

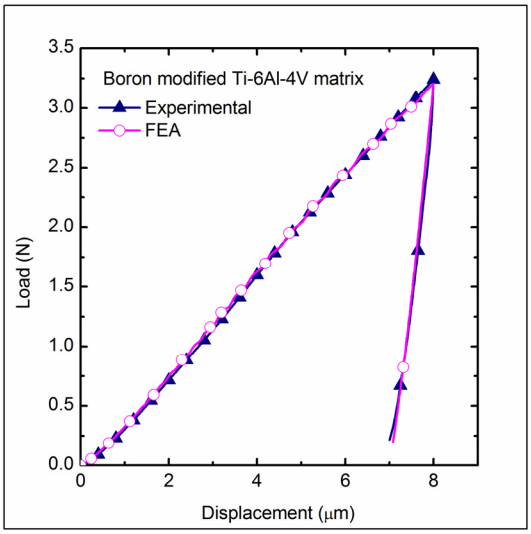

(a)

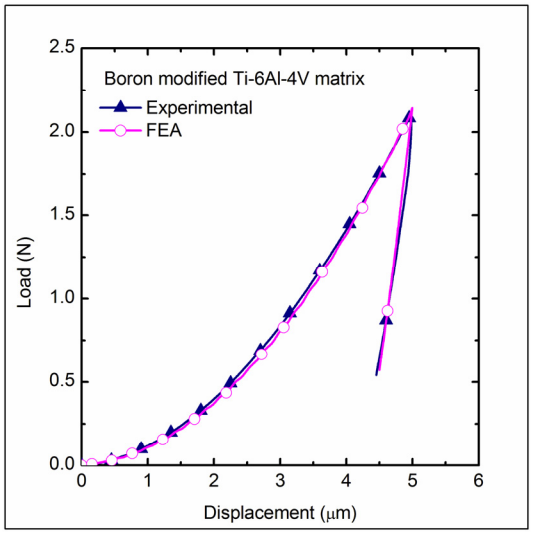

(b)

Figure 3.13: Comparison of experimental and simulated load-displacement curves for boron modified Ti-6Al-4V matrix with (a) spherical indenter and (b) Vickers pyramid

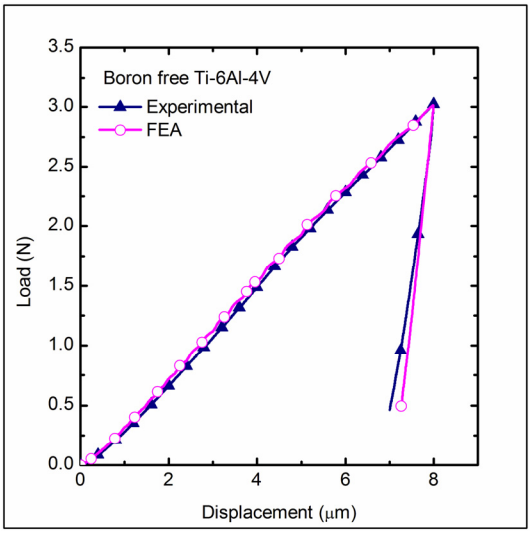

(a)

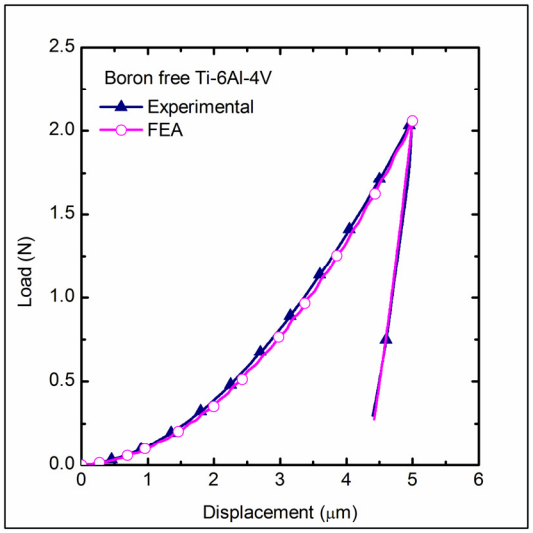

(b)

Figure 3.14: Comparison of experimental and simulated load-displacement curves for boron free Ti-6Al-4V matrix with (a) spherical indenter and (b) Vickers pyramid

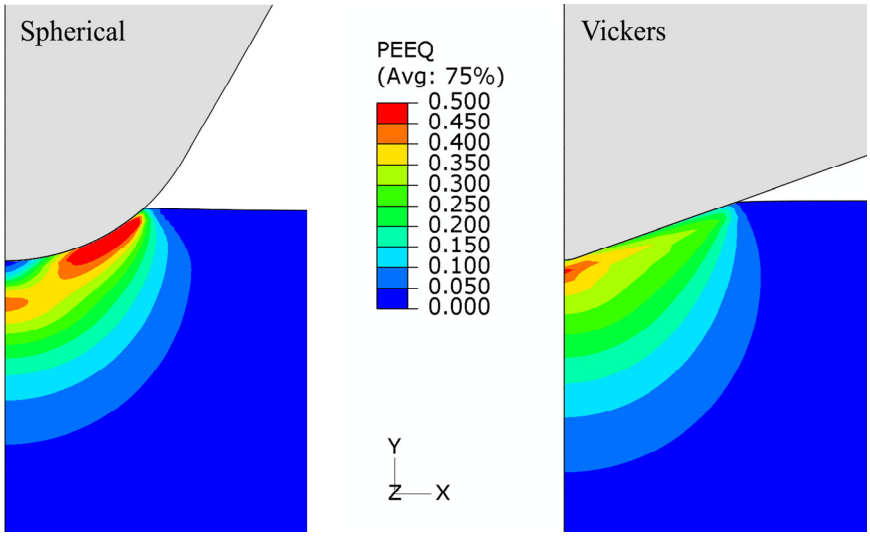

Figure 3.15: Contour plots of equivalent plastic strain distribution in Ti-6Al-4V matrix

Figure 3.16 shows the computed stress-strain curves for both the matrix and the boron free Ti-6Al-4V region along with the experimental curve for Ti-6Al-4V-1B alloy. The observed increase in yield strength of 50 MPa due to microstructural refinement and morphological change caused by boron addition is in close agreement with the analytical strength modeling results reported in the literature [100]. Note that the experimental curve includes the strengthening due to load sharing by the TiB whiskers whereas the computed curve takes into account only the strengthening due to grain refinement of the matrix due to boron addition.

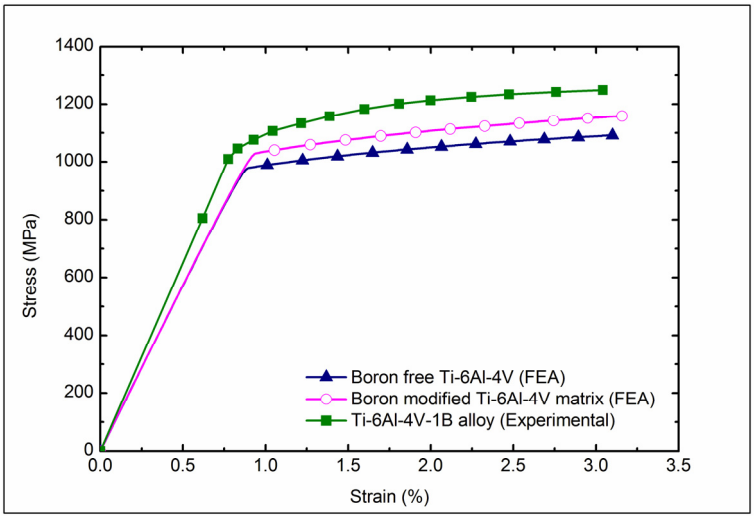

Figure 3.16: Computed stress-strain curves for both boron modified and boron free Ti-6Al-4V region along with the experimental curve for Ti-6Al-4V-1B alloy

3.4 Constitutive Properties of TiB

Because TiB is only stable within a titanium matrix and forms *in situ* during high-temperature processing, mechanical properties of this material cannot be measured by conventional methods such as tensile test. Gorsse and Miracle have analytically estimated the stiffness of TiB whiskers from bulk measurements of boron modified titanium alloys with the Halpin-Tsai equation to be 482 GPa [120]. Panda and Ravi Chandran determined the average modulus of TiB to be 427 GPa using density functional theory based first principles calculations [121]. Being a ceramic material with negligible plastic deformation (and consequently, negligible pile-up of material under indentation load), the elastic modulus of TiB can be determined directly from the indentation load-displacement data using Oliver-Pharr method with fair accuracy. As mentioned earlier, the TiB whiskers in Ti-6Al-4V-1B alloy have an average width of just 3.4μm, which makes it difficult to accurately put indents on the whiskers. It is also difficult to avoid the effect of the softer Ti-6Al-4V matrix underneath the whisker in the modulus value

obtained through indentation. Accordingly, the indentation experiments are performed on a hypereutectic Ti-6Al-4V-1.6B alloy, where along with the eutectic phase, TiB also forms as a primary phase directly precipitating from the liquid phase. The material was processed using a P/M route in the same way as described for the Ti-6Al-4V-1B alloy in an earlier section. Figure 3.17 shows an SEM image of the transverse section of an extruded Ti-6Al-4V-1.6B alloy.

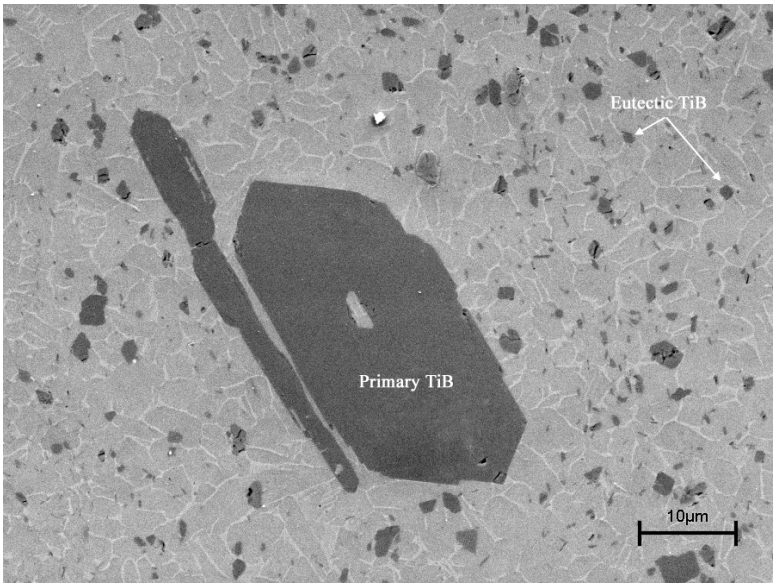

Figure 3.17: SEM image of the transverse section of an extruded Ti-6Al-4V-1.6B alloy

It may be noted that the particles of primary phase TiB are noticeably coarser than the eutectic TiB whiskers. The primary TiB particles, found with much less frequency in these samples (5-10 primary particles in an area containing more than 20,000 eutectic TiB whiskers), were observed to typically have a length of approximately 200-300 μm and a width of approximately 30-50 μm, with an aspect ratio range of between 4 and 10 [122]. The elastic modulus of primary TiB particles is expected to be same as that of the

eutectic TiB whiskers. Microindentation experiments were carried out on the transverse section of the primary TIB particles as described in the next section.

3.4.1 Microindentation of primary TiB

Displacement controlled microindentation experiments of 1 μm depth were performed on primary TiB whiskers on the transverse section of an extruded Ti-6Al-4V-1.6B alloy using Vickers pyramidal indenter with a loading/unloading rate of 1N/minute. Figure 3.18 shows an SEM image of the residual indent on a TiB whisker.

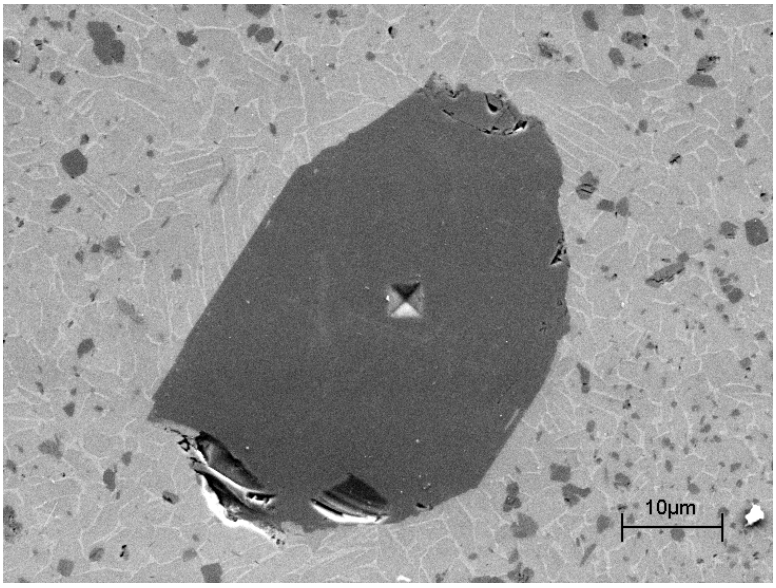

Figure 3.18: SEM image of the residual indent on a TiB whisker

As expected, no pile-up was observed near the residual indent area. Twelve indentations were performed on the same sample, but on different TiB whiskers. It is assumed that the primary TiB whiskers are sufficiently large and any substrate effects due to the softer Ti-6Al-4V matrix are negligible. The load-displacement curves from the

twelve indentations and the corresponding elastic modulus values obtained from Oliver-Pharr method are given in Figure 3.19a and Figure 3.19b, respectively.

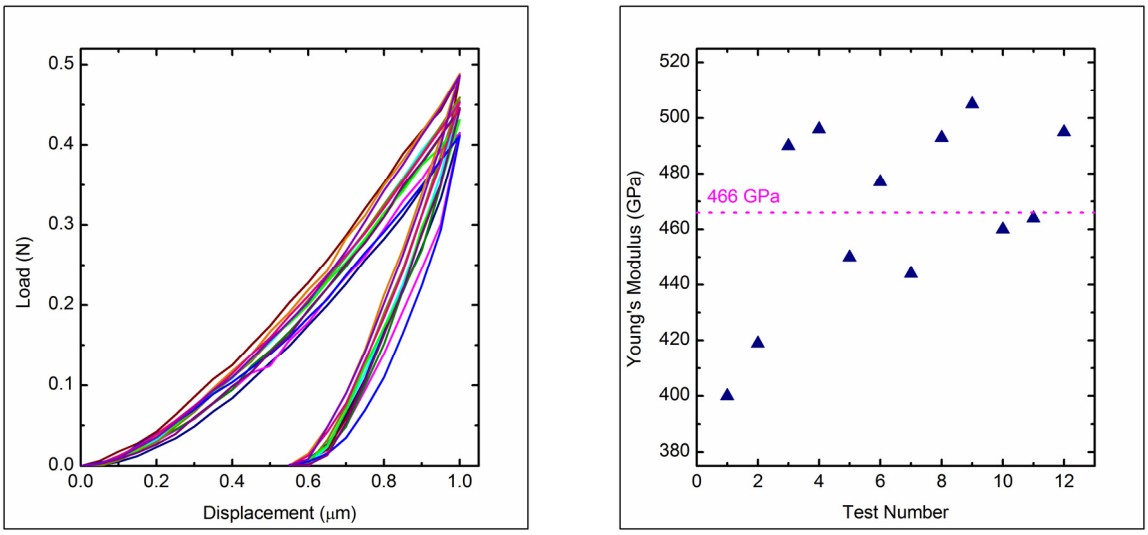

(a) (b)

Figure 3.19: (a) Load-displacement curves from twelve different indentations on TiB whiskers and (b) corresponding modulus values

Note that Oliver-Pharr method requires one to input the Poisson's ratio to compute the modulus of the material and the literature reported value of 0.15 [121] was used in this study. As can be observed from the figures, there is a wide variation in the load-displacement data and the computed elastic modulus values. The modulus values vary from 400 GPa to 505 GPa with an average value of 466 GPa. In order to determine whether the variation was caused by the microindentation apparatus or from the TiB whiskers, multiple indents were placed on the same primary TiB whisker, as shown in Figure 3.20a. The three indents showed consistent load-depth curves, as illustrated in Figure 3.20b. This suggests that the variation is not due to the apparatus, but is inherent in the different TiB whiskers in the Ti-6Al-4V-1.6B alloy specimen. The variation could

be attributed to the anisotropy of the primary TiB single crystal whiskers. In the extruded Ti-6Al-4V-1B alloy, most of the eutectic TiB whiskers are aligned parallel to the extrusion direction and are expected to have similar crystallographic texture, and consequently comparable values of modulus. Accordingly, in the present work, all the TiB whiskers were assumed to have a modulus value of 466 GPa. Note that this value is quite in agreement with the analytically determined values of TiB modulus reported in the literature [120, 121].

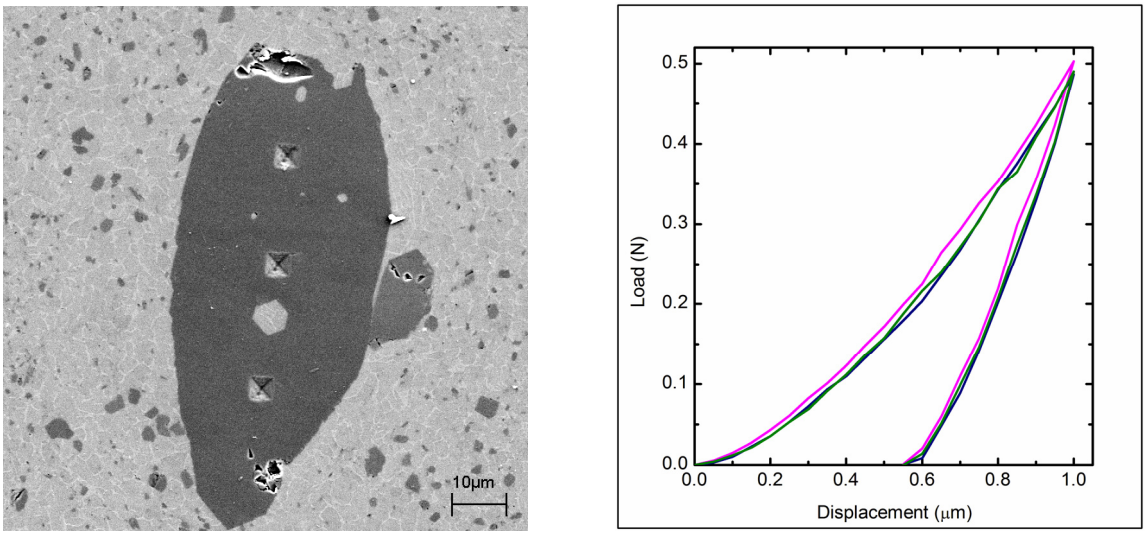

(a) (b)

Figure 3.20: (a) Multiple indents on a single TiB whisker and (b) corresponding load-displacement curves

3.4 Constitutive Properties of Al-6061 Alloy

3.4.1 Processing and Microstructure of DRA Composites

The DRA composites used for this research were fabricated by Dr. Spowart at AFRL, Materials and Manufacturing Directorate via P/M route using Al-6061 alloy (Al-

0.27Cu-0.26Fe-0.97Mg-0.56Si) as the matrix material. The reinforcement used was SiC particulate with a median particle size of 13.4 μm. Al-6061 alloy powders of three different median diameters, 26.8, 41.54 and 108.54 μm were used to produce composites having particle size ratios (PSR) of 2.0, 3.1 and 8.1. The effect of varying PSR values in the microstructure and properties of these materials were briefly discussed in Chapter 1 and will be revisited in detail in the next chapter. In order to reduce agglomeration due to electrostatic forces, the matrix and reinforcement powders were suspended in slurry using 1-butanol as the solvent during the blending stage. The powders were dried after blending, and placed in an extrusion canister made of Al-6061 alloy. In order to remove all traces of residual solvents from the powders, an elevated temperature vacuum de-gas treatment was used. The canisters were then sealed for compaction and extrusion. Extrusion was carried out at 450^0C with an extrusion ratio of 25:1 (round: round), followed by an air cool, i.e. the as-extruded (F) heat treatment [42]. The fabricated composite material contained approximately 28 volume % of SiC reinforcement particles. Figure 3.21 shows the typical microstructure of a 2.0 PSR DRA composite where the darker phase represents the SiC particles.

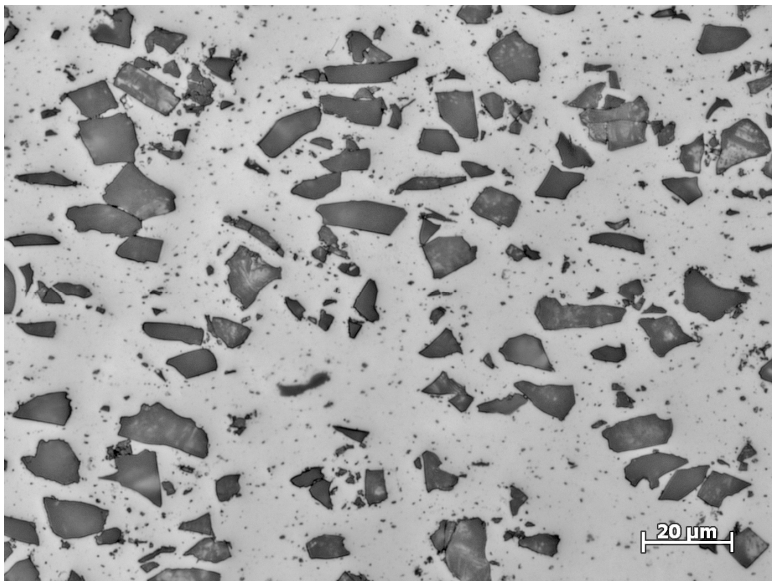

Figure 3.21: Typical microstructure of a 2.0 PSR DRA composite

3.4.2 Microindentation and Constitutive Properties

Because of the high volume fraction of SiC particles in the material, it is not possible to indent the matrix material to a sufficient depth (~ 8-10 μm, which is necessary to guarantee uniqueness of reverse analysis and avoid any size effects), while at the same time avoiding any effect of the SiC particles on the load-depth response of the matrix. The Al-6061 canister within which the matrix and reinforcement powder were packed for processing was used to perform indentation experiments. This region most closely resembles the properties of an unreinforced Al-6061 alloy which has undergone the exact same processing conditions. Spherical indentations (with indenter tip radius of 19.28 μm) of 10 μm depth were carried out and Figure 3.22a shows the load-displacement curves from 6 indentations. The load-displacement curves show negligible variation, as may be observed from the figure. Optical micrograph of a residual indent is shown in Figure 3.22b.

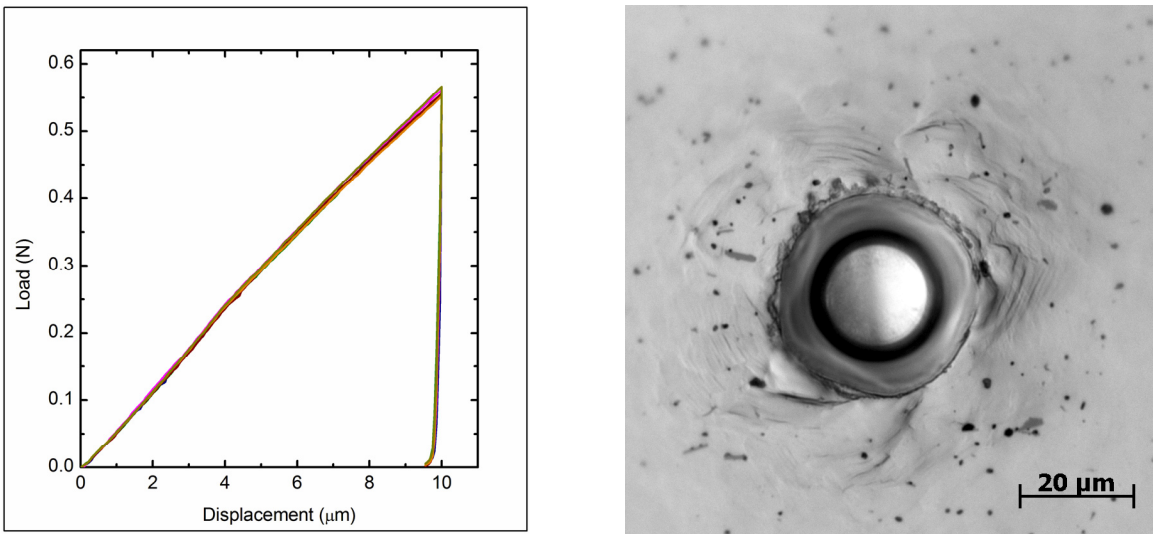

(a) (b)

Figure 3.22: (a) Load-displacement curves from spherical indentations on Al-6061 alloy and (b) optical micrograph of a residual indent

Reverse analysis using FEM was carried out in the same way as described earlier for Ti-6Al-4V alloy to deduce the constitutive properties of the as-extruded Al-6061 alloy. The material parameters $E = 70\ GPa$, $\nu = 0.33$, $\sigma_y = 71$ MPa, and $n = 0.185$ were found to match with the experimental indentation response of the Al-6061 alloy. Figure 3.23 shows both the mean experimental load-displacement curve and the FE simulated curve.

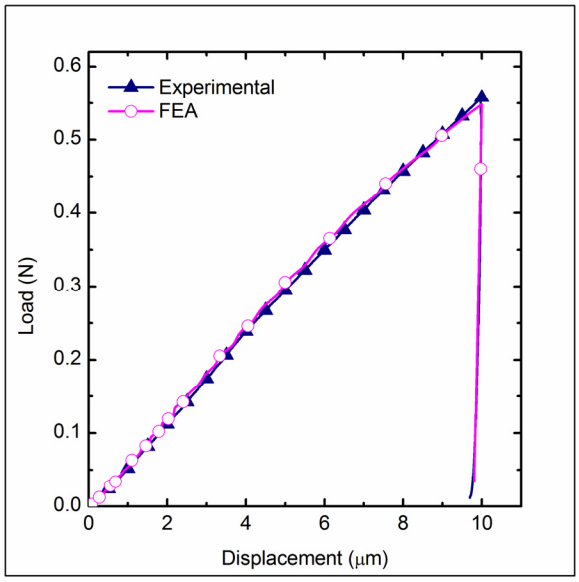

Figure 3.23: Mean experimental load-displacement curve and the FE simulated curve of Al-6061 alloy

3.5 Constitutive Properties of SiC Particles

In the DRA composites under investigation, the SiC reinforcement phase is present as equiaxed particles with a median size of 13.4 μm. The small size of these particles makes it difficult to use indentation to deduce the elastic modulus of the material because of the substrate effect. Additionally, the micro- and the nano-indenters used in this research lacked the precision required to accurately put indents on the SiC particles. Material properties of SiC have been widely researched over the last several decades and the reported elastic modulus value of 410 GPa and Poisson's ratio of 0.14 were used in this study [123].

3.6 Summary

Instrumented indentation, coupled with finite element analysis, was shown as a viable technique to determine the local constitutive properties of small microstructural

volumes. Details such as exact indenter tip geometry and friction between the indenter and the specimen were incorporated in the FE model for more realistic simulations. Spherical indentation with a penetration depth to indenter radius ratio of over 0.4 was used to compute the local constitutive properties of the Ti-6Al-4V matrix in a Ti-6Al-4V-1B alloy. It was found that small addition of boron to titanium alloys alter the microstructure, and thereby the constitutive properties, of the matrix. The spherical indentation response of the Ti-6Al-4V matrix region was shown to be different from that of an unreinforced alloy of similar composition and processing. The mechanical properties of both the matrix region and the boron free Ti-6Al-4V region were computed from the indentation response using finite element method. Microstructural changes resulting from the presence of TiB whiskers were shown to result in an yield strength increase of 50 MPa and a modest increase of 0.01 in the strain hardening exponent of the Ti-6Al-4V matrix alloy. Elastic modulus of TiB was computed as 466 GPa from the load-displacement data of Vickers indentation on primary TiB whiskers in a Ti-6Al-4V-1.6B alloy. Stress-strain curve of Al-6061 alloy in DRA composites was also computed using spherical indentation and finite element analysis.

CHAPTER 4

TWO-DIMENSIONAL MICROMECHANICAL SIMULATIONS

4.1 Introduction

The goal of micromechanics is to predict the macroscopic mechanical behavior of materials from an understanding of their microstructure. A relatively new branch of mechanics of materials, micromechanics involves application of continuum mechanics principles to individual phases in a heterogeneous material and the use of analytical and/or numerical methods to compute the macroscopic responses. Micromechanical analyses detailed in this thesis primarily involves finite element based uniaxial loading simulation of two-phase material systems containing a matrix phase and a reinforcement phase. Almost all of the reported micromechanical studies on two-phase composite material systems involve isotropic microstructures with uniform random distribution of the reinforcement phase in the matrix. But a number of emerging and technologically important composite material systems exhibit controlled anisotropy and spatial non-uniformity depending on the desired behavior for the end product. Two such powder metallurgy processed material systems are considered in this thesis, namely, discontinuously reinforced aluminum composites and boron modified titanium alloys.

This chapter deals with two-dimensional (2D) simulations where representative volume elements of 2D microstructures are incorporated in FEA to investigate the mechanical response. Qualitative microstructural observations of the materials under study are given in the first section which is followed by the use of two-point correlation functions to determine a statistically representative volume element for these

microstructures. Later sections describe the methodology developed for incorporating the microstructures in a finite element framework along with the results and comparison with experimental data.

4.2 Microstructural Observations

4.2.1 DRA Composites

Three different samples of the DRA composites, each with a different matrix to reinforcement particle size ratio (PSR) of 2.0, 3.1, and 8.1, were available for this work. As reported in Chapter 2, PSR is an important processing parameter that controls the homogeneity of the reinforcement particle distribution in these composites manufactured via powder metallurgy route. Increasing the PSR (increasing the average size of the aluminum alloy matrix powder and keeping the SiC particle size the same) leads to a reduction in the combined surface area of the matrix alloy particles and as this area becomes insufficient for a uniform arrangement of reinforcement particles, clusters of SiC particles are formed in-between the larger matrix particles. Standard metallographic procedures were used to observe the material microstructure along the longitudinal section of the extruded samples. Note that the longitudinal section contains the extrusion axis of the sample. Figures 4.1a, 4.1b, and 4.1c show low-resolution micrographs of the longitudinal section of the DRA samples with PSR value of 2.0, 3.1, and 8.1, respectively. The sample with PSR 2.0 is relatively homogeneous whereas long-range heterogeneity caused by clustering of SiC particles is observed with increasing PSR values.

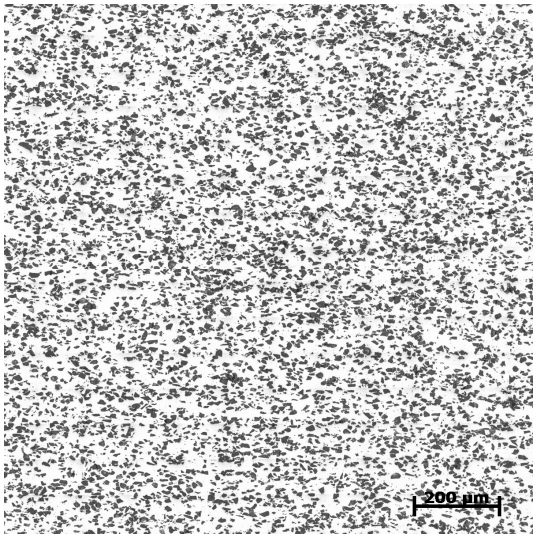

(a)

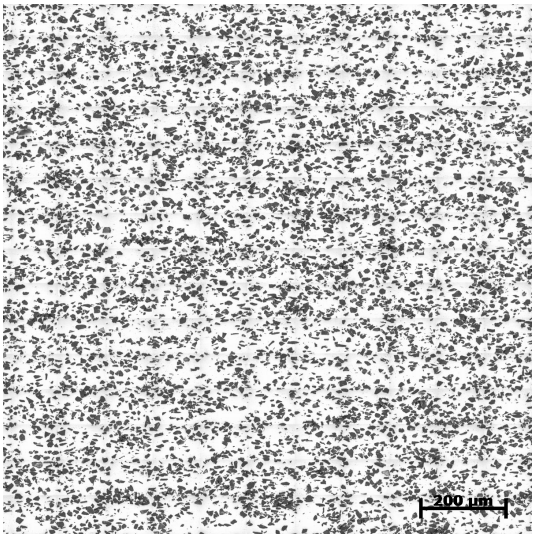

(b)

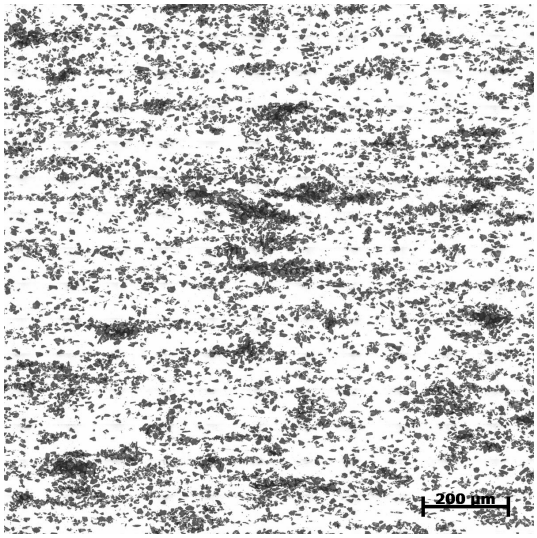

(c)

Figure 4.1: Low-resolution optical micrographs of the DRA composites with PSR value of (a) 2.0 (b) 3.1 and (c) 8.1

A high-magnification single field of view optical micrograph, in such cases, fails to capture the long-range spatial information. Hence it is necessary to obtain large areas of microstructural images at sufficiently high resolution, capturing the heterogeneity at all

relevant length scales while at the same time preserving information on individual particle morphologies, in order to perform any meaningful simulation of material microstructures. Using modern digital image analyzers it is possible to create a seamless 'montage' of a very large number of contiguous microstructural fields of view where each image is captured at a high enough magnification to resolve all the features of interest. Figure 4.2a shows such a large-area high-resolution montage (compressed here for visualization) of the 8.1 PSR microstructure [124]. The montage encompasses an area of 1 mm^2, at a resolution of 0.2 μm. The clustering of SiC particles aligned along the extrusion axis, as can be observed in the montage image, is clearly not captured in a single field of view (Figure 4.2b).

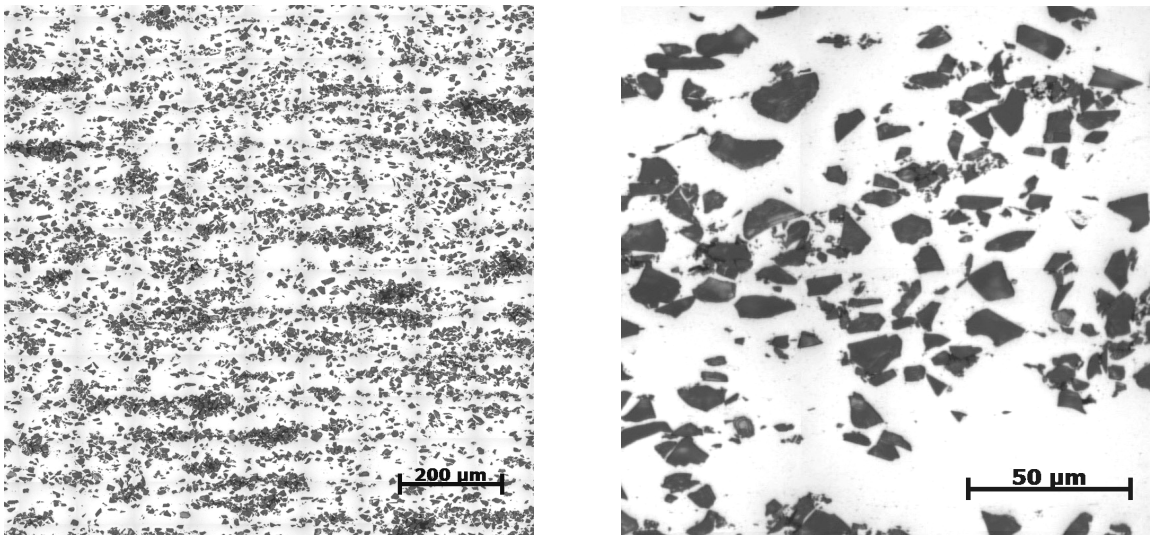

(a) (b)

Figure 4.2: (a) Montage image of 8.1 PSR microstructure covering an area of 1 mm^2 at 0.2 μm resolution and (b) magnified view showing the SiC particle morphologies

4.2.2 Boron modified Ti-6Al-4V Alloy

Micromechanical response of extruded Ti-6Al-4V-1B alloy (all compositions are in weight percent) produced via a pre-alloyed powder metallurgy approach was investigated in this research. Large-area high-resolution montage images of 1 mm^2 area were created, in a similar fashion as described earlier for DRA composites. Figure 4.3 shows the montage image of a longitudinal metallographic section of the alloy containing the extrusion axis [122]. Extrusion direction is along the horizontal axis of the image and the TiB whiskers can clearly be seen aligned along the extrusion axis.

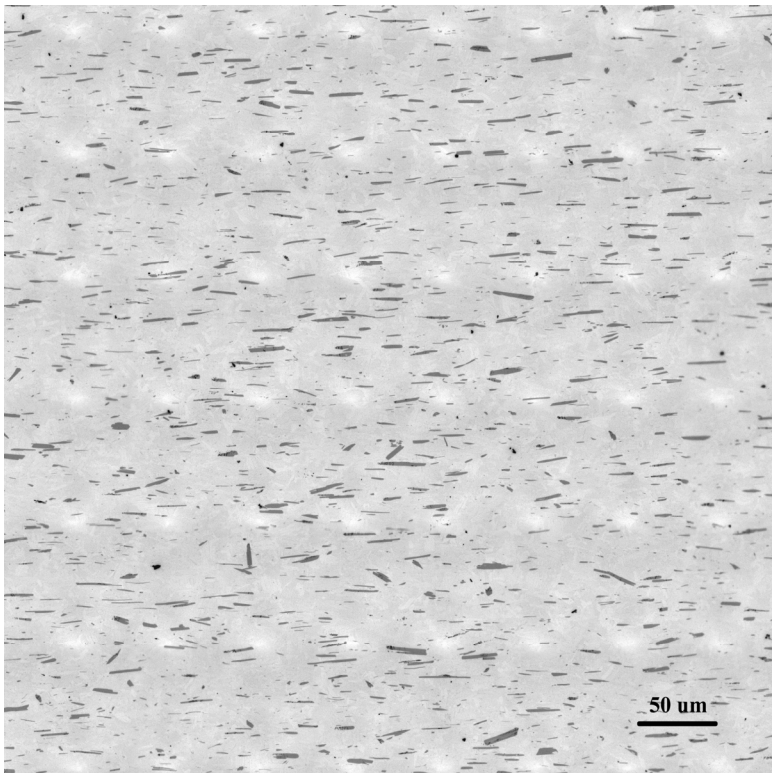

Figure 4.3: Montage image of extruded Ti-6Al-4V-1B microstructure covering an area of 500 μm x 500 μm at 0.2 μm resolution

4.3 Statistically Representative Volume Element

The selection of Representative Volume Element (RVE) is one among the most important decisions to be made in the modeling of random heterogeneous microstructures. The size of an RVE depends on the geometry of the microstructure as well as the physical property that is being investigated in the model. For example, the RVE for a microstructure exhibiting long-range spatial non-uniformities will be larger than that for an isotropic microstructure Also, the RVE size required for mechanical response simulation of a given material microstructure is not necessarily the same as the RVE size for thermal conductivity analysis of the same material. An RVE in its strict sense is applicable only for a periodic microstructure where the RVE is the same as the unit cell i.e., the smallest cell of periodicity. For stochastic microstructures, statistical descriptors can be used to arrive at a statistically equivalent representative volume element for computational studies [17-19, 125]. But none of the reported studies involve microstructures with long-range spatial correlations such as those observed in the microstructures under investigation in this work, particularly the DRA composite with 8.1 PSR value. Previous research within the author's group at Georgia Tech has shown that two-point correlation functions are well suited for quantifying both short-range and long-range spatial arrangements in two-phase material microstructures [91, 97]. But the applicability of such statistical descriptors in determining the RVE size for material microstructures has not been investigated earlier. Two-point correlation functions were used in this study to arrive at the smallest microstructural window that is statistically similar to the global material microstructure. The statistically representative microstructural windows were then incorporated in a finite element framework for further

analyses. In the present context, a microstructural window was regarded as the RVE provided it satisfied the following requirements:

- The chosen microstructural window is statistically representative of the entire material, i.e., the two-point correlation functions of the window are identical (within the stochastic variations) to that of the entire material microstructure. Note that matching these functions implicitly takes into account the first order microstructural attributes such as the volume fraction and size distribution of the phases.
- The global stress-strain behavior and the local stress and strain distributions of the chosen window are identical to that of the entire microstructure and they do not vary depending on the location of the chosen window or the nature of boundary conditions applied.

Large-area high-resolution montage images were used to measure the two-point correlation functions for DRA composites and boron modified titanium alloys. As discussed earlier, for a two-phase microstructure, only one of the four possible two-point correlation functions is independent. Therefore, only P_{11}, which represents the two-point correlation functions for the reinforcement phase (SiC in DRA composites and TiB in boron modified titanium alloys) was investigated in this research. For the measurements, the grayscale digital images were converted to binary images using KS 400, an image processing program from Carl Zeiss. Figure 4.4 shows a grayscale image of 8.1 PSR DRA microstructure and the corresponding binary image after image processing.

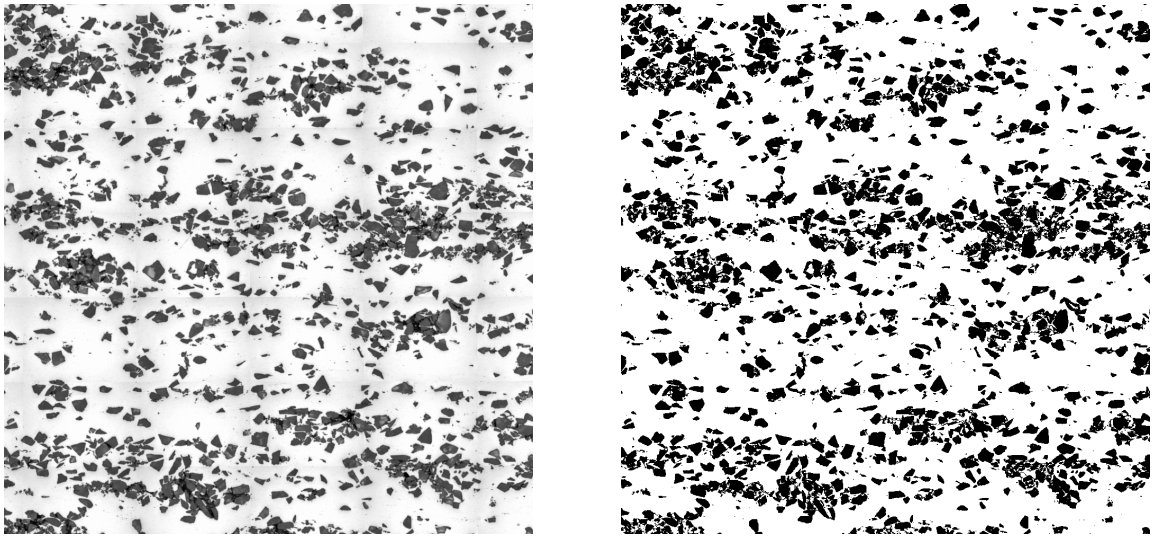

(a) (b)

Figure 4.4: (a) Grayscale image of 8.1 PSR microstructure and (b) corresponding binary image

4.3.1 DRA Composites

As discussed earlier, DRA composites with a high PSR value exhibit clustering of SiC particles and have long-range spatial correlations. Figure 4.5 shows the comparison of two-point correlation functions for the SiC phase (P_{11}) measured along the extrusion direction ($\theta = 0$) for the DRA microstructures with PSR values of 2.0, 3.1 and 8.1 on montage images of area 1 mm x 1mm [91]. The correlation functions are shown for lengths up to 350 μm (data for 50 -350 μm is given in the inset). The two-point correlation functions measured along the transverse direction ($\theta = \pi/2$) for lengths up to 80 μm are shown in Figure 4.6.

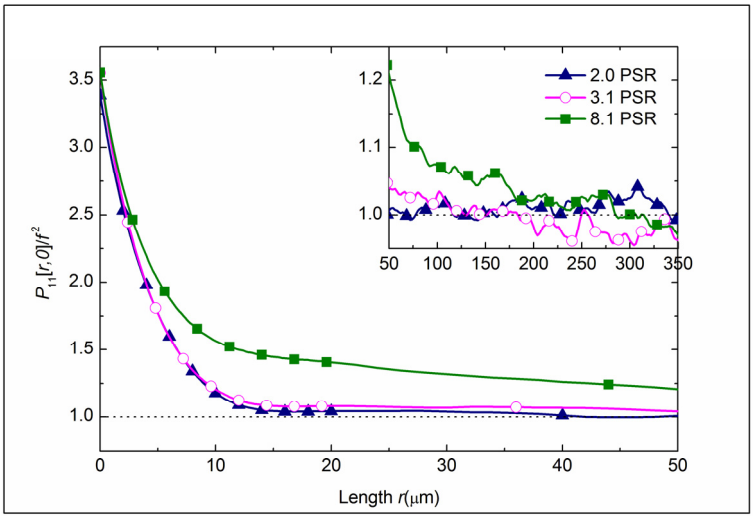

Figure 4.5: Two-point correlation functions for the DRA composites measured along the extrusion direction [91]

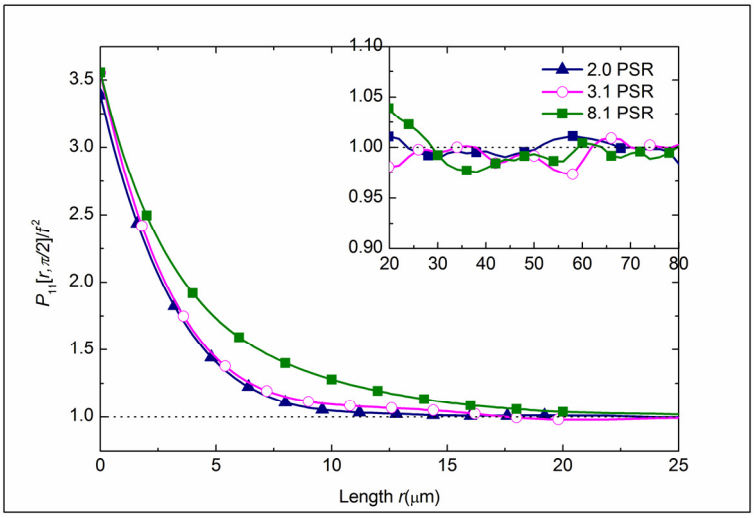

Figure 4.6: Two-point correlation functions for the DRA composites measured along the transverse direction [91]

Note that the two-pint correlation data has been normalized by the square of volume fraction of SiC particles, f^2. By definition, the two-point correlation function approaches the square of volume fraction of the phase under consideration (or unity, as in this case, when normalized by the square of the volume fraction) as r approaches infinity. For a

given DRA microstructure, this means that when the normalized two-point correlation function for SiC particles approaches unity at length *r*, the particles at either ends of a line of length *r* are no longer spatially correlated to each other. In other words, the distance at which normalized two-point correlation function approaches unity is an indicator of the characteristic length scale of the whole microstructure. Couple of observations can be made from the figures as listed below:

The two-point correlation function clearly brings out the differences in spatial distribution of the SiC particles in the three samples. For both longitudinal and transverse directions, the function approaches unity at the shortest distance for the 2.0 PSR microstructure, followed by 3.1 PSR and 8.1 PSR microstructures. This is to be expected as the spatial distribution of SiC particles is the most uniform in 2.0 PSR microstructure and the most clustered in 8.1 PSR microstructure.

For all the three microstructures, the two-point correlation function approaches unity at a shorter distance along the transverse direction compared to the longitudinal direction. This suggests that the characteristic length scale of the microstructures is of the order of SiC particle size (~ 15 μm) along the transverse direction whereas it is of the order of the SiC cluster size (~ 250 μm for 8.1 PSR microstructure) along the longitudinal direction. This may be attributed to the anisotropy introduced by the extrusion. As mentioned earlier, the extrusion direction is along the longitudinal axis and the SiC clusters tend to get aligned along the extrusion direction creating a banded structure.

Since 2.0 and 8.1 PSR microstructures represent the extremities, only these two samples will be further investigated in this research. Statistically representative microstructural window size can be determined by reducing the window size sequentially

until the two-point correlation functions deviate from that of a $1mm^2$ montage image. By keeping the $1mm^2$ montage image as the standard against which smaller windows are compared, it is implicitly assumed that the montage image is representative of the material in its entirety. In order to ascertain that this is indeed the case, two-point correlation functions were measured on five different 1 mm^2 montage images of 2.0 and 8.1 PSR microstructures. Figure 4.7 shows the correlation functions along the longitudinal direction for 2.0 PSR microstructure. Inset shows the long-range correlations up to 100 μm. The correlation functions for 8.1 PSR microstructure for up to 350 μm are given in Figure 4.8. While the correlation functions for the 2.0 PSR microstructures show insignificant variation, the same cannot be said about the 8.1 PSR microstructures where up to 10% variation is observed between the different realizations. This could be attributed to the inherent stochastic variations in this highly heterogeneous microstructure. Therefore, a 1 mm^2 montage image can be considered as statistically representative of the whole microstructure, i.e., a *microstructural RVE* for both 2.0 and 8.1 PSR DRA composites. It needs to be determined whether or not smaller window sizes will suffice as an RVE.

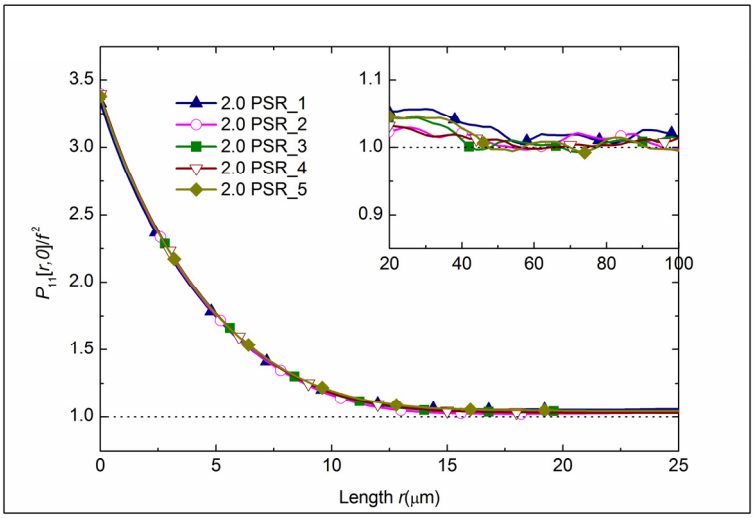

Figure 4.7: Two-point correlation functions for five different realizations of 1 mm x 1mm 2.0 PSR microstructure

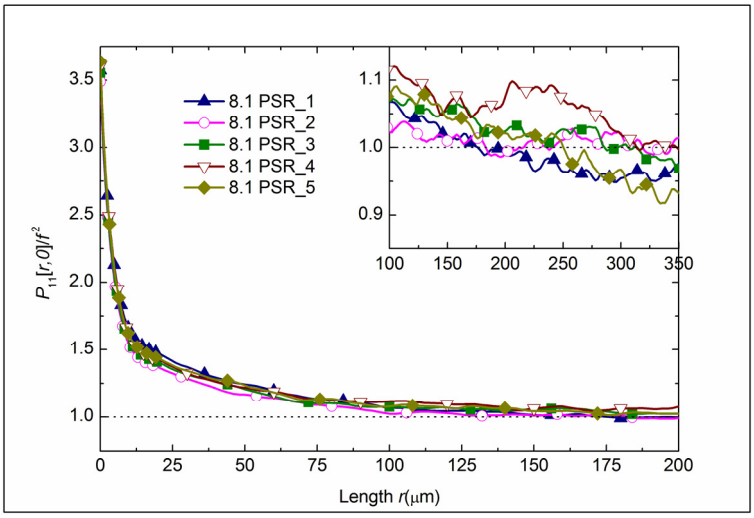

Figure 4.8: Two-point correlation functions for five different realizations of 1 mm x 1mm 8.1 PSR microstructure

4.3.1.1 Statistically Representative Window Size for 8.1 PSR Microstructure

Two-point correlation functions were measured for randomly picked square microstructural windows of edge lengths 1000 μm, 500 μm, 400 μm, and 300 μm. Edge effects that may arise at smaller window sizes were avoided by performing the

measurements on a virtual frame of desired window size within the large montage image such that right and top edges of the montage image (since the measurements are made only at 0^0 and 90^0 in this study) are at least 300 μm away from the corresponding edges of the chosen frame. Figure 4.9 illustrates this concept by showing the chosen location for a microstructural window of edge length 500 μm within a montage image. This allows for the measurement of correlation functions for all the pixels in the small frame for up to 300 μm without any edge effects. The choice of 300 μm is made as the two point correlation function approaches unity between 200-300 μm for 8.1 PSR montage images. Figure 4.10 shows the two-point correlation functions for up to 300 μm along the extrusion direction for the four microstructural windows. Note that for microstructural windows of size 400 μm and 300 μm, the two-point correlation functions deviate from that for 1000 μm size image in both short-range (0 – 100 μm) and long-range (100 – 350 μm) while the 500 μm window correlation functions deviate only at the long-range, beyond 200 μm. Figure 4.11 gives the two-point correlation functions for five different realizations of 500 μm x 500 μm window sizes. On comparison with Figure 4.8, it may be observed that while the two-point correlation functions for the five different 500 μm edge length windows are in good agreement with that of the larger montage images for most part, more scatter is observed at larger distances (beyond 200 μm). Note that the Y-axis scale is different for the long-range correlation functions in figures 4.8 and 4.11. But such small variations in the long-range correlation functions do not necessarily affect the mechanical response of the microstructure, as shown later in this chapter.

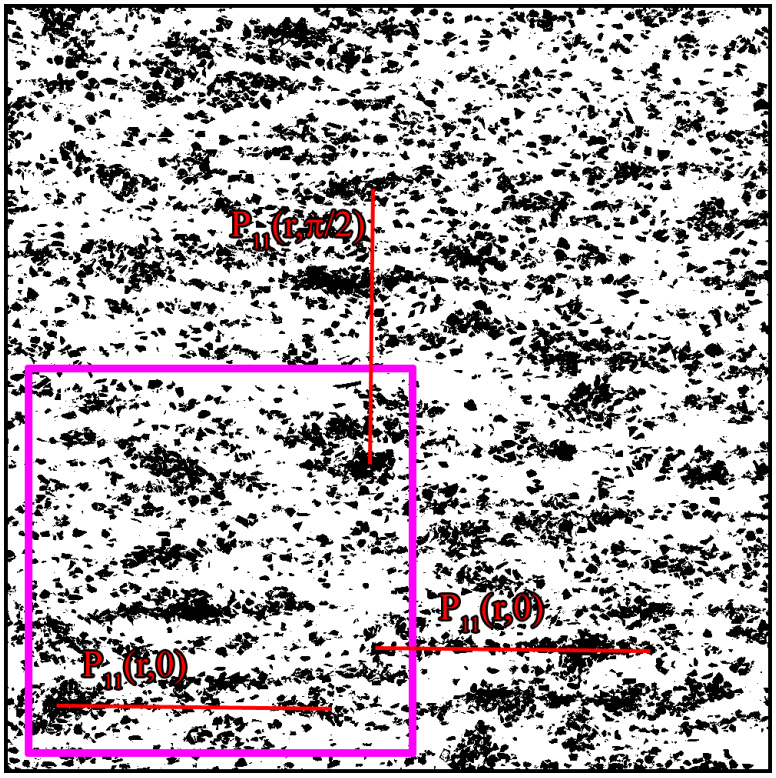

Figure 4.9: Measurement frame for two-point correlation functions

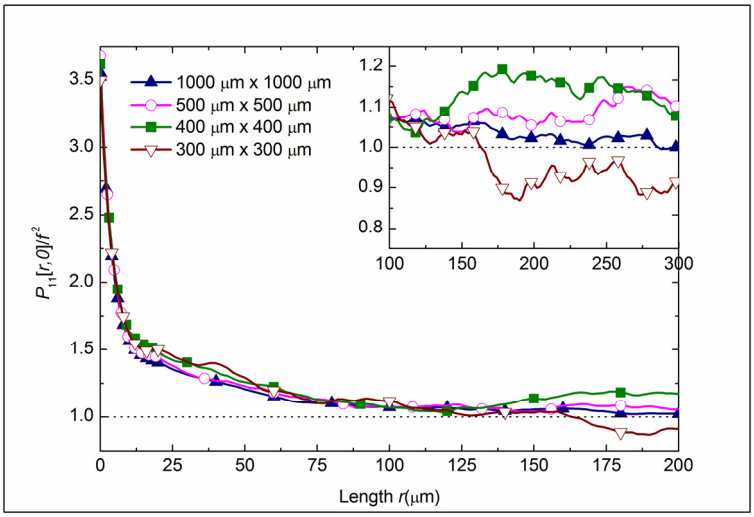

Figure 4.10: Two-point correlation functions for 8.1 PSR microstructural windows of varying sizes

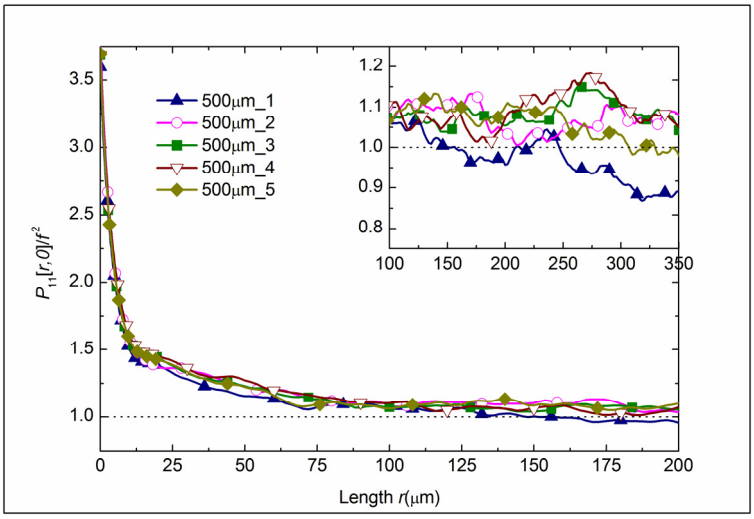

Figure 4.11: Two-point correlation functions for five different 500 μm x 500 μm 8.1 PSR microstructural windows

4.3.1.2 Statistically Representative Window Size for 2.0 PSR Microstructure

Being a more uniform microstructure compared to the 8.1 PSR composite, the statistically representative window size for the 2.0 PSR microstructure is expected to be much smaller than 500 μm. Figure 4.12 shows that the deviation in two-point correlation functions from the large montage image of 1000 μm edge length is less than 10% even for a window size as small as 200 μm. While a much smaller microstructural window may be used for micromechanical studies of 2.0 PSR microstructure, the RVE size determined for 8.1 PSR microstructure was used for the 2D FE modeling of the 2.0 PSR microstructure as well in this chapter for fair comparison between the results.

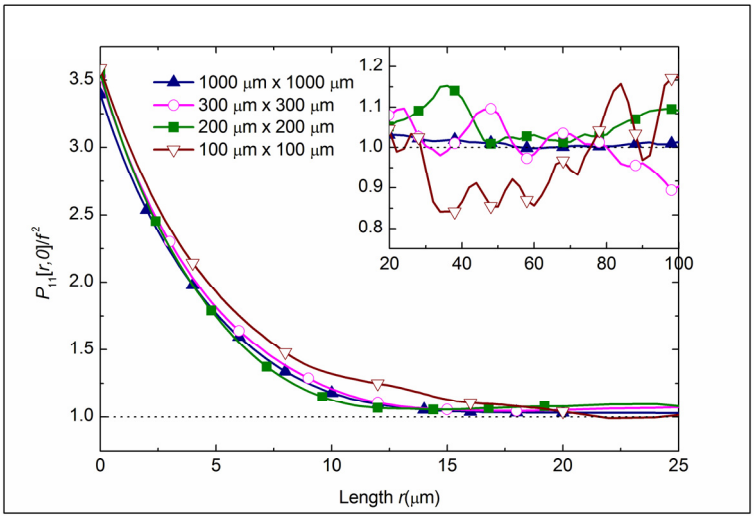

Figure 4.12: Two-point correlation functions for 2.0 PSR microstructural windows of varying sizes

4.3.2 Ti-6Al-4V-1B Alloy

Microstructure of Ti-6Al-4V-1B alloy, while anisotropic due to the extrusion process, is fairly uniform with no noticeable long-range spatial correlations as may be seen from Figure 4.3. Two-point correlation functions for the TiB phase were measured on a 1 mm^2 area montage image containing the extrusion axis. Figure 4.13a shows the normalized functions along the longitudinal (extrusion direction) and transverse directions. Note that the normalized two-point correlation functions approach unity at lengths of the order of TiB whisker size (average length of 23.4 μm and width of 3.4 μm) along both directions. This suggests that the characteristic length scale of the microstructure is of the order of whisker size and no long-range spatial correlations exist in this microstructure. The observation is more apparent in Figure 4.13b which shows the same plot when the *X* axis is normalized with the whisker size (whisker length for correlation functions along the longitudinal direction and whisker width for transverse direction).

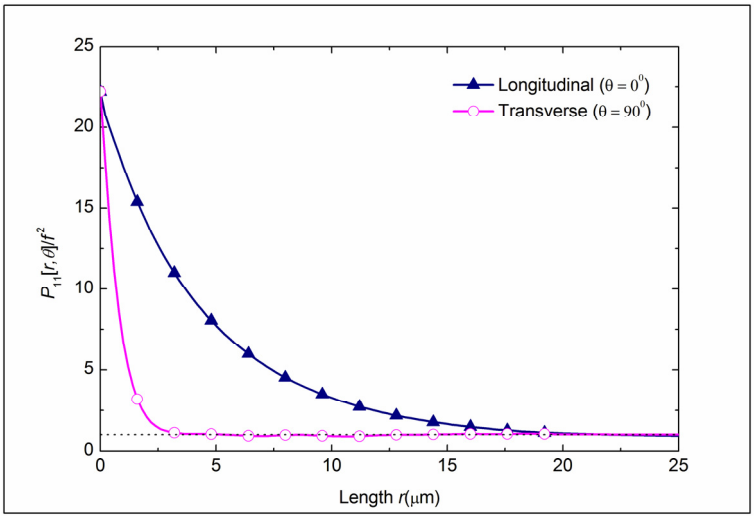

(a)

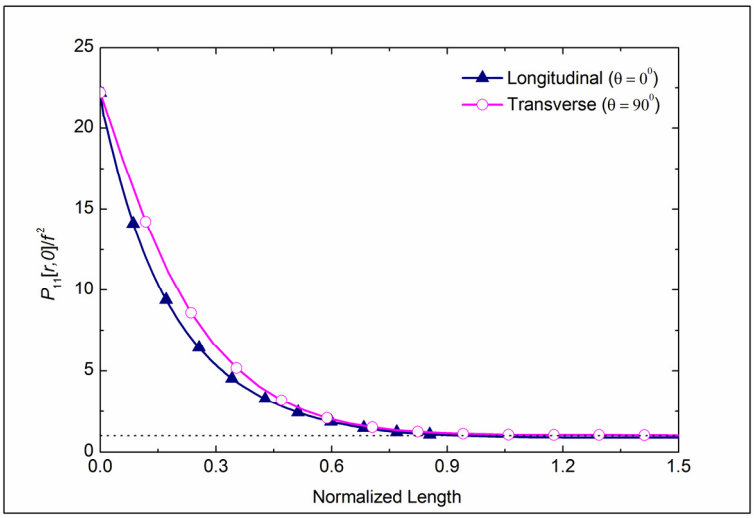

(b)

Figure 4.13: (a) Normalized two-point correlation functions along longitudinal and transverse directions for Ti-6Al-4V-1B alloy and (b) *X* axis of Figure 4.13a normalized with whisker size

Accordingly, it may be argued that the representative volume element for this microstructure is much smaller than the one required for DRA composites. Figure 4.14

shows that a window size as small as 200 μm x 200 μm can be considered statistically representative of the microstructure.

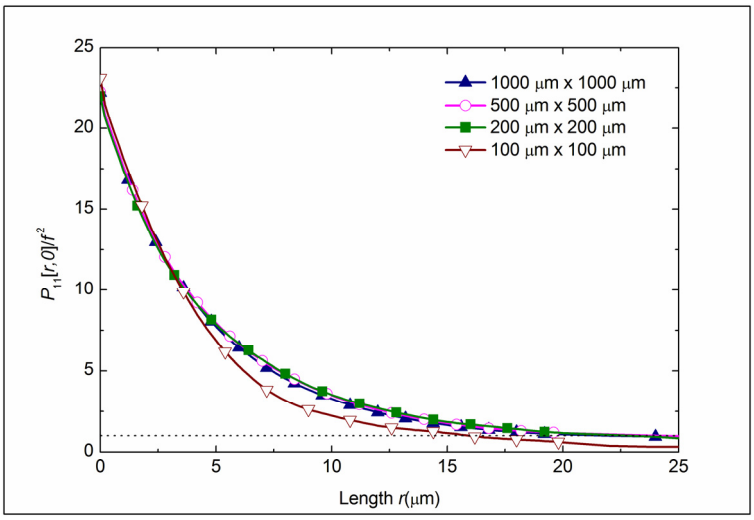

Figure 4.14: Two-point correlation functions for Ti-6Al-4V-1B microstructural windows of varying sizes

4.4 Finite Element Analysis of Real Microstructures

4.4.1 Meshing of Microstructures

In the current research, two-dimensional digital microstructural images were incorporated into finite element modeling framework using OOF, a public-domain software developed at NIST specifically to mesh and analyze real microstructural images. Figure 4.15 illustrates the steps involved creating a mesh using OOF by taking a small microstructural field of view of DRA composite as an example. Binary image of the microstructure (Figure 4.15a) is imported into the program and material properties are assigned to different phases depending on the grayscale value of each pixel. The initial mesh is created as a regular array of equilateral triangular elements as shown in Figure 4.15b. This mesh is adapted to the microstructure by an 'adaptive meshing' procedure,

which allows selective refining of the elements at the interface between the two phases and movement of the nodes to conform to the underlying microstructure. The FE mesh at an intermediate step during adaptive meshing is shown in Figure 4.15c and Figure 4.15d shows the final mesh which conform quite well to the original microstructure. The element size at the matrix/SiC interface is of the order of 1 μm.

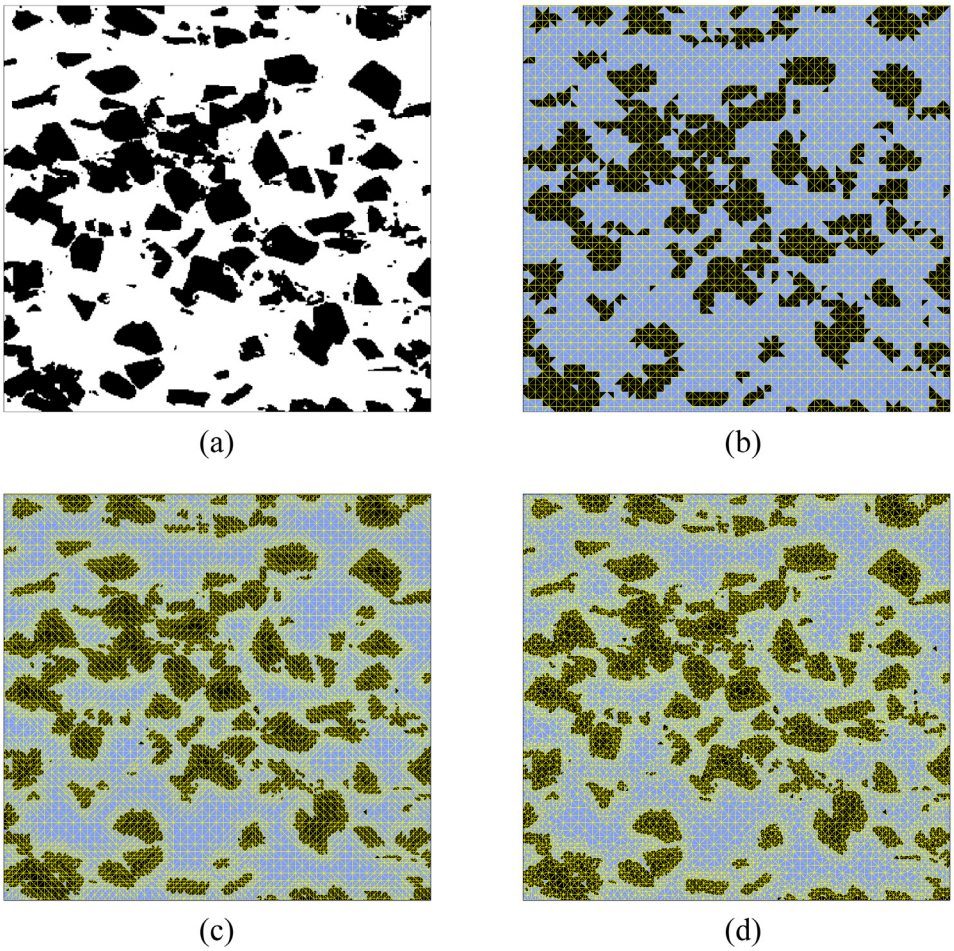

Figure 4.15: Steps involved in creating a finite element mesh using OOF (a) binary image (b) initial mesh (c) mesh at an intermediate step and (d) final mesh

The mesh density shown in these figures was used all the 2D analyses conducted on DRA composites in this study, unless otherwise mentioned. The FE mesh created in OOF was

exported to Abaqus for the micromechanical analysis. Though OOF has in-built modules to conduct FE analysis, Abaqus was used in this study because of the additional flexibility offered by the program in defining material models, boundary conditions and post-processing of results.

4.4.2 Finite Element Model

A modified embedded cell model, where a sufficiently large real microstructural image is embedded in a homogeneous composite medium, was used to study the 2D micromechanical response to uniaxial loading of these composites. The embedding allows for the effect of the rest of the material on the behavior of the cell. It also makes it easier to apply periodic boundary conditions, as described later in this section. The embedding method is a self-consistent procedure, which requires several iterations. An initially assumed stress-strain curve is first assigned to the embedding composite in order to perform the first iteration. An improved stress-strain curve of the composite will be obtained by analyzing the average mechanical behavior of the embedded cell. This procedure is repeated until the calculated stress-strain curve from the embedded cell is almost identical to that from the previous iteration. Mesh convergence and the effect of linear vs. quadratic interpolation of elements were studied using a 500 μm x 500 μm 8.1 PSR microstructure embedded in homogeneous composite medium of width 125 μm along all the four edges of the microstructure. Periodic boundary conditions as outlined in van der Sluis et al. [33] were employed in the simulations. These conditions require the model to deform in such a way that the opposing faces would fit together seamlessly upon translation in either *x* or *y* direction at any instance during or after deformation. The

boundary conditions are implemented in Abaqus by specifying the following displacement constraints using the *EQUATION option in Abaqus.

$$\begin{aligned} \boldsymbol{u}_{Top} - \boldsymbol{u}_{Bottom} &= \boldsymbol{u}_{TopLeft} - \boldsymbol{u}_{BottomLeft} \\ \boldsymbol{u}_{Right} - \boldsymbol{u}_{Left} &= \boldsymbol{u}_{BottomRight} - \boldsymbol{u}_{BottomLeft} \\ \boldsymbol{u}_{TopRight} - \boldsymbol{u}_{BottomRight} &= \boldsymbol{u}_{TopLeft} - \boldsymbol{u}_{BottomLeft} \end{aligned} \tag{11}$$

where *Top*, *Bottom*, *Right*, and *Left* represent the set of surface nodes on the corresponding edges in the model, excluding the corner nodes. The corner nodes are represented by *TopLeft*, *BottomLeft*, *BottomRight*, and *TopRight* respectively depending on the intersection of the two faces making up that particular corner. Figure 4.16 shows a schematic of the deformation behavior of a model with periodic boundary conditions.

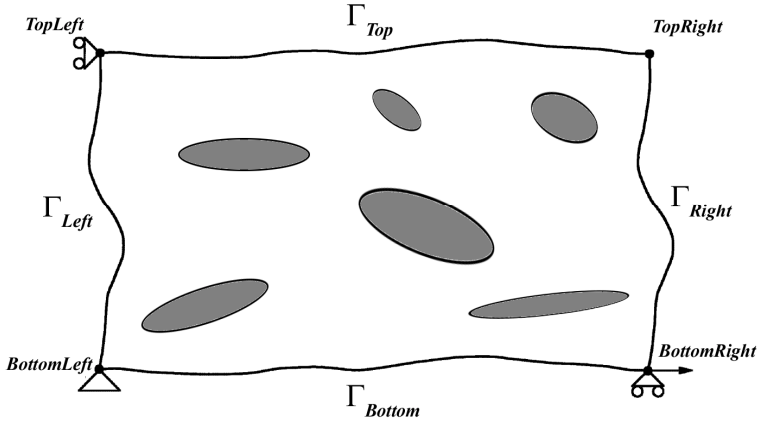

Figure 4.16: Schematic of the deformation behavior of a model with periodic boundary conditions [33]

Presence of a homogeneous composite medium in the model makes it easier, and computationally efficient, to apply these multi-point constraints as (a) number of nodes along opposing surfaces are the same and (b) there are fewer number of surface nodes

because of the coarser mesh at the surface resulting in a reduced number of constraints. Figure 4.17 shows the FE model created using Abaqus. Periodic boundary conditions are not shown in the figure for clarity. Uniaxial loading along the longitudinal direction was simulated by applying the following boundary conditions:

$$\boldsymbol{u}_{BottomLeft} = 0; u_{1_{TopLeft}} = 0; u_{2_{BottomRight}} = 0; u_{1_{BottomRight}} = u_{1_{applied}} \qquad (12)$$

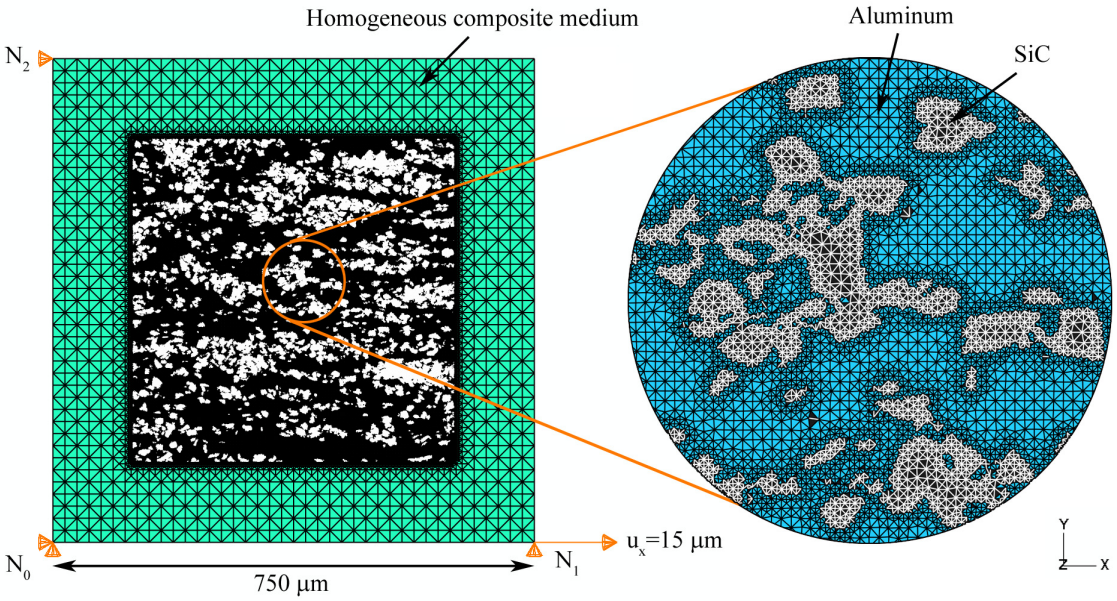

Figure 4.17: Finite element model for 2D uniaxial loading simulation

All the elements in the model were assigned plane-stress formulation with linear interpolation (CPS3 type). Small-displacement small-strain analysis was performed for 2% strain using Abaqus/Standard. The SiC particles were assumed to be perfectly elastic with Young's modulus E = 410 GPa and Poisson's ratio ν = 0.14. The aluminum matrix was assigned the constitutive properties deduced from microindentation, as discussed in Chapter 3 ($E = 70\ GPa$, $\nu = 0.33$, σ_y = 71 MPa, $n = 0.185$). The interface between the matrix and the reinforcement particles was assumed to be perfect. A stress-strain curve

was initially assumed for the homogeneous composite medium and was iteratively modified until the computed stress-strain curve from the model was identical to that from the previous iteration. For uniaxial loading simulation under the prescribed boundary conditions, the macroscopic stress-strain curve of the model can be computed from the *reaction force* and *displacement* output at the *BottomRight* node (N_1 in Figure 4.17) where the displacement was applied. The stress and strain values are given by:

$$\bar{\sigma}_1 = \left(\frac{1}{A}\right) RF_1; \quad \bar{\varepsilon}_1 = \left(\frac{1}{d}\right) \boldsymbol{u}_1 \tag{13}$$

where A is the area of the surface on which the non-zero displacement is imposed, RF_1 is the reaction force component in the x direction, d is the length of the model along the loading direction, and u_1, the displacement at node N_1. For a 2D plane stress analysis with thickness 1, A reduces to the edge length along the direction normal to the applied displacement, which in this case is the same as d. Note that for small-strain analysis in Abaqus, all stress and strain measures (for example, true stress versus nominal stress, and logarithmic strain versus engineering strain) are considered to be indistinguishable. This approximation was found not to introduce any significant error in the current research where the maximum applied strain was 2%. Contour plots of maximum principal stress (SMAX) and equivalent plastic strain (PEEQ) distributions within a small region in the model are given in Figures 4.18a and 4.18b respectively. It may be observed from Figure 4.18a that the SiC particles are the primary load-bearing phase and the stress concentration within the particles is highest when there are particle clusters. Consequently, such particle rich clusters have a higher propensity for crack nucleation and propagation. Similarly, matrix yielding is also high near particle clusters, as may be seen from Figure 4.18b. Contour plot of PEEQ distribution in the aluminum matrix for

the whole model is given in Figure 4.19 which clearly shows the shear banding in the matrix. Figure 4.20 gives the computed stress-strain curve for the composite along with the input constitutive properties used for the matrix and the reinforcement.

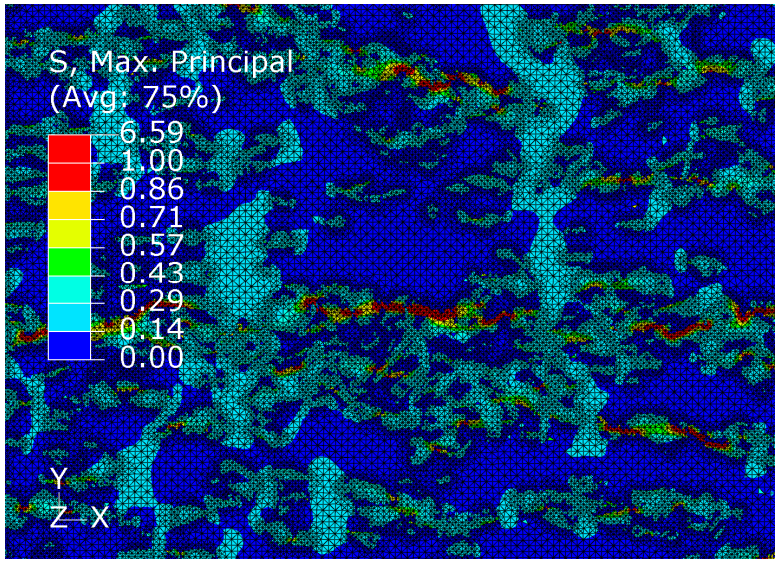

(a)

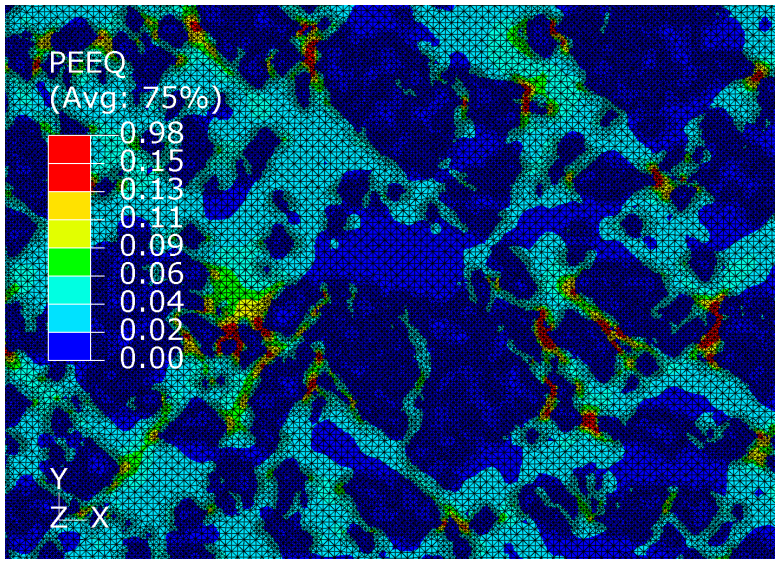

(b)

Figure 4.18: Contour plot of (a) maximum principal stress (GPa) distribution and (b) equivalent plastic strain distribution in a small section of the model

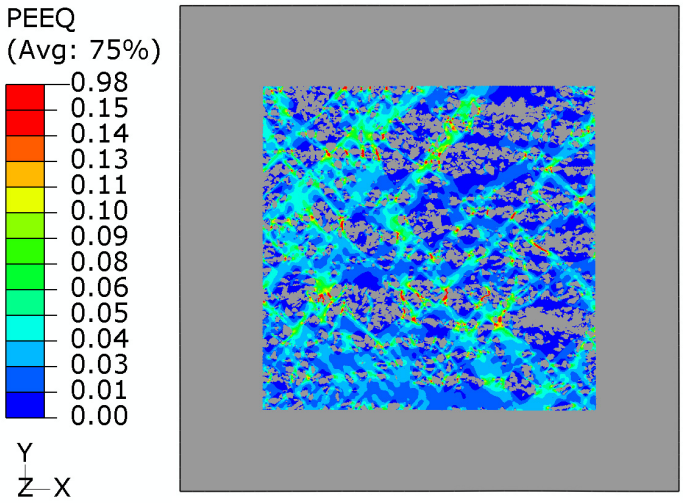

Figure 4.19: Contour plot of PEEQ distribution in the aluminum matrix for the whole model

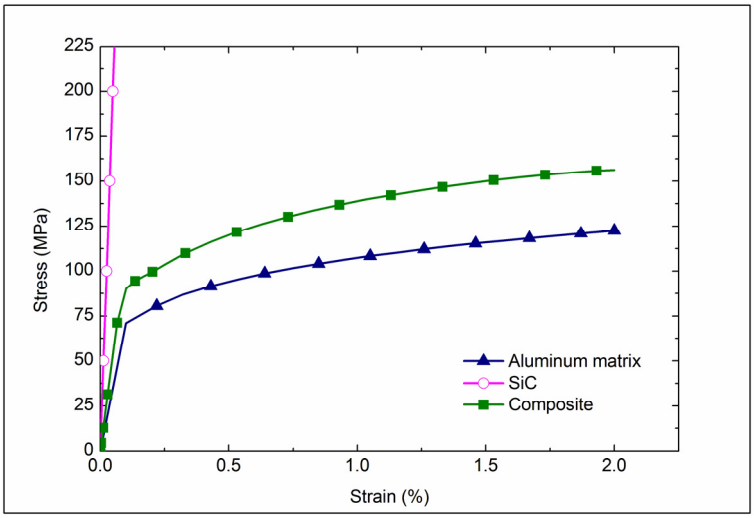

Figure 4.20: Computed stress-strain curve for the composite along with the input constitutive properties used for the matrix and the reinforcement

4.4.3 Mesh Convergence

When meshing real microstructures, the need to conform the finite element mesh as accurately as possible to the underlying microstructure implicitly requires that the

mesh is well refined. Mesh convergence and the effect of linear vs. quadratic interpolation of elements were studied using the model described in the previous sub-section, which is a 500 μm x 500 μm 8.1 PSR microstructure embedded in homogeneous composite medium of width 125 μm along all the four edges of the microstructure (referred to as Model A). The same microstructure was used to create a much more refined mesh in OOF which was then analyzed in Abaqus under the same boundary conditions (Model B). Figures 4.21a and 4.21b show a small cut-out from the two different models with Figure 4.21b clearly showing a refined mesh compared to Figure 4.21a. Similarly, effect of linear vs. quadratic interpolation of the elements was studied by assigning quadratic interpolation (Model C) to elements in model A. Details of the three models are given in Table 4.1.

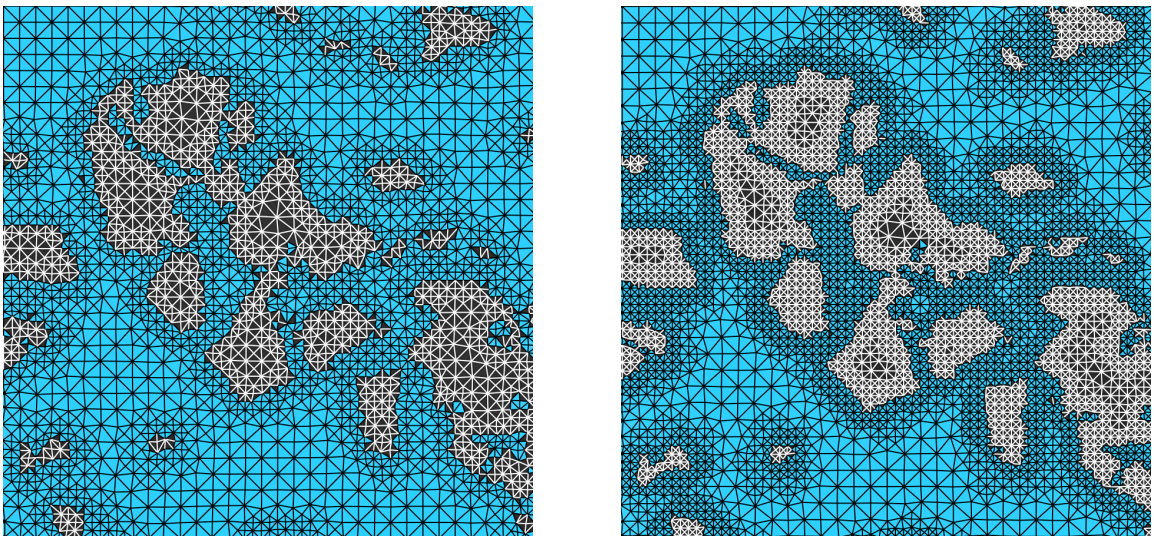

Figure 4.21: Small section of FE model with (a) regular mesh and (b) finer mesh size

Table 4.1: Mesh details for the convergence study models

Model	Element Type	Element Interpolation	Number of elements	Degrees of freedom
A	Plane Stress (CPS3)	Linear	254990	255152
B			502540	502702
C	Plane Stress (CPS6)	Quadratic	254990	1020282

Figure 4.22 shows the computed stress-strain curves from the three models. Rather than looking at the stress/strain contour plots, it is of interest to quantify the local stress/strain distributions in the models to make such observations more meaningful and comparable. Figure 4.23 shows the complementary cumulative distribution of the maximum principal stress within the SiC particles in the models, where Y-axis is the fraction of the SiC integration points with maximum principal stress higher than a given value. Similarly, Figure 4.24 gives the complementary cumulative distribution of equivalent plastic strain in the matrix. Tail ends of the distributions in Figures 4.23 and 4.24 are given in the inset of the respective figures. As may be seen from the figures, no significant variation is observed between the three models. Accordingly, linear interpolation elements with the same mesh density as model A was used in all further studies of DRA composites. Though not shown here, it was observed that increasing the width of the homogeneous medium beyond 125 μm did not affect the simulation results except for increasing the number of iterations required for the convergence of mechanical response.

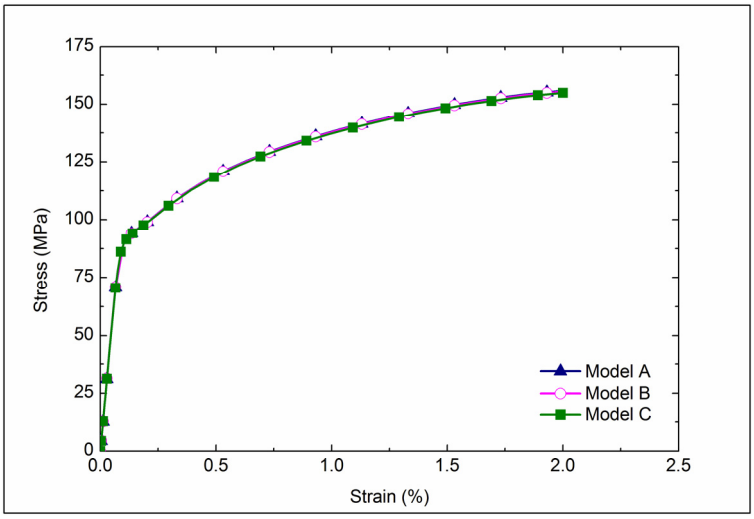

Figure 4.22: Computed stress-strain curves for mesh convergence study models

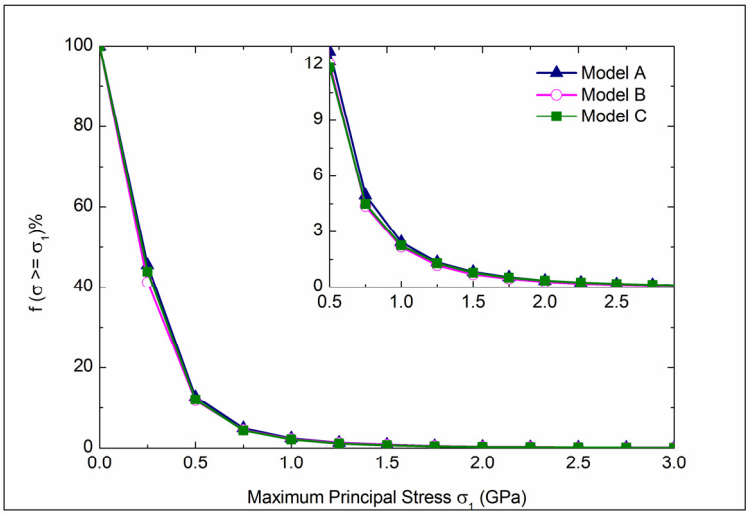

Figure 4.23: Complementary cumulative distribution of maximum principal stress in SiC for mesh convergence study models

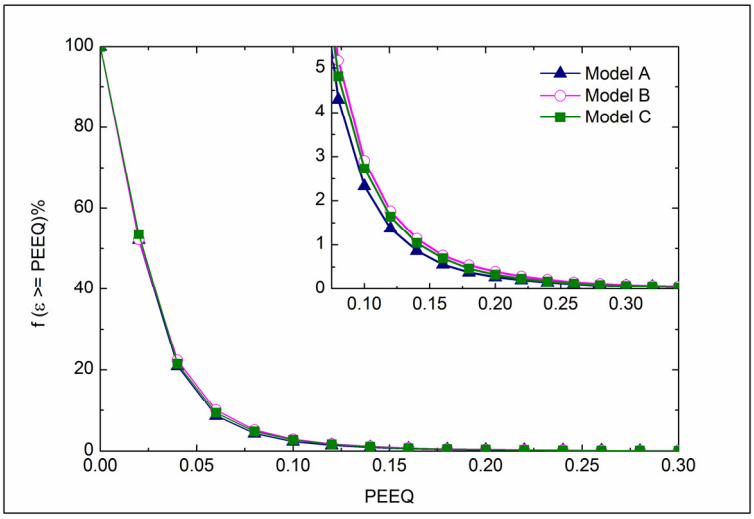

Figure 4.24: Complementary cumulative distribution of equivalent plastic strain in aluminum matrix for mesh convergence study models

4.4.4 Representative Volume Element

4.4.4.1 Window Size

As shown in the earlier section on two-point correlation functions, for a highly anisotropic and non-uniform microstructure such as the 8.1 PSR DRA composite, a randomly selected microstructural window of area 500 μm x 500 μm can be considered as statistically similar to the global microstructure but for long-range spatial correlations beyond 200 μm. The size of a representative volume element depends also on the material properties that one is trying to model, which in the present context is mechanical response under small strain. It is of interest to investigate whether or not the variations in long-range correlation functions affect the mechanical response of the microstructure in this case. Finite element analyses of the mechanical response for 2% strain along the longitudinal direction was performed on four randomly selected fields of view of sizes 1 mm x 1mm, 500 μm x 500 μm, 400 μm x 400 μm, and 300 μm x 300 μm of the 8.1 PSR

microstructure. Table 4.2 gives the volume fractions of SiC, computed elastic modulus, and computed 0.2% yield strength values for the four models. Elastic modulus and yield strength values have been rounded off to the nearest integer. Figure 4.25 gives the computed stress-strain curves for the four different window sizes. Similarly, 4.26 and 4.27 show the computed stress-strain curves, maximum principal stress distribution in SiC phase, and the distribution of equivalent plastic strain in the matrix for the four models.

Table 4.2: Volume fractions of SiC particles and computed mechanical properties for four different 8.1 PSR window sizes

Image Size	**V_f (SiC) %**	**Elastic Modulus (GPa)**	**Yield Strength (MPa)**
1 mm x 1 mm	28.04	111	100
500 μm x 500 μm	28.24	111	100
400 μm x 400 μm	29.36	113	102
300 μm x 300 μm	21.44	100	93

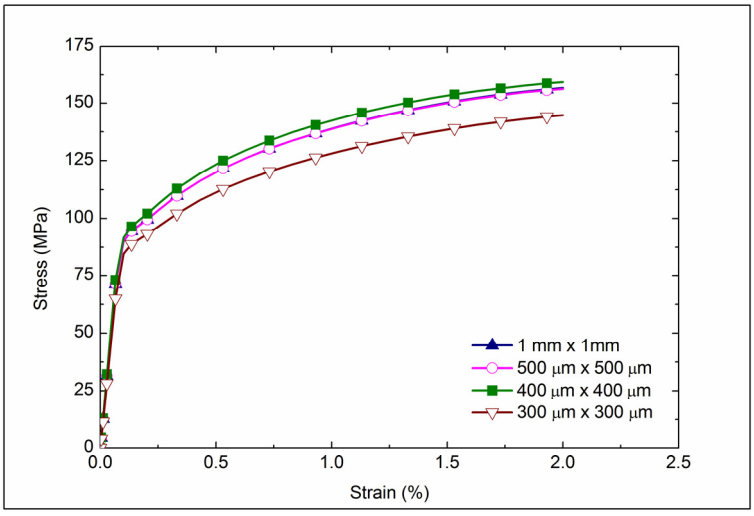

Figure 4.25: Computed stress-strain curves for four different 8.1 PSR window sizes

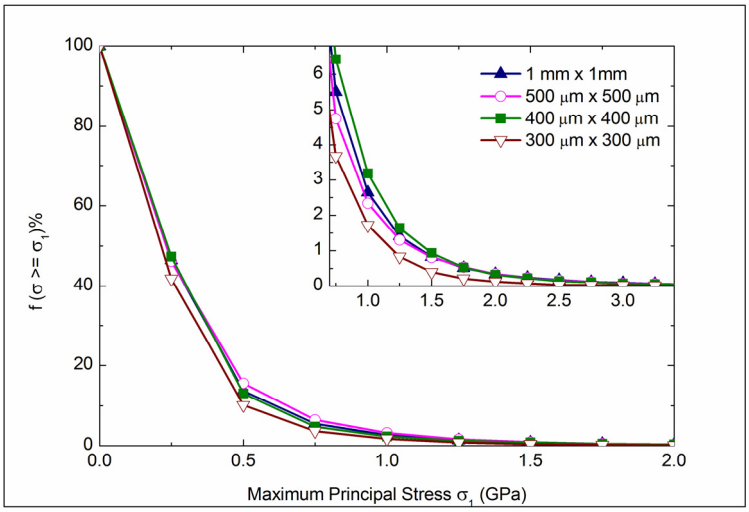

Figure 4.26: Complementary cumulative distribution of maximum principal stress in SiC for four different 8.1 PSR window sizes

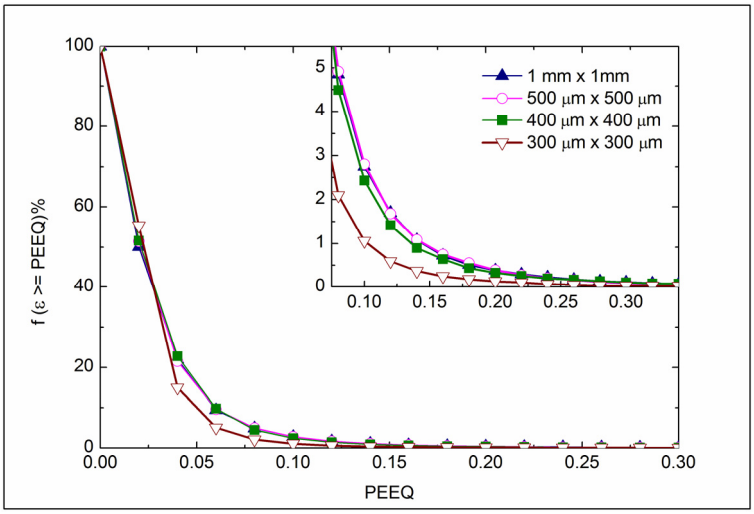

Figure 4.27: Complementary cumulative distribution of equivalent plastic strain in aluminum matrix for four different 8.1 PSR window sizes

The variation in the volume fraction and/or spatial distribution of SiC particles among the four different models are clearly reflected in the computed properties. A microstructural window of edge length 300 μm does not capture the spatial heterogeneity of the 8.1 PSR microstructure and a randomly selected image can underestimate/overestimate the

volume fraction by as much as 25% depending on whether it falls on the cluster-free or cluster-rich region. It may be recalled that the two-point correlation function for 8.1 PSR microstructure along the longitudinal direction approaches unity at around 250 μm, suggesting that it is the characteristic length scale of the microstructure along that direction. But to assume that a microstructural square window of edge length 250 μm is an RVE is not necessarily true, as observed from the FE analysis of a 300 μm x 300 μm window. Note that the two-point correlation functions given in Figure 4.8 were averaged over a large montage image. For any randomly picked microstructural window to be representative of the global microstructure, the window size must be much larger than the characteristic length scale. Microstructural window size of 500 μm x 500 μm was chosen in this study for further analyses. Five different realizations of this size were input in finite element models to look at the micromechanical response. Table 4.3 gives the volume fractions of SiC, computed elastic modulus, and computed 0.2% yield strength values for the five realizations.

Table 4.3: Volume fractions of SiC particles and computed mechanical properties for five different realizations of 500 μm x 500 μm window of 8.1 PSR microstructure

Model	**V_f(SiC) %**	**Elastic Modulus (GPa)**	**Yield Strength (MPa)**
i	26.86	110	99
ii	28.17	111	100
iii	28.24	111	100
iv	28.20	111	100
v	28.23	111	100

Figures 4.28, 4.29, and 4.30 show the corresponding computed stress-strain curves, maximum principal stress distribution in SiC phase, and the distribution of equivalent plastic strain in the matrix, respectively. The variations in the curves for the five realizations are well within the statistical variations that are expected in material microstructures.

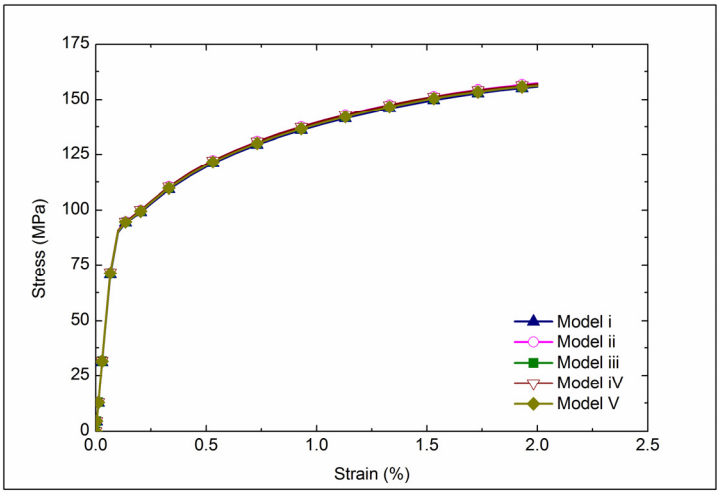

Figure 4.28: Computed stress-strain curves for five different 8.1 PSR 500 μm x 500 μm microstructural windows

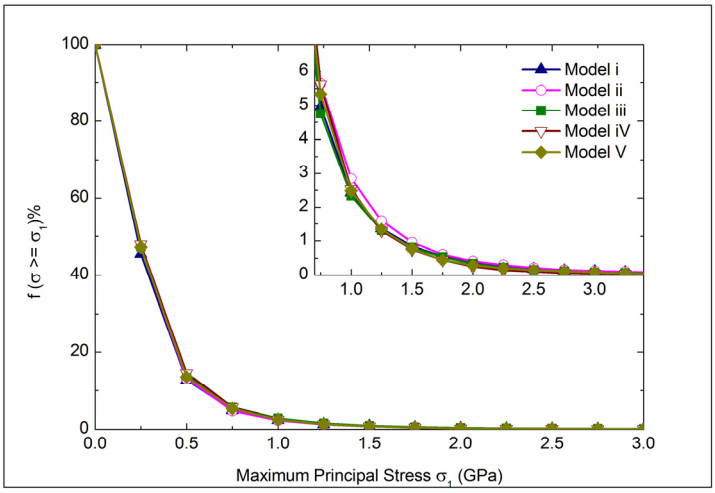

Figure 4.29: Complementary cumulative distribution of maximum principal stress in SiC for five different 8.1 PSR 500 μm x 500 μm microstructural windows

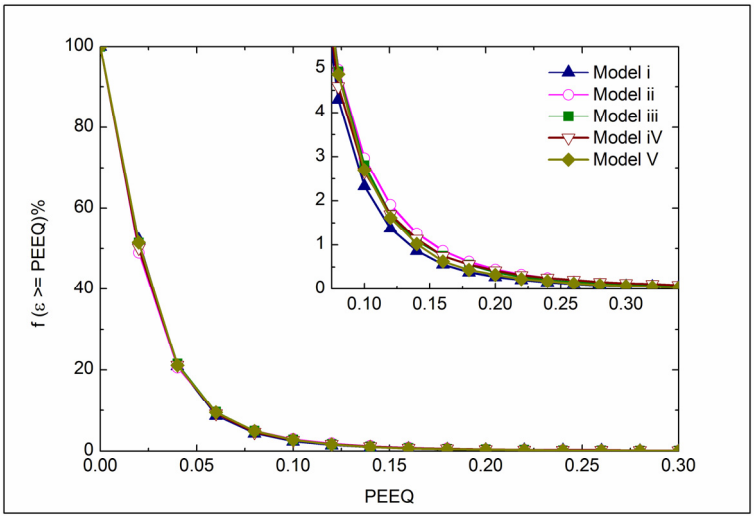

Figure 4.30: Complementary cumulative distribution of equivalent plastic strain in aluminum matrix for five different 8.1 PSR 500 μm x 500 μm microstructural windows

4.4.4.2 Boundary Conditions

The mechanical response of an RVE must remain identical regardless of the nature of boundary conditions (for example, periodic versus non-periodic and displacement versus traction boundary conditions). All the FE analyses described in the previous sections were displacement-controlled with periodic boundary conditions. Non-periodic displacement- and traction-controlled analyses were carried out to compare the micromechanical response. Figure 4.31 shows the model used for non-periodic boundary conditions. Displacements in both *x* and *y* directions were constrained to zero for the *Left* edge of the model and the displacement/traction boundary conditions were specified on the *Right* edge along the longitudinal direction. The micromechanical responses of these models were compared with that of the model with periodic boundary conditions. Figures 4.32, 4.33, and 4.34 show the computed stress-strain curves, maximum principal stress distribution in SiC phase, and the distribution of equivalent plastic strain in the matrix for

the three models respectively. It may be observed that the micromechanical response is not affected by the nature of boundary conditions.

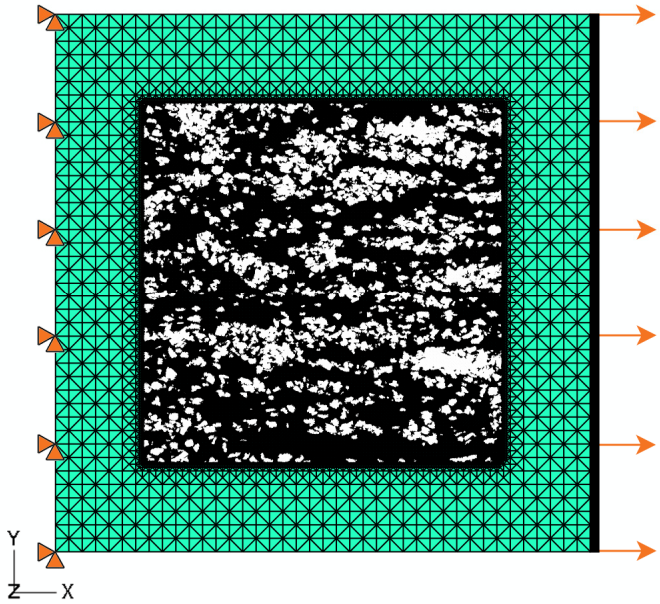

Figure 4.31: Finite element model with non-periodic boundary conditions

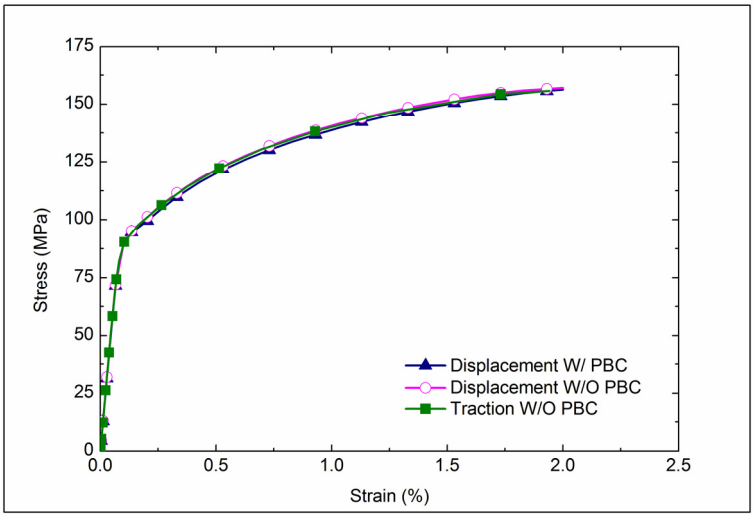

Figure 4.32: Computed stress-strain curves for different boundary conditions

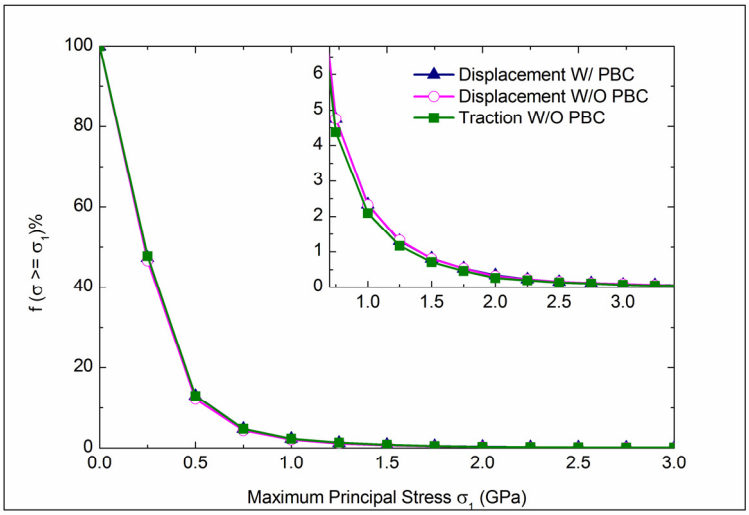

Figure 4.33: Complementary cumulative distribution of maximum principal stress in SiC and for different boundary conditions

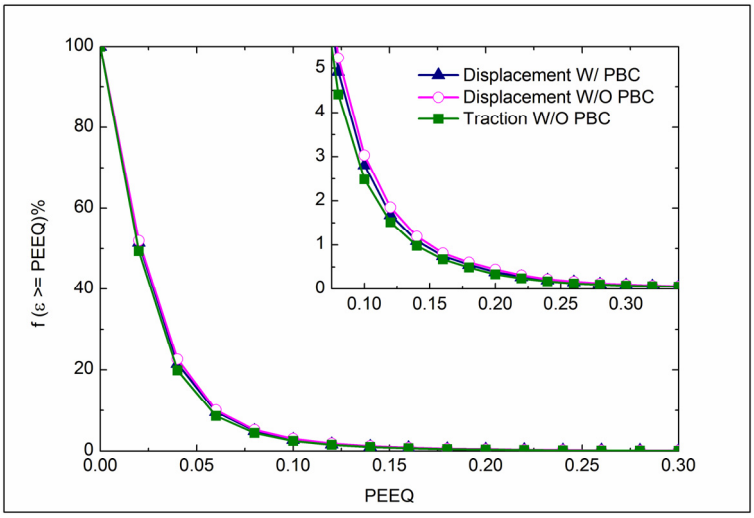

Figure 4.34: Complementary cumulative distribution of equivalent plastic strain in aluminum matrix for different boundary conditions

Results given in the previous sections conclusively show that a 500 μm x 500 μm microstructural window is at least as big as a representative volume element of this microstructure. It is concluded that for an anisotropic microstructure, any randomly chosen square microstructural window with an edge length of at least twice as much as

the characteristic length scale of the microstructure can be considered an RVE provided the volume fraction of the phase of interest in the chosen window is representative of the global volume fraction. Since the 8.1 PSR DRA microstructure is the most anisotropic and spatially non-uniform material considered in this research, a microstructural window size that is representative for this structure will be representative for any other microstructures under investigation. Hence a 500 μm edge length microstructural window was chosen for FE analyses of all other microstructures.

4.4.5 Finite Element Analysis of 2.0 PSR Microstructure

Displacement-controlled uniaxial loading simulation with periodic boundary conditions along the extrusion direction was performed on a 2.0 PSR microstructure montage image of 500 μm x 500 μm area and the micromechanical response was compared with that of 8.1 PSR microstructure. Figures 4.35, 4.36, and 4.37 show the computed stress-strain curves, maximum principal stress distribution in SiC phase, and the distribution of equivalent plastic strain in the matrix for the two different microstructures. Figure 4.38 gives the contour plots of maximum principal stress in the two models. The computed macroscopic stress-strain curves are identical for both the microstructures. While subtle differences are observed in the local stress/strain distributions (for example, the maximum principal stress values are higher in the 8.1 PSR microstructure because of the SiC clusters), the differences are not as substantial as one might expect from these microstructures. But it may be noted from the contour plots in Figure 4.38 that the connectivity of high-stressed regions is more in the 8.1 PSR microstructure. Though not considered in this research, such connectivity is expected to be a factor when modeling crack nucleation and propagation.

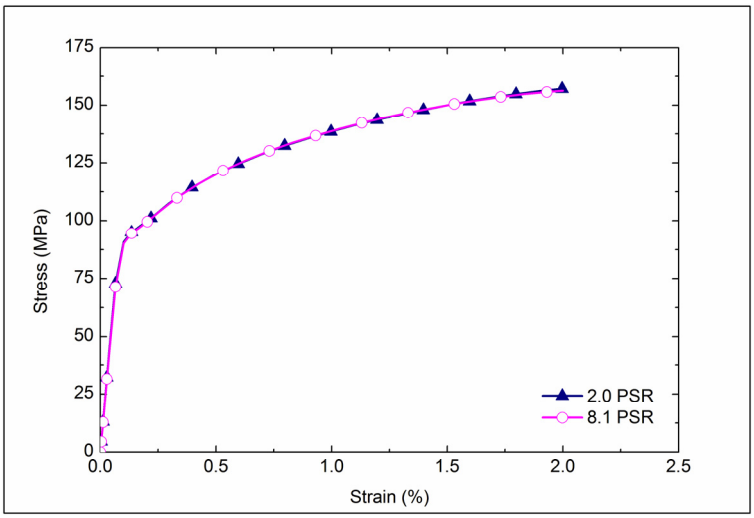

Figure 4.35: Computed stress-strain curves for 2.0 PSR and 8.1 PSR DRA microstructures for loading along extrusion direction

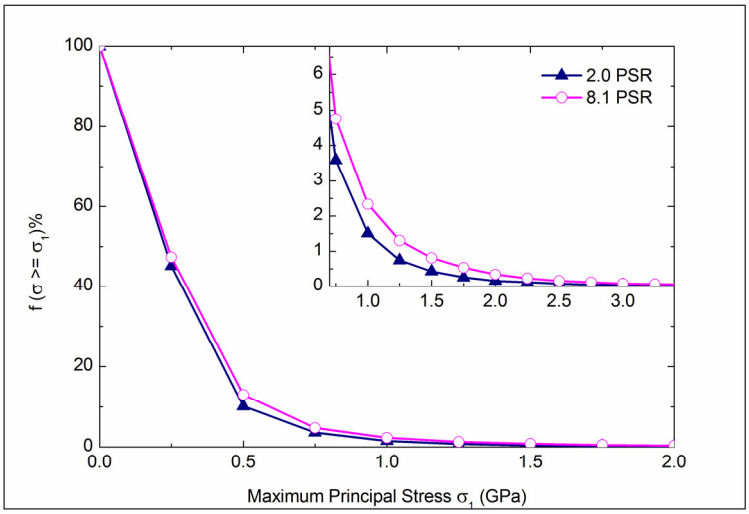

Figure 4.36: Complimentary cumulative maximum principal stress distribution in SiC for 2.0 and 8.1 PSR microstructures

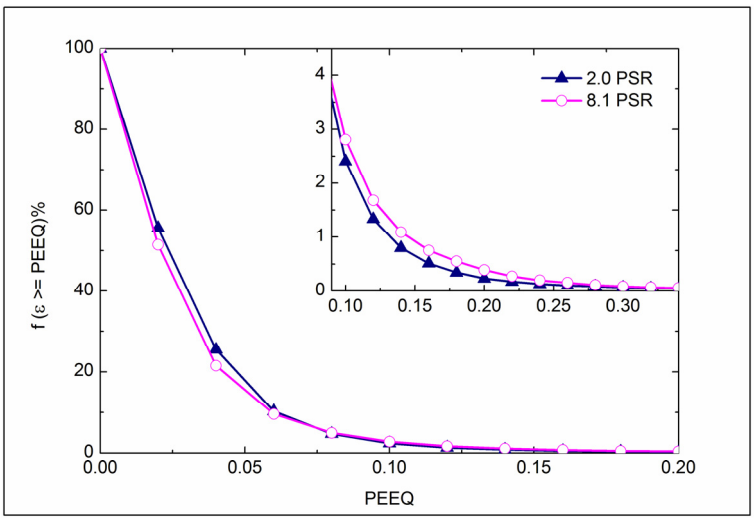

Figure 4.37: Complimentary cumulative equivalent plastic strain distribution in the matrix for 2.0 and 8.1 PSR microstructures

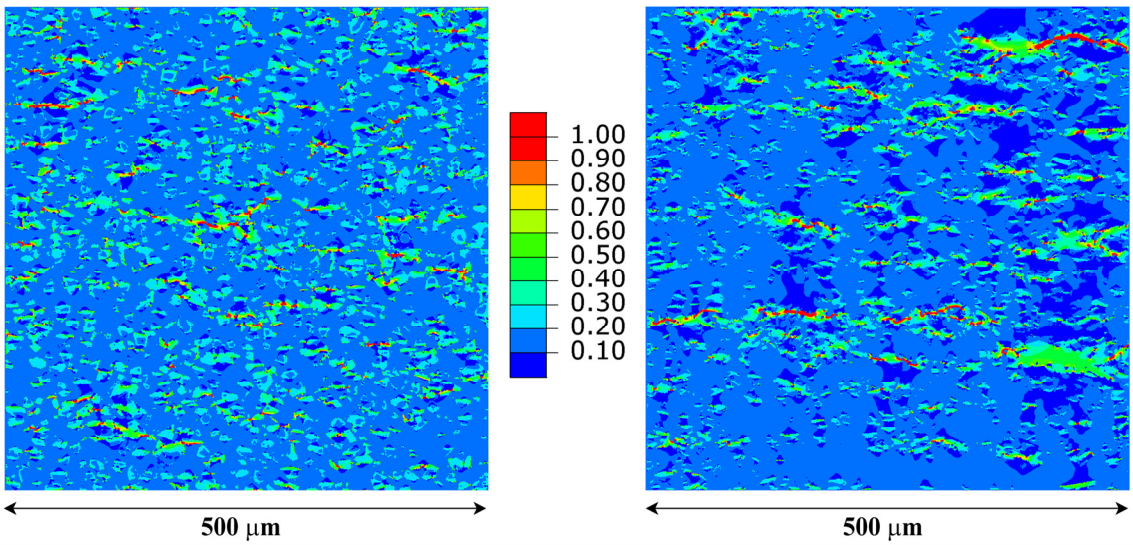

(a) (b)

Figure 4.38: Maximum principal stress (GPa) contour plots for (a) 2.0 PSR microstructure and (b) 8.1 PSR microstructure

4.4.6 Transverse Loading

Because of the anisotropy introduced by the extrusion process, the DRA composites are expected to behave differently under different loading directions. All the previous analyses discussed in this chapter were for uniaxial loading along the extrusion direction. Transverse loading simulations were performed on the 2.0 PSR and 8.1 PSR DRA microstructures using 500 μm edge length microstructural windows. Table 4.4 gives the comparison of the computed elastic modulus and 0.2% yield strength values with that for longitudinal loading. Figures 4.39, 4.40, and 4.41 show the corresponding computed stress-strain curves, maximum principal stress distribution in SiC phase, and the distribution of equivalent plastic strain in the matrix. It may be observed that the 2D models very well capture the anisotropy in both the microstructures. For both 2.0 and 8.1 PSR microstructures, the material is substantially weaker in a direction perpendicular to the extrusion direction. But the microstructural differences between 2.0 and 8.1 PSR microstructures, primarily the clustering of SiC particles, are clearly not captured in the 2D micromechanical response.

Table 4.4: Computed elastic modulus and yield strength values for longitudinal and transverse loading of 2.0 PSR and 8.1 PSR microstructures

PSR	Loading Direction	Elastic Modulus (GPa)	Yield Strength (MPa)
2.0	Longitudinal	114	101
	Transverse	107	95
8.1	Longitudinal	111	100
	Transverse	103	94

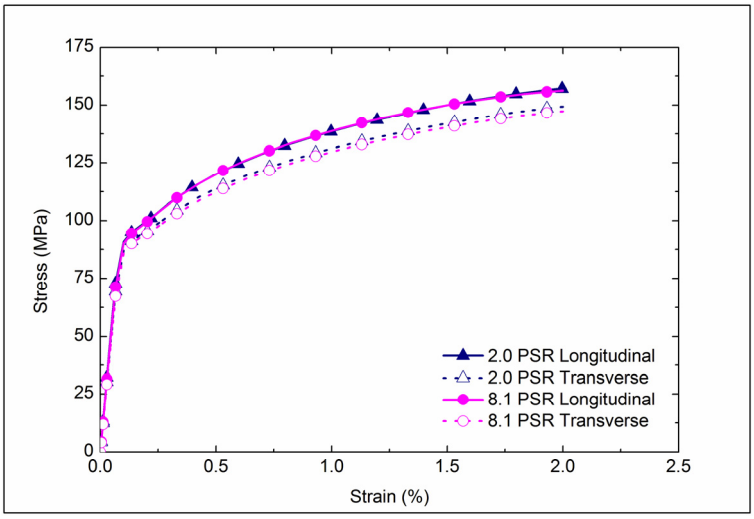

Figure 4.39: Computed stress-strain curves for longitudinal and transverse loading

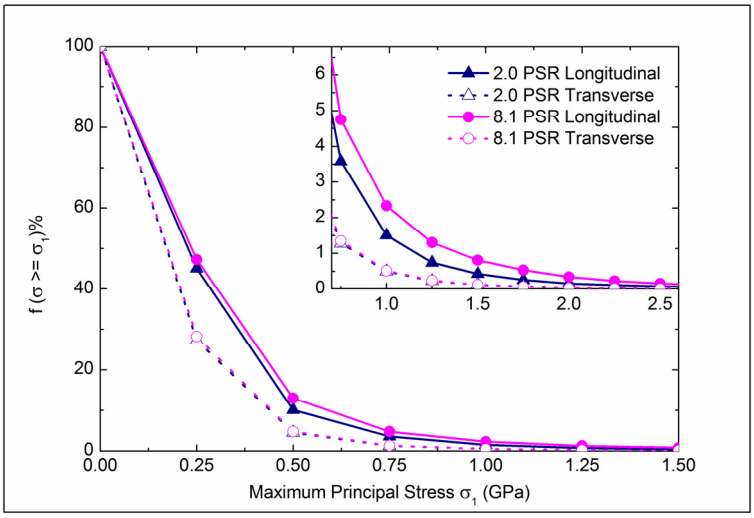

Figure 4.40: Complimentary cumulative maximum principal stress distribution in SiC for longitudinal and transverse loading of DRA microstructures

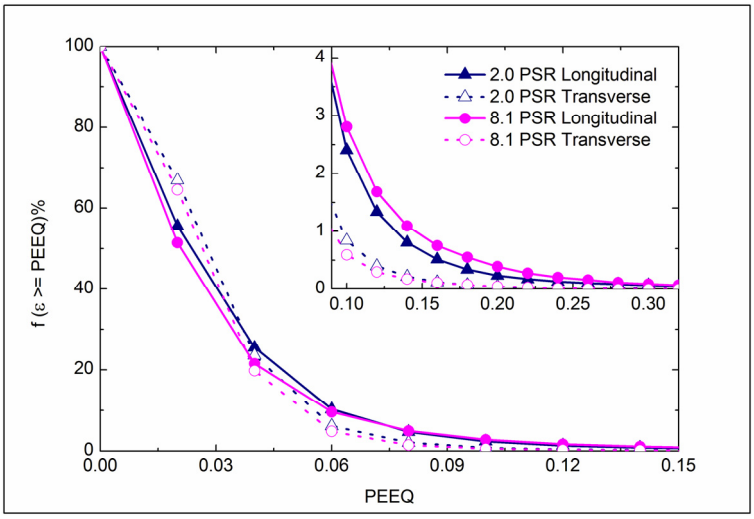

Figure 4.41: Complimentary cumulative equivalent plastic strain distribution in the matrix for longitudinal and transverse loading of DRA microstructures

4.4.7 Comparison with Experimental Data

Room temperature tensile tests were carried out on extruded samples of 2.0, 3.1, and 8.1 PSR DRA composites along the extrusion direction by Dr. Spowart at Air Force Research Laboratory. Test results for three samples each of 2.0, 3.1, and 8.1 PSR composites are shown in Figure 4.42. While some variability is observed in the stress-strain behavior of all the three materials, it is apparent that higher PSR values lead to lower yield strength and ductility. In order to investigate whether or not the 2D plane-stress simulations reflect these differences, computed stress-strain curves of 2.0 and 8.1 PSR composites were compared with the experimental data.

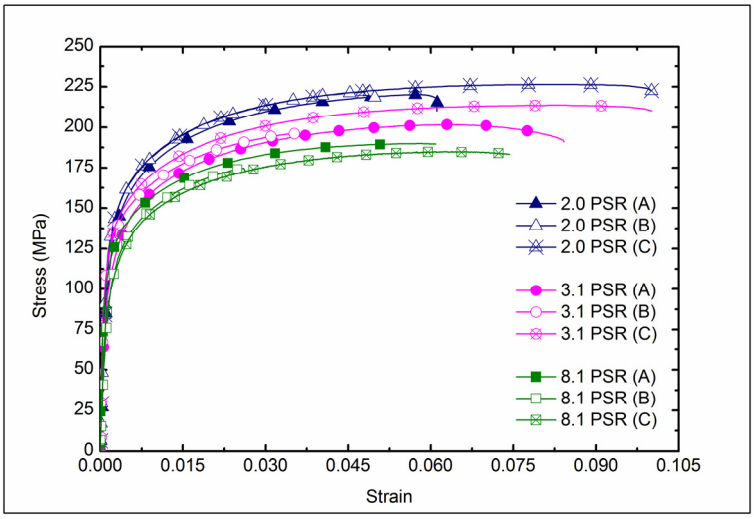

Figure 4.42: Tensile test data of DRA composites containing 28% SiC [126]

Figure 4.43 shows typical experimental stress-strain curves for 2.0 and 8.1 PSR composites along with the computed curves from 2D plane-stress simulations. It may be noted that while the elastic modulus and strain-hardening coefficient values predicted by 2D simulations of DRA composites are in good agreement with the experimental data, the simulations noticeably underestimate the yield strength of these materials. Also, while the experimental curves clearly show a difference between the mechanical response of 2.0 and 8.1 PSR microstructures, the computed curves from 2D FE analysis for the two microstructures are identical. These discrepancies may be attributed to (a) the inability of a 2D analysis to account for the complex stress state in a 3D microstructure and/or (b) the presence of porosity which was not accounted for in the FE analyses performed in this research. This is particularly true for the 8.1 PSR microstructure where the SiC particle rich clusters are often accompanied by porosity as can be seen in Figure 4.44 which shows a close-up view of one SiC cluster region. Note that the two-way segmentation of

the grayscale image before FE meshing in this study resulted in treating the porosity as part of the matrix phase.

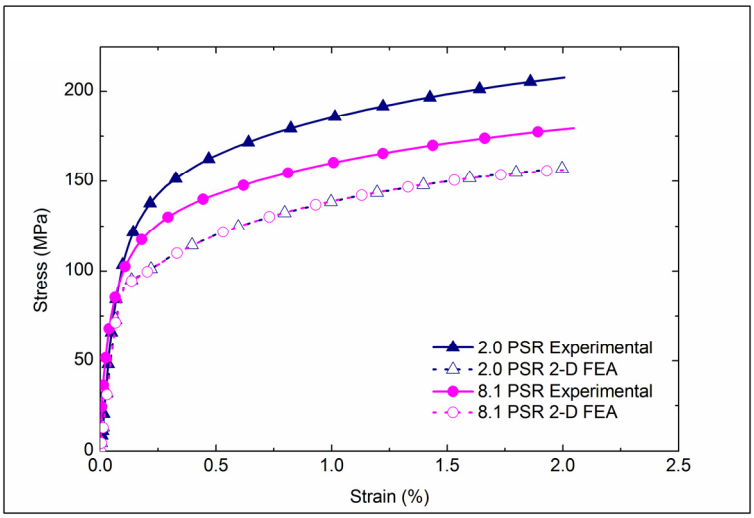

Figure 4.43: Experimental stress-strain curves for 2.0 and 8.1 PSR microstructures along with the computed curves from 2D plane-stress simulations

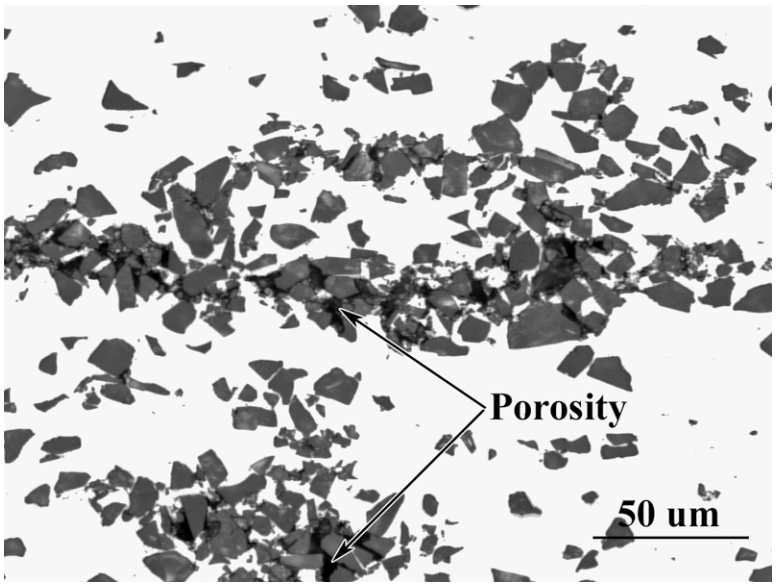

Figure 4.44: SiC cluster region in 8.1 PSR microstructures showing porosity

Density measurements of the DRA composites conducted recently at Air Force Research Laboratory are given in Figure 4.45. While the 2.0 PSR microstructure is 99% dense, the 8.1 PSR microstructure is only 94.3 % dense suggesting a large amount of porosity in the material. These issues will be addressed in the next chapter which deals with the 3D modeling.

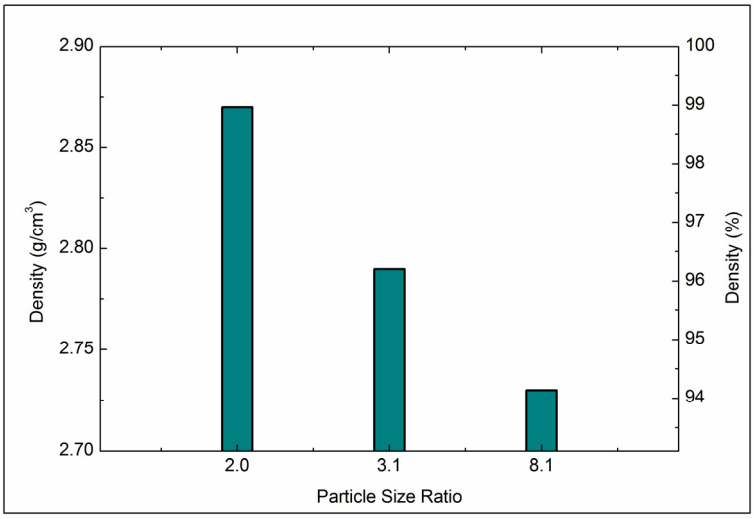

Figure 4.45: Density measurements on DRA composites [126]

4.4.7 Finite Element Analysis of Ti-6Al-4V-1B Microstructure

Uniaxial loading simulations were carried out on 500 μm x 500 μm montage images of Ti-6Al-4V-1B alloy microstructure along longitudinal and transverse directions. Mesh convergence studies were conducted as explained earlier for DRA composites and a mesh size of the order of 0.5 μm at the Ti/TiB interface was found to be sufficient for the analyses. Figure 4.46 shows a small section of the FE model. Periodic boundary conditions with homogeneous composite medium were used for the studies, details of which are given in an earlier section on modeling of DRA composites.

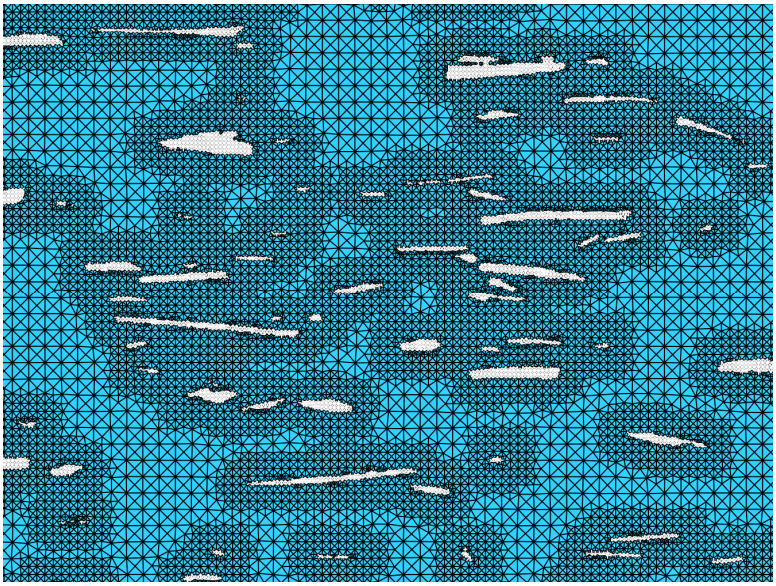

Figure 4.46: Small section of the FE model for Ti-6Al-4V-1B alloy

The TiB particles were assumed to be perfectly elastic with Young's modulus E = 466 GPa and Poisson's ratio ν = 0.15. The Ti-6Al-4V matrix was assigned the constitutive properties deduced from microindentation, as discussed in Chapter 3 ($E = 115\ GPa$, $\nu = 0.33$, σ_y = 1025 MPa, $n = 0.1$). The interface between the matrix and the whiskers was assumed to be perfect. The microstructure was embedded in a homogeneous composite medium of which the constitutive properties were computed in an iterative manner as described earlier for the DRA microstructures. Figures 4.47a and 4.47b show the maximum principal stress contour plots of the model under longitudinal and transverse loading respectively. Note that the homogeneous composite medium and the stress contour plots in Ti-6Al-4V matrix are not shown for clarity. The complementary cumulative distribution plots of maximum principal stress in the TiB whiskers and equivalent plastic strain in Ti-6Al-4V matrix are given in Figures 4.48 and 4.49 respectively. Figures 4.47 and 4.48 evidently show that the TiB whiskers are more

effective as the load-bearing phase when aligned parallel to the loading direction. The computed stress-strain curve for longitudinal loading along with the experimental stress-strain curve is shown in Figure 4.50.

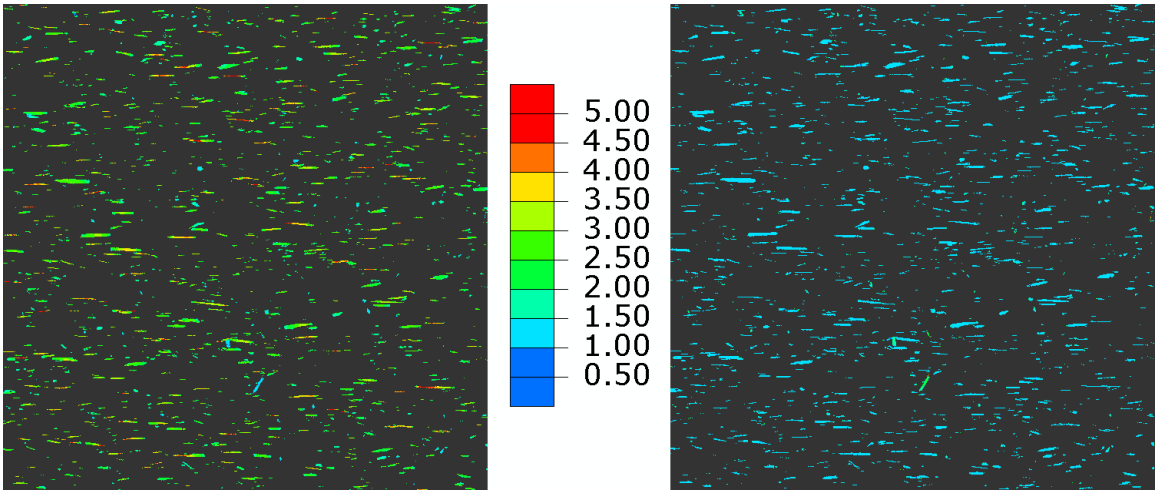

(a) (b)

Figure 4.47: Maximum principal stress (GPa) contour plots for (a) longitudinal loading and (b) transverse loading

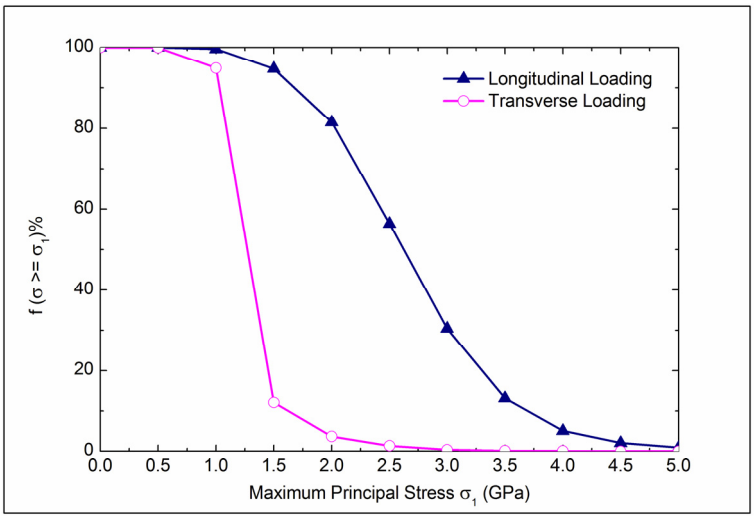

Figure 4.48: Complimentary cumulative distribution of maximum principal stress in TiB whiskers for longitudinal and transverse loading

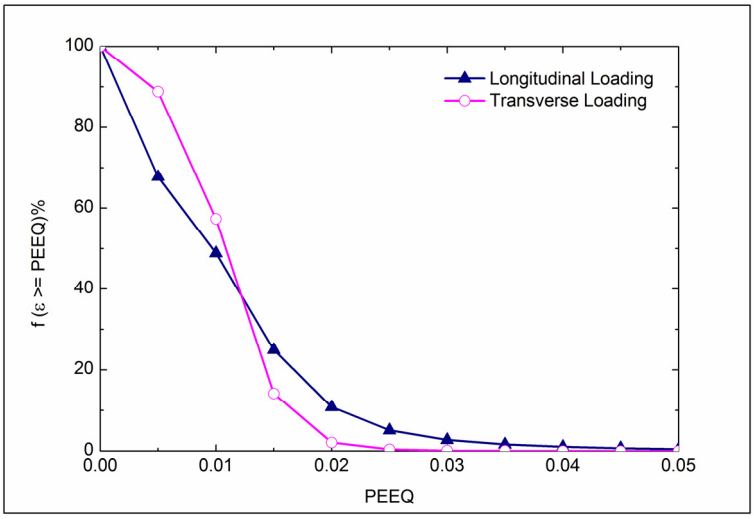

Figure 4.49: Complimentary cumulative distribution of equivalent plastic strain in the matrix for longitudinal and transverse loading

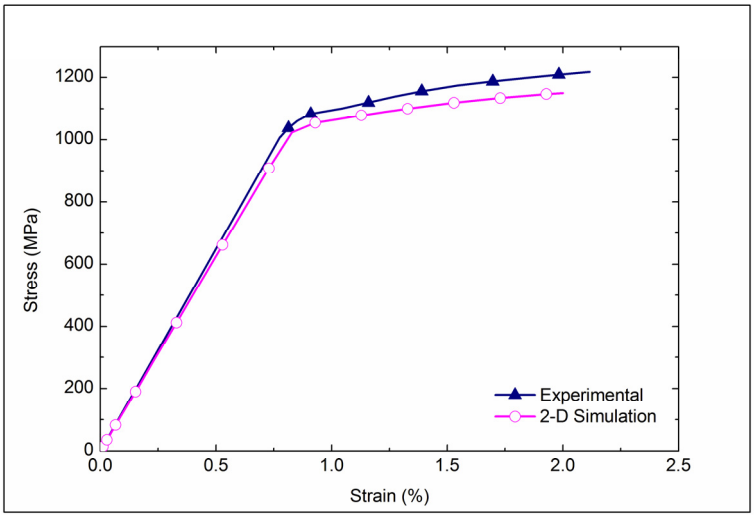

Figure 4.50: Experimental and computed stress-strain curves for uniaxial loading of Ti-6Al-4V-1B alloy along the extrusion direction

4.5 Summary

Two-dimensional plane-stress micromechanical analyses were performed on DRA composites with varying spatial distribution of SiC particles and boron modified Ti-6Al-4V alloy containing *in situ* formed TiB whiskers. Two-point correlation functions

were used to arrive at a statistically representative volume element for the microstructures. It was observed that while the 2D FE simulations were sensitive to the anisotropy of the microstructures as well as first order microstructural properties such as volume fraction of the reinforcement phase, the spatial arrangement of the reinforcement phase did not significantly affect the computed macroscopic response. Comparison with experimental tensile test data showed that the 2D plane-stress analyses underestimate the yield stress of the composite material in all cases. This may be attributed to the limitations associated with the 2D simplification of a 3D microstructure. Experimental studies have shown a significant difference in the uniaxial stress-strain behavior of 2.0 and 8.1 PSR microstructures. The 2D analyses suggest that the differences are due primarily to the porosity introduced by the clustering of SiC particles rather than the clustering itself. These observations will be revisited in the next chapter within the context of 3D modeling. It is concluded that for discontinuously reinforced composites, while qualitative observations may be made using 2D plane-stress simulations, the usefulness of such simulations for quantitative information is limited.

CHAPTER 5

THREE-DIMENSIONAL MICROMECHANICAL SIMULATIONS

5.1 Introduction

Most material microstructures are three-dimensional in nature and two-dimensional models do not always accurately capture the deformation behavior of these materials. It was shown in the last chapter that for discontinuously reinforced composite materials, 2D plane stress analyses underestimate the mechanical response under uniaxial loading. Accordingly, meaningful simulations of such materials require incorporation of the 3D microstructures in the simulation models. 3D realistic micromechanical simulations reported in the literature are limited to isotropic uniform random microstructures. This is primarily due to (a) the unavailability of large 3D datasets that capture the long-range spatial arrangement in anisotropic non-uniform microstructures; and/or (b) computational difficulties involved in FE meshing and subsequent analyses of 3D microstructural volumes. In the current research, 3D volumes reconstructed using montage serial-sectioning technique were used to conduct micromechanical simulations of DRA composites and Ti-6Al-4V-1B alloy.

5.2 Reconstruction of Three-Dimensional Microstructures

Three-dimensional microstructures of opaque metallic materials can be reconstructed using different techniques such as serial-sectioning or X-ray tomography. In this work, 3D microstructures of DRA composites and Ti-6Al-4V-1B alloy reconstructed previously using montage serial-sectioning technique were used to investigate the micromechanical behavior of these materials. The 3D reconstruction of

DRA composites and boron modified titanium alloys were performed by Dr. Harpreet Singh [124] and Dr. Scott Lieberman [122] respectively, as part of their doctoral thesis research. Figures 5.1a and 5.1b show small sections of the reconstructed 3D volumes of DRA composites with PSR values of 2.0 and 8.1 respectively. In the figures, *X* is the extrusion direction; *Y* is the transverse direction; and, *Z*, the through-thickness direction.

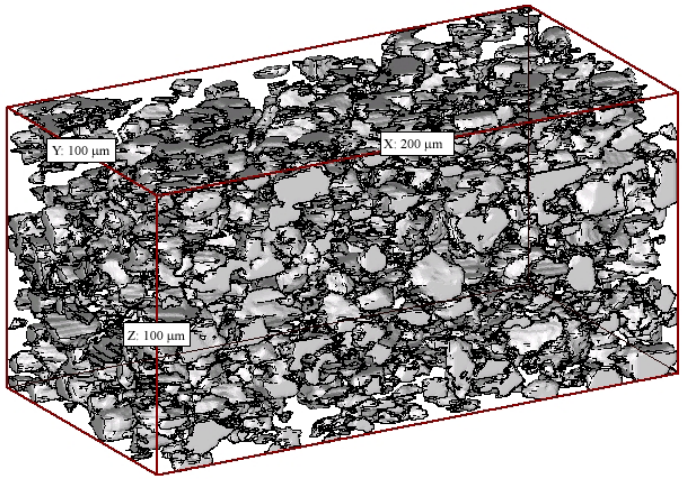

(a)

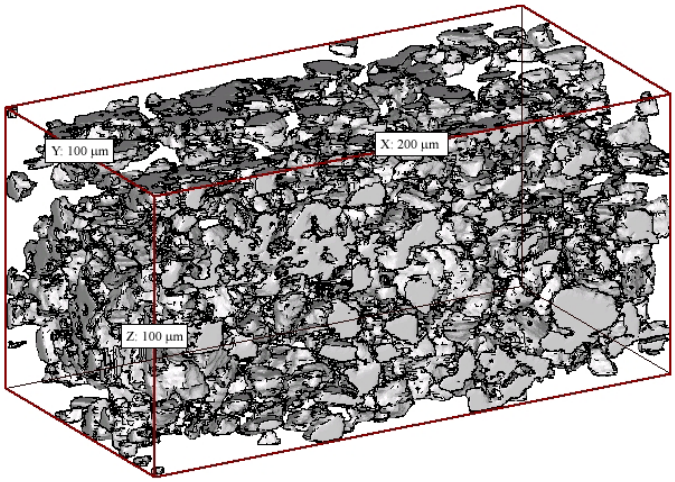

(b)

Figure 5.1: Reconstructed 3D volumes of DRA composites with PSR values of (a) 2.0 and (b) 8.1

Figure 5.2 shows a small section of the reconstructed microstructure of Ti-6Al-4V-1B alloy where *Z* is the extrusion direction (serial-sectioning was performed in a direction normal to the extrusion direction). Note that only the reinforcement phase (SiC or TiB) is shown in the figures.

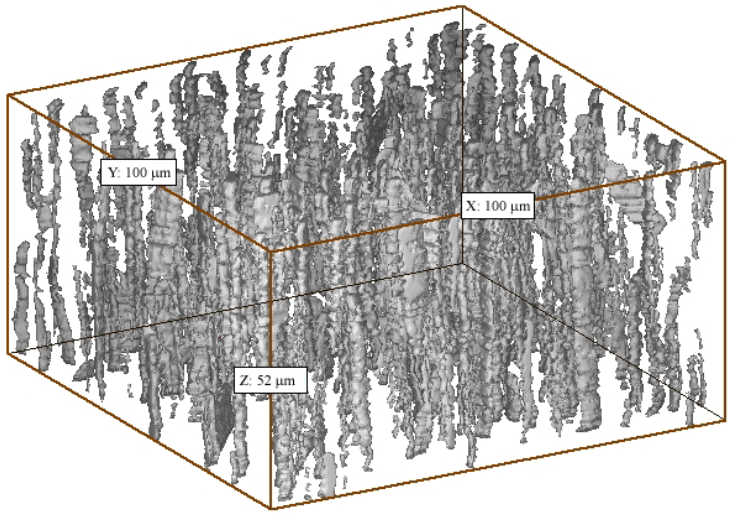

Figure 5.2: Reconstructed microstructure of Ti-6Al-4V-1B alloy

5.3 Three-Dimensional Microstructural RVE

A combination of two-point correlation functions and FE analyses were used in the previous chapter for identifying the RVE for 2D micromechanical studies of the DRA composites and Ti-6Al-4V-1B alloy. It was shown that the microstructural RVE size depends on the spatial distribution of the phases and the anisotropy of the microstructure along with the first order attributes such as volume fraction and size distribution of the reinforcement phases. For 2D simulations of DRA composites, the two-point correlation function measurements (and the subsequent FE analyses) were performed on metallographic sections along the *X*-*Y* plane which contains the extrusion axis. For the

8.1 PSR DRA composite, which has the most non-uniform microstructure among the materials under investigation in this research, it was shown that a microstructural window with an edge length of 500 μm along the extrusion direction can be considered an RVE for uniaxial loading simulations. Extending this information to 3D, it can be stated that a 3D cube of 500 μm edge length is representative of the 8.1 PSR microstructure. But the amount of 3D microstructural volume dataset available for simulations is limited by the effort required in reconstructing large volumes of the microstructure. In the present case, where serial-sectioning was used to obtain 100 layers of microstructure with 1 μm gap between the layers, we are limited to a length of 100 μm along the thickness direction. We are also limited by the computational power when dealing with large 3D microstructural simulations. Accordingly, it is of interest to investigate whether smaller microstructural volumes can serve as RVE for 3D simulations. It was shown in the previous chapter that the characteristic length scale along the transverse (*Y*) direction is much smaller than that along the extrusion (*X*) direction for all the microstructures under study, due to the anisotropy introduced by the extrusion process. Since the microstructures are statistically symmetric along the extrusion axis, the characteristic length scale of the microstructure is expected to be of the same order along all the directions normal to the extrusion direction (the *Y*-*Z* plane for DRA composites). It may be argued that the edge lengths along both *Y* and *Z* axes for the 3D RVE of these composites will be shorter than that required along the *X* axis. To verify this, two-point correlation functions were measured on sections normal to the extrusion direction prepared using standard metallographic procedures. Figures 5.3a and 5.3b show 1mm x 1mm montage images of 2.0 PSR and 8.1 PSR microstructures respectively. The

comparison of two-point correlation functions for the SiC phase (P_{11}) measured along *Y* ($\theta = 0$) and *Z* ($\theta = 90$) axes for the two images are given in Figure 5.4. As expected, the figures show that both the microstructures are isotropic in *Y*-*Z* plane with the 8.1 PSR microstructure being more non-uniform.

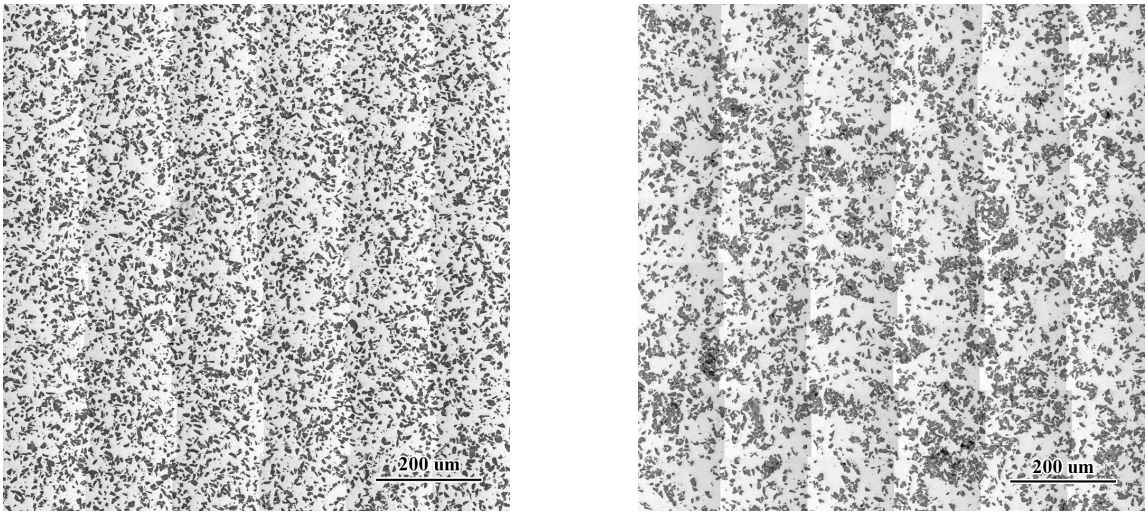

(a) (b)

Figure 5.3: Montage optical micrographs of transverse section of (a) 2.0 PSR microstructure and (b) 8.1 PSR microstructure

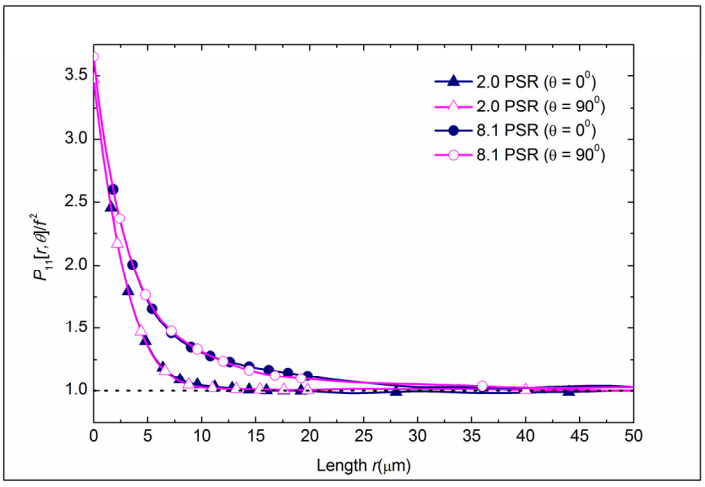

Figure 5.4: Normalized two-point correlation functions for the SiC phase measured along *Y* ($\theta = 0$) and *Z* ($\theta = 90$) axes for 2.0 and 8.1 PSR microstructures

It may also be argued that, unlike in 2D RVE determination, it is not necessary to match the two-point correlation functions for *any* randomly picked smaller window size with that of the large montage image. Rather, matching the two-point correlation functions in an average sense will be adequate since we are measuring the correlation functions on a 2D section to determine the RVE size of a 3D volume which contains a number of such sections. Following this argument, the 3D RVE size was determined as follows. Two-point correlation functions were measured along the extrusion (X) and the transverse (Y) directions for 20 montage (1 mm x 1 mm) serial sections evenly spaced along the thickness (Z) direction and the results were averaged. A smaller window of length a (along the extrusion direction) and width b (along the transverse direction) was randomly chosen on the first montage image and the two-point correlation functions were measured for the smaller window at the same location for all the 20 sections. The averaged correlation functions were compared with that for the large montage images. The frame size was progressively reduced until the averaged two-point correlation functions deviated (> 7% at any given r) from that for the montage images. If the smallest possible window size is a x b, the 3D RVE can be considered as the volume a x b x b since the microstructure is isotropic along the Y-Z plane. The concept is illustrated in Figure 5.5 which shows five sections along the thickness direction for the 8.1 PSR microstructure. Note that while the figure shows only five sections for visual clarity, the correlation functions were measured on 20 large montage images evenly spaced along the thickness direction.

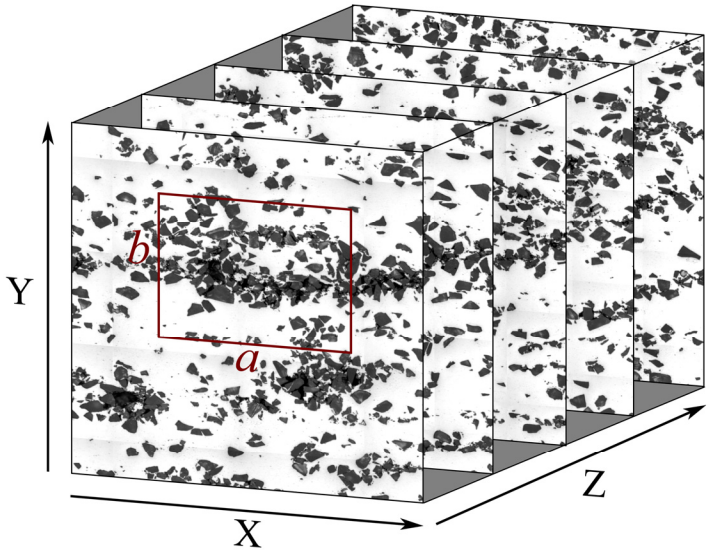

Figure 5.5: Schematic of RVE determination in 3D space

For the 2.0 PSR DRA composite, it was found that a volume of 200 μm x 100 μm x 100 μm can serve as an RVE. Figures 5.6 and 5.7 show the averaged two-point correlation functions for different window sizes considered in *X* and *Y* directions, respectively. Figure 5.8 shows the averaged two-point correlation functions for three different randomly picked sets of 200 μm x 100 μm x 100 μm volumes. The two-point correlation functions for all the three sets deviate less than 7% from that for the $1mm^2$ montage images. Three-dimensional FE simulations of 2.0 PSR DRA composites were performed on 200 μm x 200 μm x 100 μm volumes, which are twice as big as the RVE size obtained from two-point correlation functions.

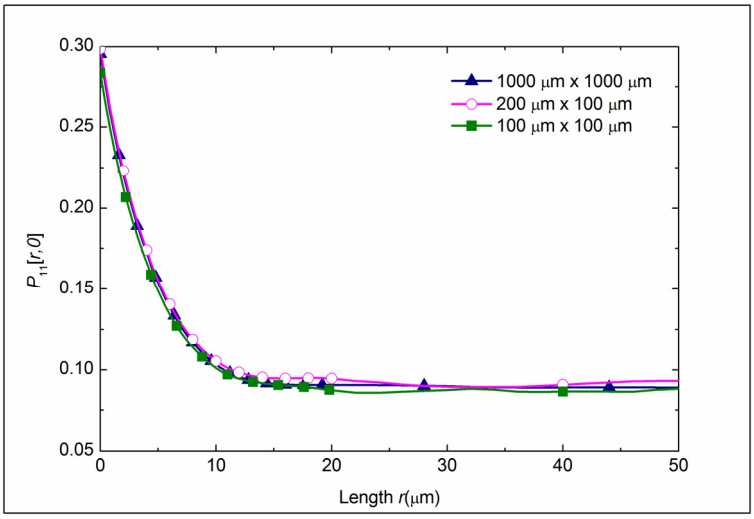

Figure 5.6: Averaged two-point correlation functions for different 2.0 PSR window sizes along the extrusion direction

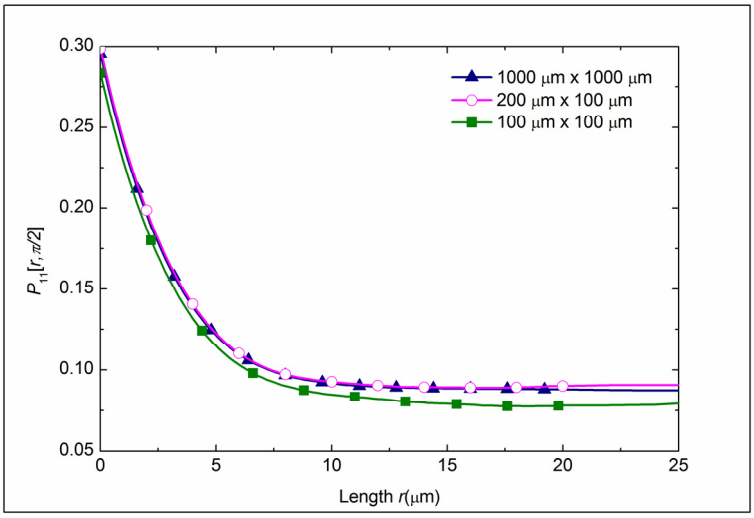

Figure 5.7: Averaged two-point correlation functions for different 2.0 PSR window sizes along the transverse direction

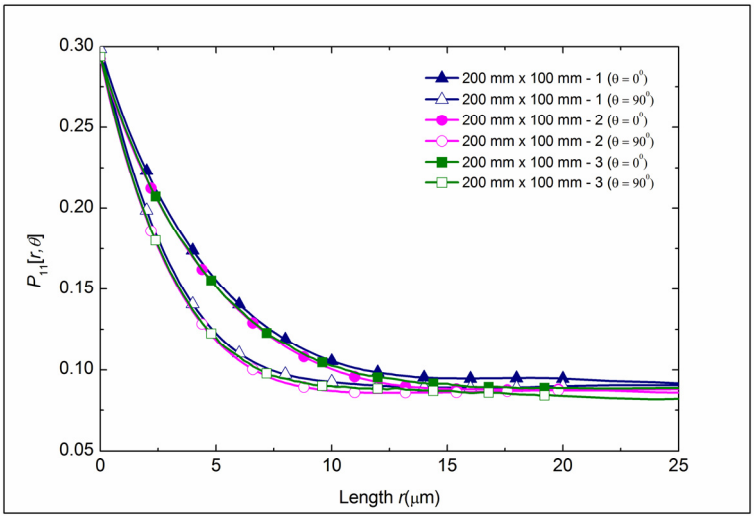

Figure 5.8: Averaged two-point correlation functions for three randomly picked sets of 200 μm x 100 μm x 100 μm volumes of 2.0 PSR microstructure

Similarly Figures 5.9, 5.10 and 5.11 show that the 8.1 PSR DRA microstructure requires a much larger volume, 400 μm x 200 μm x 200 μm, to be considered as a microstructural RVE. However, as mentioned earlier, the amount of microstructural volume available for computations along the *Z* direction is limited by the amount of material removed by serial sectioning which in this case is 100 μm. Accordingly, three-dimensional FE simulations of 8.1 PSR DRA composites were performed on 400 μm x 200 μm x 100 μm volumes.

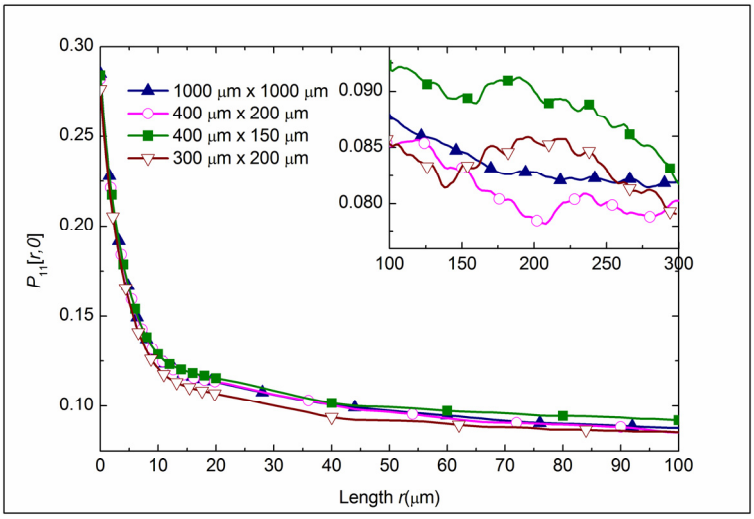

Figure 5.9: Averaged two-point correlation functions for different 8.1 PSR window sizes along the extrusion direction

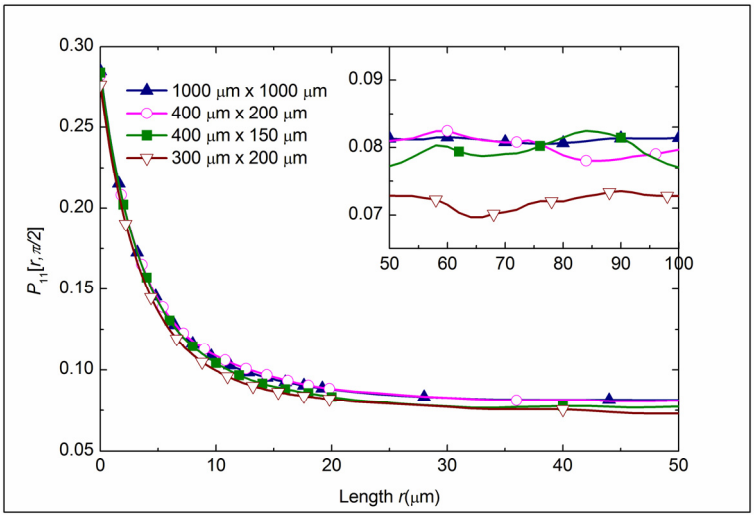

Figure 5.10: Averaged two-point correlation functions for different 8.1 PSR window sizes along the transverse direction

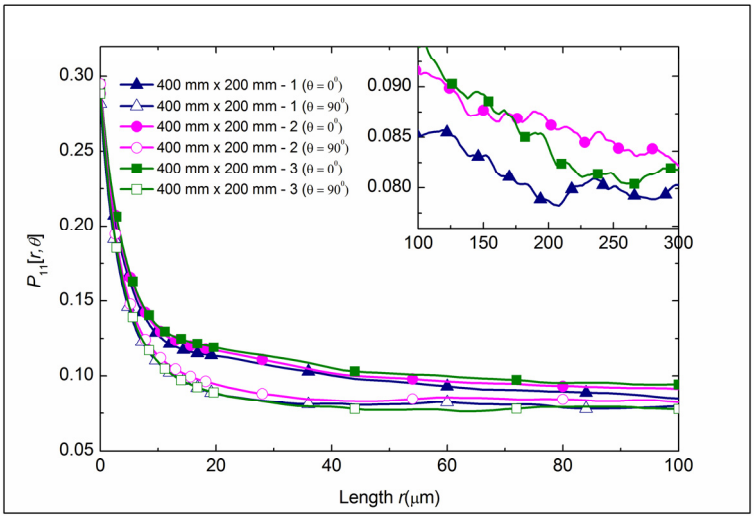

Figure 5.11: Averaged two-point correlation functions for three randomly picked sets of 400 μm x 200 μm x 200 μm volumes of 8.1 PSR microstructure

5.4 Finite Element Analysis of Real 3D Microstructures

5.4.1 Meshing of 3D volumes

The 3D reconstructed microstructural volumes were converted into FE mesh using Simpleware, a commercial software developed at University of Exeter, UK [127]. The process of generating a mesh involves first segmenting the different phases in the volume or in this case, the matrix and the reinforcement phases in the stack of 2D serial sections. The image stacks are then converted into a 3D volume and simultaneously meshed based on an orthotropic grid intersected by interfaces defining the boundaries. In effect a base cartesian mesh of the whole volume defined by the sampling rate is tetrahedralised at boundary interfaces based on cutting planes defined by interpolation points. Smooth boundaries are obtained by adjusting the interpolation points in one, or a combination, of two ways: by setting points to reflect partial volumes or by applying a multiple material anti-aliasing scheme. The process results in either a mixed

tetrahedral/hexahedral mesh or a pure tetrahedral mesh and incorporates an adaptive meshing scheme. The robust meshing algorithms in Simpleware preserve the topology and create a smooth mesh with low element distortions regardless of the complexity of the underlying 3D microstructure [128]. Figure 5.12 shows the tetrahedral FE mesh created from a 2.0 PSR microstructure of volume 200 μm x 200 μm x 100 μm.

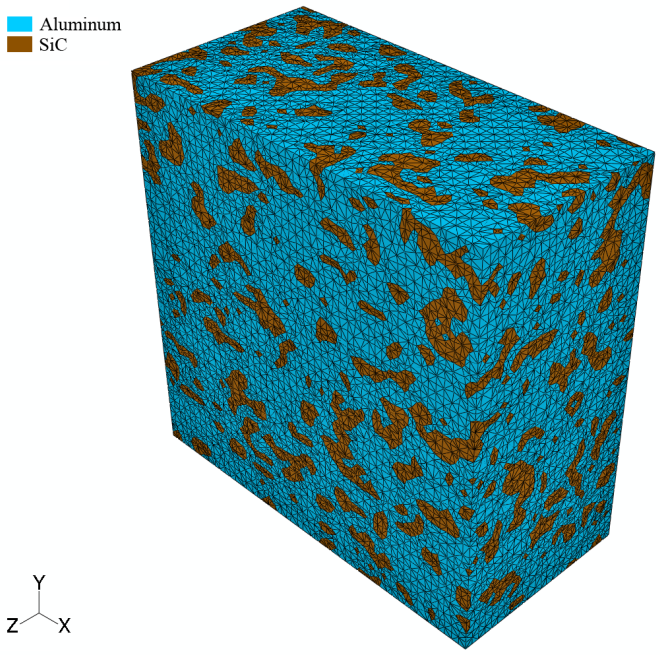

Figure 5.12: Finite element mesh created from a 2.0 PSR microstructure of volume 200 μm x 200 μm x 100 μm

The mesh size in all the 3D models used in this study is of the order of 3 μm and it can be seen from Figure 5.12 that the mesh is quite refined and conforms well to the underlying 3D microstructure. For stress/displacement analyses, first-order tetrahedral elements do not provide accurate results and hence second-order interpolation was used for all the elements. No mesh convergence studies were performed on the 3D models primarily due to computational difficulties.

5.4.2 Quasi-Static Analyses using Abaqus/Explicit

5.4.2.1 Implicit Versus Explicit Schemes

As discussed in the previous chapter, the 2D micromechanical analyses in this research were performed using the commercial finite element analysis package Abaqus/Standard which uses a traditional implicit scheme to solve the equations of motion. The implicit method is based on static equilibrium, which requires that the net force acting on each node in the model is zero at all time increments. It is characterized by the simultaneous solution of a set of linear equations to determine the unknown nodal displacements. The simultaneous solution of all the nodal equations necessitates the assembly (and subsequent inversion) of a global stiffness matrix which is an important feature of the implicit solution procedure. Abaqus/Standard uses Newton-Raphson method to iteratively solve the equations for non-linear problems. For elastic-plastic problems with a large number of degrees of freedom, the implicit scheme requires considerable computation time, disk space, and memory because of the iterative procedure involving the inversion of a large global stiffness matrix (determined by the number of degrees of freedom). The computational cost for problems based on the implicit scheme is roughly proportional to the square of the number of degrees of freedom. An alternative is to conduct quasi-static analysis using Abaqus/Explicit.

Abaqus/Explicit integrates the equations of motion explicitly through time, using the kinematic conditions at one increment to calculate the kinematic conditions at the next increment. The state of the model at the end of an increment (time $t + \Delta t$) is solely based on the displacements, velocities, and accelerations at the beginning of the increment (time t). The accelerations are integrated through the time increment Δt to

calculate the change in nodal velocity assuming that the acceleration is constant during the increment. The velocities are subsequently integrated through time and added to the displacements at the beginning of the increment to determine the displacements at the end of the increment. For the method to produce accurate results, the time increments must be quite small so that the accelerations are nearly constant during an increment. Since the time increments must be small, analyses typically require many thousands of increments, though the increments are inexpensive because there are no simultaneous equations (and consequently, no global stiffness matrix) to solve. The computational cost for Explicit is proportional to the number of elements and roughly inversely proportional to the smallest element dimension. Though primarily used to simulate dynamic events, the benefits of using Abaqus/Explicit are immediately apparent even for a static simulation when the model involves non-linearity and a large number of degrees of freedom.

5.4.2.2 Increasing the Efficiency of Quasi-Static Simulations

Static problems, such as the uniaxial tensile test, can be modeled using Abaqus/Explicit provided the state of static equilibrium does not evolve into a state of dynamic equilibrium in which inertial forces become more dominant. It is not practical to model the process in its natural time period because of the small time increments required for the explicit scheme. The loading rate can be artificially increased for computational efficiency so that the same physical event occurs in less time as long as the solution remains nearly the same as the true static solution and dynamic effects remain insignificant. The efficiency can also be increased by artificially increasing the material density in the model since the minimum stable time increment is influenced by the mass density [112]. A possible tool to identify whether or not the solution has evolved into a

state of dynamic equilibrium involves monitoring the various components of the energy balance throughout the loading process. If a simulation is quasi-static, the work applied by the external forces must be nearly equal to the internal energy of the system and the kinetic energy must not exceed a small fraction (typically 5% to 10%) of the internal energy throughout most of the process.

All the 3D analyses in this research were solved quasi-statically using Abaqus/Explicit (6.7-1) and were run at the University of Illinois' National Center for Supercomputing Applications (NCSA) supported by the National Science Foundation through TeraGrid resources [129]. The analyses details and results are given in the following subsections.

5.4.3 FE Analyses of 2.0 PSR Microstructure

A 3D microstructure of 200 μm x 200 μm x 100 μm volume was meshed with second-order tetrahedral elements (C3D10M) using Simpleware as described earlier (shown in Figure 5.12). The mesh contained 633370 elements and over 4.5 million degrees of freedom. The SiC particles were assumed to be perfectly elastic with density $\rho = 3.1 \times 10^{-6}$ μg/μm^3, Young's modulus E = 410 GPa, and Poisson's ratio $\nu = 0.14$. The aluminum matrix was assigned the constitutive properties deduced from microindentation, as discussed in Chapter 3 ($E = 70$ *GPa*, $\nu = 0.33$, $\sigma_y = 71$ MPa, $n = 0.185$) and density $\rho = 2.7 \times 10^{-6}$ μg/μm^3. The interface between the matrix and the reinforcement particles was assumed to be perfect. Uniaxial loading along the extrusion direction was simulated by fixing the displacements along all the three directions on one *Y-Z* plane and applying a non-zero displacement boundary condition along the *X* axis on the other *Y-Z* plane as shown in Figure 5.13. Note that the periodic boundary conditions

and homogeneous composite medium employed in the 2D analyses were not considered for the 3D analyses in order to reduce the computational cost. The displacement along the extrusion direction was defined as a smooth loading amplitude as shown in Figure 5.14. This was done to avoid generation of stress waves that may result from a sudden application of load (as in a linear loading rate) and cause the solution to deviate from a quasi-static state.

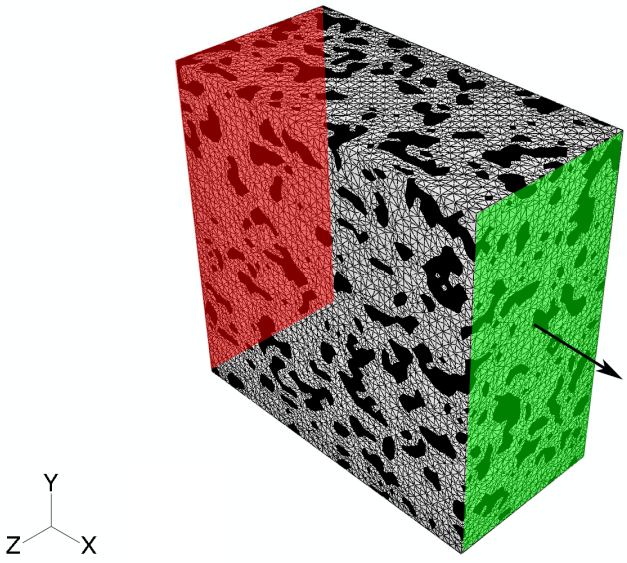

Figure 5.13: Uniaxial loading boundary conditions

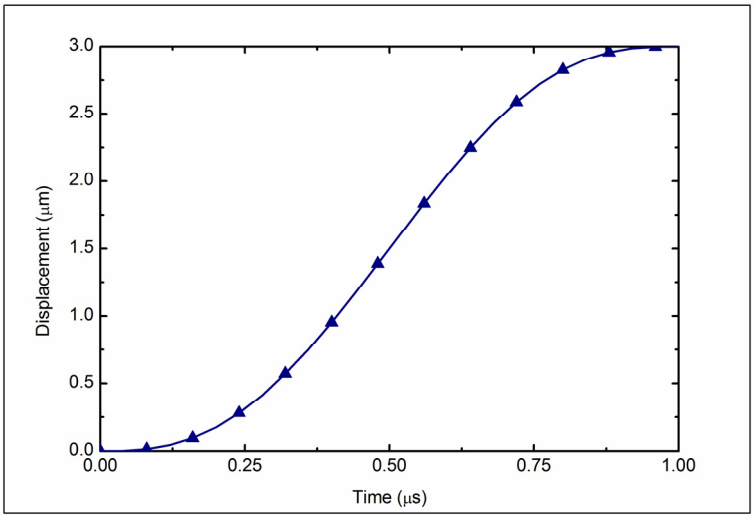

Figure 5.14: Smooth loading amplitude curve

The macroscopic stress and strain in the composite can be computed from the reaction forces and displacements output at the nodes on the surface where the displacement was applied. The nominal stress and strain values are given by:

$$\overline{S}_{11} = \frac{1}{A}\sum_{n=1}^{n=N} RF_1; \quad \overline{E}_{11} = \left(\frac{1}{d}\right)\boldsymbol{u}_1 \tag{14}$$

where A is the area of the surface on which the non-zero displacement is imposed, RF_1 is the reaction force component at the node N in the x direction, d is the length of the model along the loading direction, and $\boldsymbol{u}_1$, the applied displacement. The true stress and logarithmic strain values are determined using

$$\overline{\sigma}_{11} = \overline{S}_{11}(1+\overline{E}_{11}); \quad \overline{\varepsilon}_{11} = \ln(1+\overline{E}_{11}) \tag{15}$$

As mentioned in the previous section, it is impractical to model the uniaxial loading in its natural time period because of the extremely small time increments required for the explicit scheme. For the uniaxial loading simulation of 1.5% strain in a microstructural volume of 200 μm x 200 μm x 100 μm, it was found (by monitoring the

energy balance) that the solution remained quasi-static even when the total time period was as low as 1 μs. Also, a semi-automatic mass scaling was performed at the beginning of the analysis where the mass density of the model was increased so as to target a minimum stable time increment of 5 x 10^{-5} μs. The analysis took 4 hours to finish with four 1.6 GHz Itanium 2 processors and 2.5 GB of memory. Figure 5.15 shows the energy balance in the model for a 1 μs simulation with mass scaling. As may be observed, the kinetic energy remains a small percentage of the internal energy throughout the simulation.

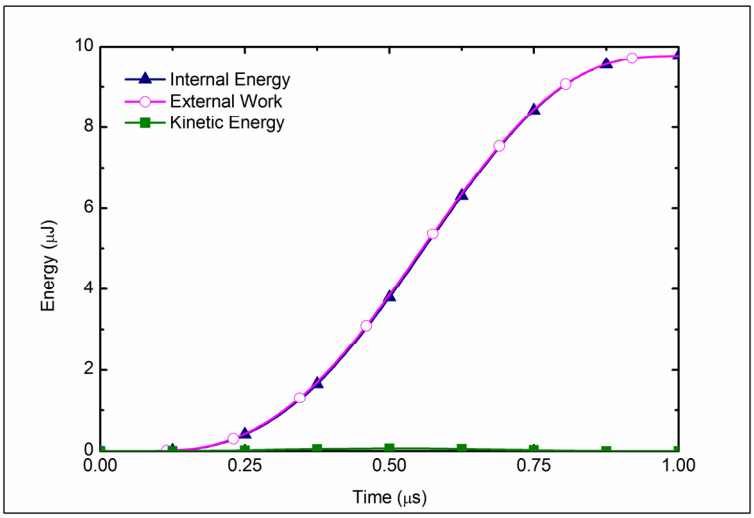

Figure 5.15: Energy balance in the FE model for a 1 μs simulation

Figures 5.16a and 5.16b shows the contour plots of maximum principal stress and equivalent plastic distribution in the model, respectively. It can be observed from Figure 5.16a that the SiC particles are the primary load bearing phase as expected. Also, Figure 5.16b shows the formation of shear bands in the matrix demonstrating that the deformation in the matrix occurs through localized shear.

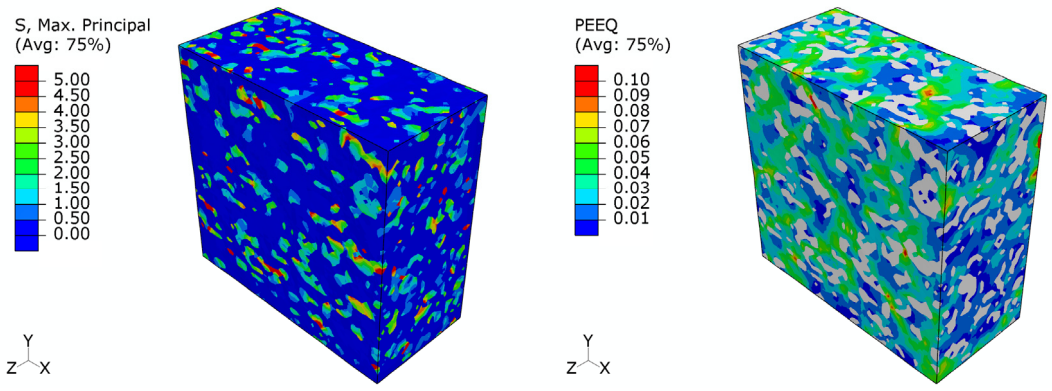

(a) (b)

Figure 5.16: Contour plots of (a) maximum principal stress (GPa) and (b) equivalent plastic distribution in the 2.0 PSR FE model

5.4.3.1 Comparison with Experimental Data

Experimental studies have shown some variability in the stress-strain data for uniaxial loading of DRA composites. Figure 5.17 shows the range in experimental results (shaded region) along with the computed curve from 3D FE simulation of a 2.0 PSR DRA composite for 1.5% strain.

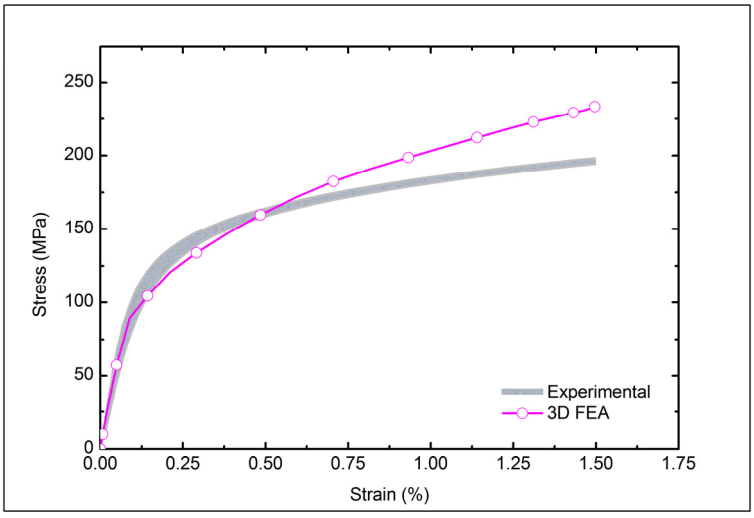

Figure 5.17: Comparison between experimental and 3D FE simulation results for uniaxial loading of a 2.0 PSR DRA composite

It is immediately apparent from the figure that while the predicted modulus and the yield strength values match quite well with the experimental data, the simulation significantly overestimates the strain hardening behavior of the composite. This may be attributed to the absence of any sort of damage mechanisms in the model. Damage initiation in DRA composites is associated with one, or a combination of the following factors: SiC fracture, decohesion at the matrix-SiC interface, or failure initiation in the matrix. The dominance of any of these damage mechanisms above others depends upon the size and spatial distribution of SiC particles as well as the matrix properties such as the composition and heat treatment history [130]. Longitudinal sections (containing the extrusion axis) of failed 2.0 PSR tensile test samples were observed under optical microscope for qualitative investigation of the failure mechanisms. Figures 5.18a and 5.18b show single fields of view from the gage section of the tensile test specimen close to the fracture surface (a), and away from the fracture surface (b). Cracked SiC particles are highlighted in both the micrographs. While both the micrographs show some cracked SiC particles, no interfacial or matrix damage is observed. Also note that the number of cracked particles is of the same order in both the micrographs. This suggests that while the cracking of SiC particles is prevalent in this microstructure, the final fracture of the material is characterized by localized matrix failure.

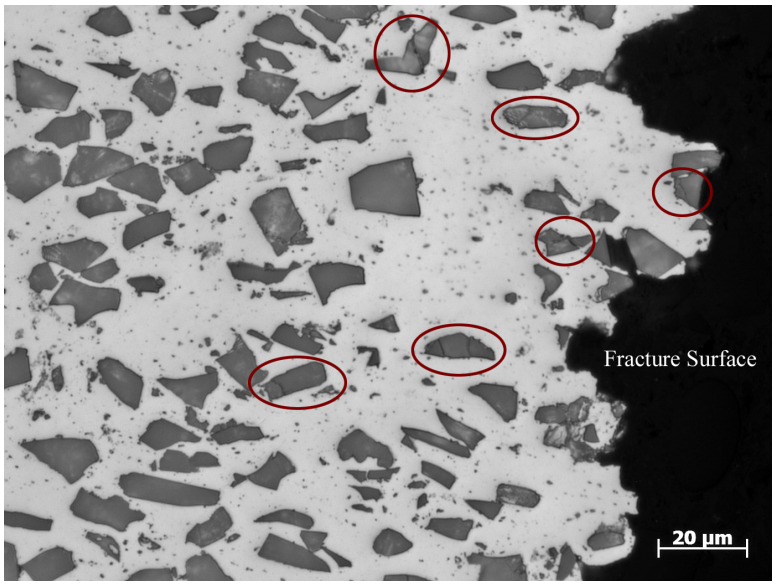

(a)

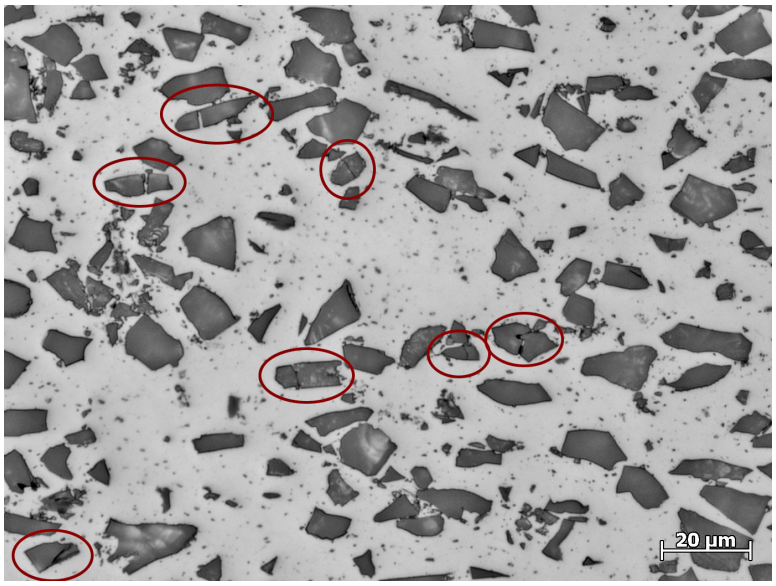

(b)

Figure 5.18: Optical micrographs from the gage section of a 2.0 PSR tensile test specimen (a) close to the fracture surface, and (b) away from the fracture surface showing cracked SiC particles

SEM image of the fracture surface of 2.0 PSR tensile test sample is given in Figure 5.19 clearly showing the ductile fracture of the aluminum matrix. Very little, if any, SiC particle pullout is observed.

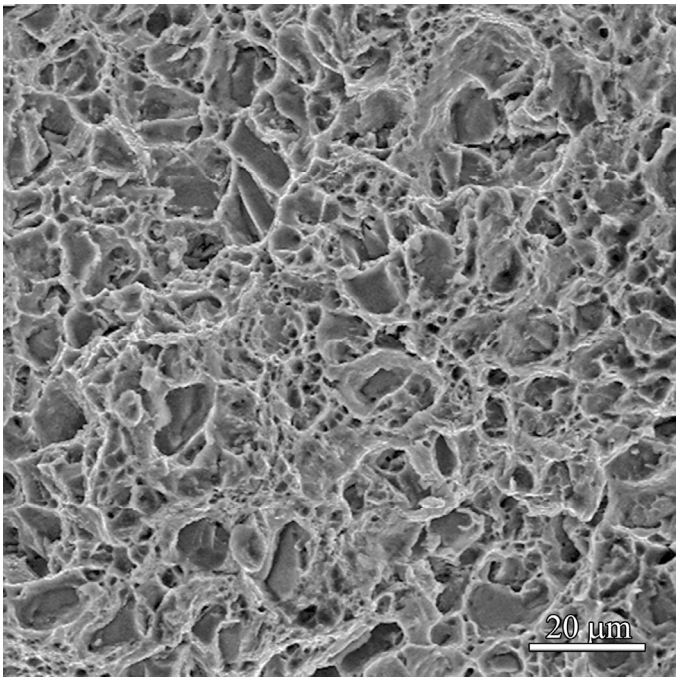

Figure 5.19: SEM image of the fracture surface of a 2.0 PSR tensile test specimen

Since this research concerns uniaxial loading simulations for less than 2% strain which is well below the failure strain of the material (> 6%), it is safe to assume that the dominant damage mechanism is SiC particle cracking. A brittle cracking constitutive model was added to the SiC phase in the model of which the details are given in the next section.

5.4.3.2 Brittle Cracking Model for SiC Particles

A simple Rankine criterion was used to describe the brittle cracking behavior in SiC particles. According to this criterion, a crack is assumed to be formed when the

maximum principal tensile stress exceeds the tensile strength of SiC. The crack surface is taken to be normal to the direction of the maximum tensile principal stress. Subsequent cracks may form with crack surface normals in the direction of maximum principal tensile stress that is orthogonal to the directions of any existing crack surface normals at the same point. Brittle cracking in Abaqus is a smeared crack model which does not track individual cracks: instead, constitutive calculations are performed independently at each material point of the finite element model. The presence of cracks enters into these calculations by the way in which the cracks affect the stress and material stiffness associated with the material point.

Tensile strength of ceramics such as SiC depends to a large extent on the method of preparation and number/size of defects in the material. While experimental tensile strength data is reported for SiC in bulk (~ 0.25 GPa [131]), fiber (2.5–3.5 GPa [132]), and whisker (7-35 GPa [133]) form, no such data is available for SiC particulates. The tensile strength of SiC particulates is expected to be much higher than that for bulk SiC but lower than SiC in fiber/whisker form. Due to the lack of better experimental data, a value of 2 GPa was assumed as the tensile strength of SiC particles. Incorporation of brittle cracking behavior for SiC phase in the 3D model leads to a number of computational difficulties, including the premature termination of the analysis due to excessive distortion of elements that no longer carry stress. Abaqus allows for a brittle failure criterion where the element is removed from the analysis once it loses its ability to carry stress in order to reduce problems due to distortion. Excessive distortion is also affected by the post-failure stress-strain data as well as the post-failure shear retention for the material. In the current research, once a crack is formed at a material point, the stress

and the shear modulus of that point were assumed to linearly reduce to zero at 5% strain after which the element is removed from the analysis. Note that further experiments are required to gain accuracy in post-failure behavior of SiC particles.

Figure 5.20 shows the stress-strain curve from the FE simulation of a 200 μm x 200 μm x 100 μm model of 2.0 PSR microstructure with brittle cracking of SiC particles. As may be observed, the simulated stress-strain curve matches quite well with the experimental data.

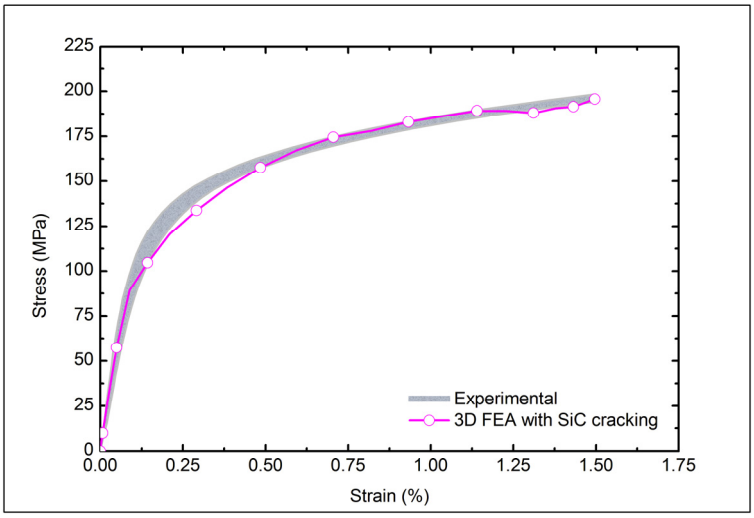

Figure 5.20: Comparison between experimental data and 3D FE simulation with SiC particle cracking for uniaxial loading of a 2.0 PSR DRA composite

The complementary cumulative maximum principal stress distribution at 1.5% strain in the SiC particles with and without the brittle cracking constitutive behavior added to the model is given in Figure 5.21. It may be observed that the maximum principal stress in the SiC particles reduces to zero beyond 2 GPa, the specified tensile strength of SiC in the model.

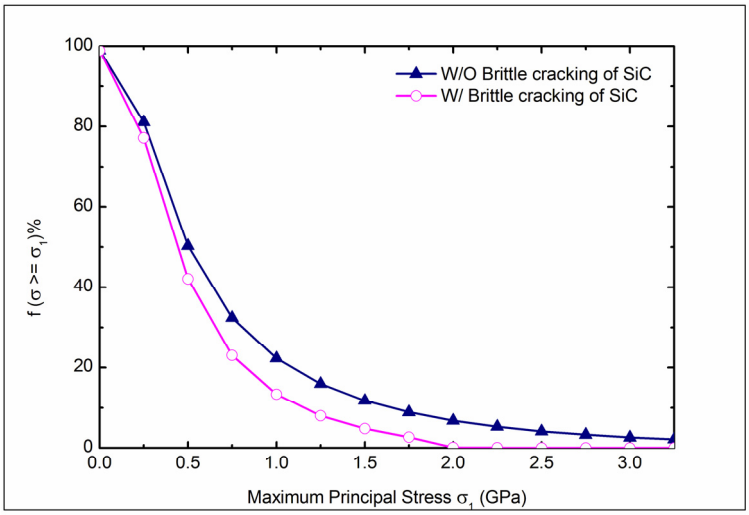

Figure 5.21: Complementary cumulative maximum principal stress distribution at 1.5% strain in the SiC particles with and without the brittle cracking constitutive behavior

In order to validate that a 200 μm x 200 μm x 100 μm volume can be considered as an RVE for uniaxial loading simulation, FE analyses were carried out on a larger volume of 400 μm x 200 μm x 100 μm as well as three different realizations of 200 μm x 200 μm x 100 μm volumes. Figure 5.22 shows that the stress-strain curves predicted by all the models are in close agreement with the experimental data. Similarly, Figures 5.23 and 5.24 illustrate that the maximum principal stress and equivalent plastic strain distributions in SiC and aluminum matrix in all the four models are also in good agreement, suggesting that a 200 μm x 200 μm x 100 μm volume can be considered an RVE for the 2.0 PSR microstructure.

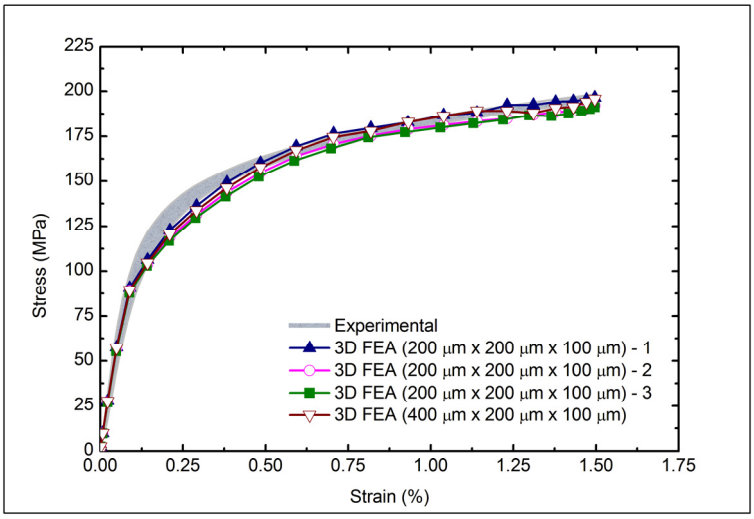

Figure 5.22: Computed stress-strain curves for three different realizations of 200 μm x 200 μm x 100 μm volumes and one 400 μm x 200 μm x 100 μm volume of 2.0 PSR microstructure

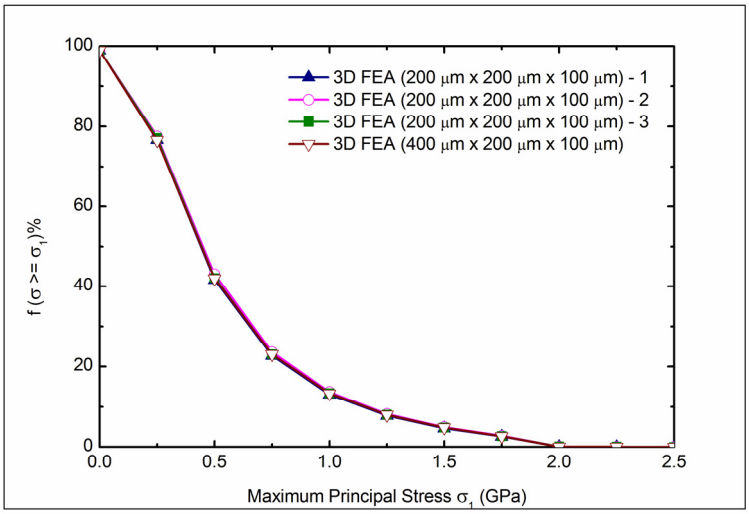

Figure 5.23: Complementary cumulative distributions of maximum principal stress in SiC particles for three different realizations of 200 μm x 200 μm x 100 μm volumes and one 400 μm x 200 μm x 100 μm volume of 2.0 PSR microstructure

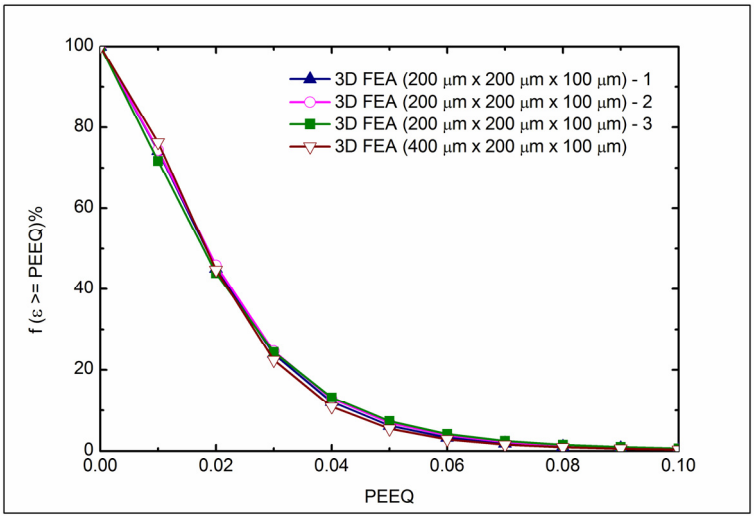

Figure 5.24: Complementary cumulative distributions of equivalent plastic strain in the matrix for three different realizations of 200 μm x 200 μm x 100 μm volumes and one 400 μm x 200 μm x 100 μm volume of 2.0 PSR microstructure

5.4.3.3 Comparison with 2D Plane-Stress Model

While it was shown in the previous chapter that 2D plane-stress simulations do not accurately predict the deformation behavior of these composites, it is of interest to compare the local stress/strain distributions in the 2D model with that of the 3D model. Complementary cumulative maximum principle stress distributions in the SiC particles for 2D and 3D (with brittle cracking constitutive behavior) models at 1.5% strain are given in Figure 5.25, which shows that the 2D model greatly underestimates the load bearing capacity of SiC particles in the DRA composite. But the deformation behavior of the matrix is similar in both 2D and 3D simulations as shown in Figure 5.26, the complimentary cumulative equivalent plastic strain distributions in the models. Figures 5.27a and 5.27b show the contour plots of equivalent plastic strain distribution in the matrix for a small window from the 2D analysis and the *X*-*Y* plane of the 3D analysis,

respectively. The shear deformation in the matrix is clearly captured in both the 2D and 3D models.

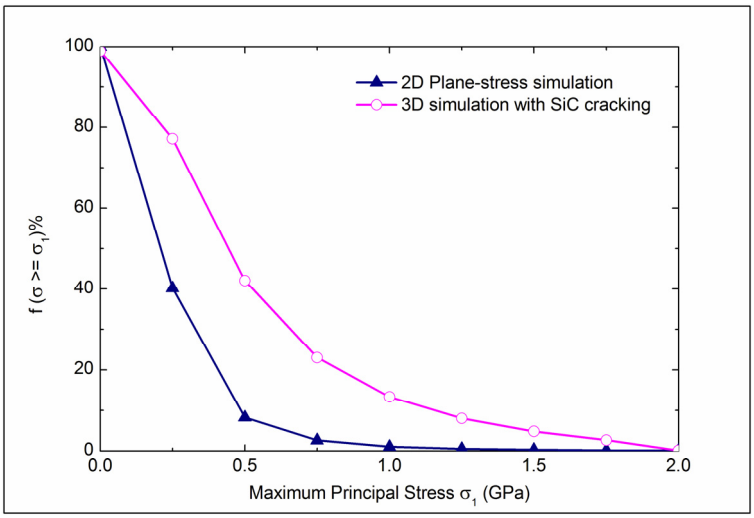

Figure 5.25: Complementary cumulative maximum principle stress distributions in the SiC particles for 2D and 3D FE simulations of 2.0 PSR microstructure

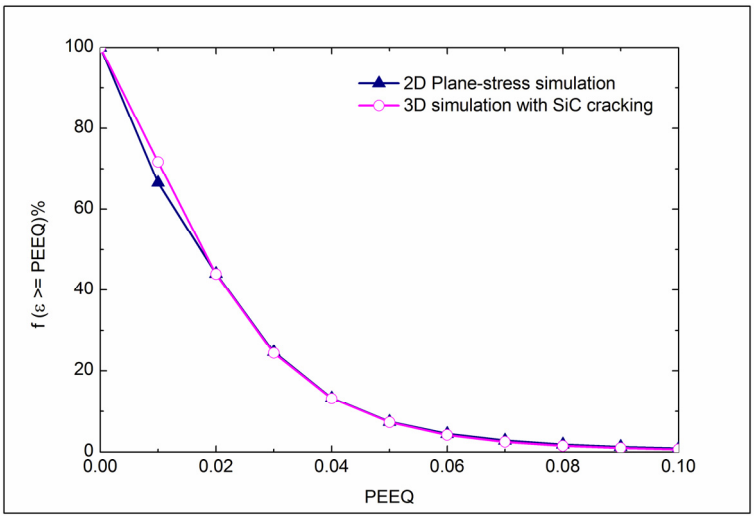

Figure 5.26: Complementary cumulative equivalent plastic strain distributions in the matrix for 2D and 3D FE simulations of 2.0 PSR microstructure

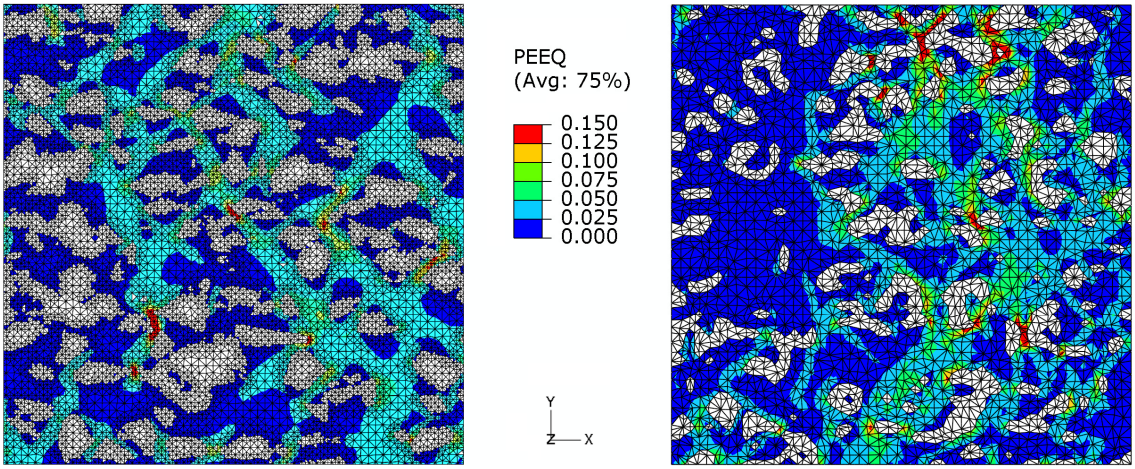

(a) (b)

Figure 5.27: Contour plots of equivalent plastic strain distributions in the matrix for (a) 2D and (b) 3D FE simulations of 2.0 PSR microstructure

5.4.4 FE Analysis of 8.1 PSR DRA Microstructure

It was shown earlier in this chapter using two-point correlation functions that the 3D microstructural RVE for the 8.1 PSR DRA composite is of the order of 400 μm x 200 μm x 200 μm. However, since the amount of microstructural volume available along the *Z* direction is limited by the amount of material removed by serial sectioning which in this case is 100 μm, three-dimensional FE simulations of the 8.1 PSR DRA composites were performed on 400 μm x 200 μm x 100 μm volumes. Figure 5.28 shows the FE model for the 8.1 PSR microstructure.

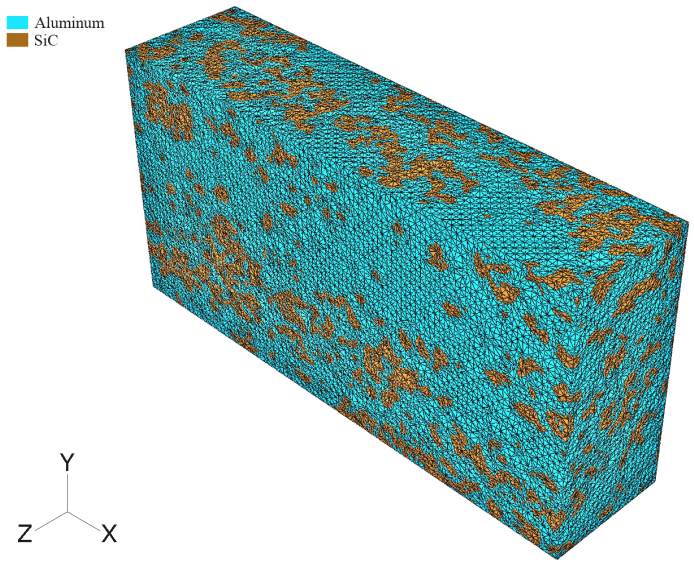

Figure 5.28: FE mesh of a 400 μm x 200 μm x 100 μm volume of 8.1 PSR microstructure

Experimental uniaxial tests have shown that the yield strength of the 8.1 PSR DRA composite is significantly lower (15-20%) than that for the 2.1 PSR composite. Two-dimensional plane-stress analyses failed to capture this difference, as shown in chapter 4. It was also noted in Chapter 4 that the clustering of SiC particles in DRA composites with a high PSR value leads to the formation of porosity in the clustered region. While the 2.1 PSR microstructure showed less than 1% porosity, the 8.1 PSR microstructure was found to have around 6% porosity. The presence of porosity is expected to affect the mechanical response of the 8.1 PSR microstructure. Note that the 2D analyses and the 3D FE model shown in Figure 5.28 neglect the porosity in the sample. In order to investigate the effect of porosity in the mechanical response of the composite, the porosity was included in an FE model. This was done by doing a three-phase segmentation of the serial sections (instead of a two-phase binary segmentation) and meshing only the aluminum

and SiC phase. Figure 5.29 shows one section from the 3D stack of images showing the three different phases.

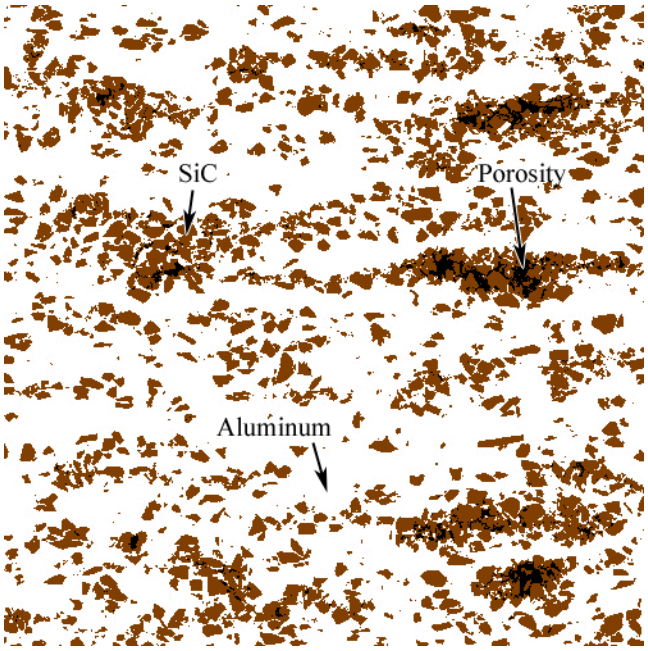

Figure 5.29: Three-phase segmentation of 8.1 PSR microstructure

Figures 5.30a and 5.30b show a 400 μm x 200 μm x 100 μm volume of the 8.1 PSR microstructure without and with the porosity incorporated in the model, respectively. A high-porosity SiC cluster region is shown highlighted in the figures. The FE mesh is not shown for clarity. Note that the porosity is treated as part of the matrix in two-phase segmentation (Figure 5.30a).

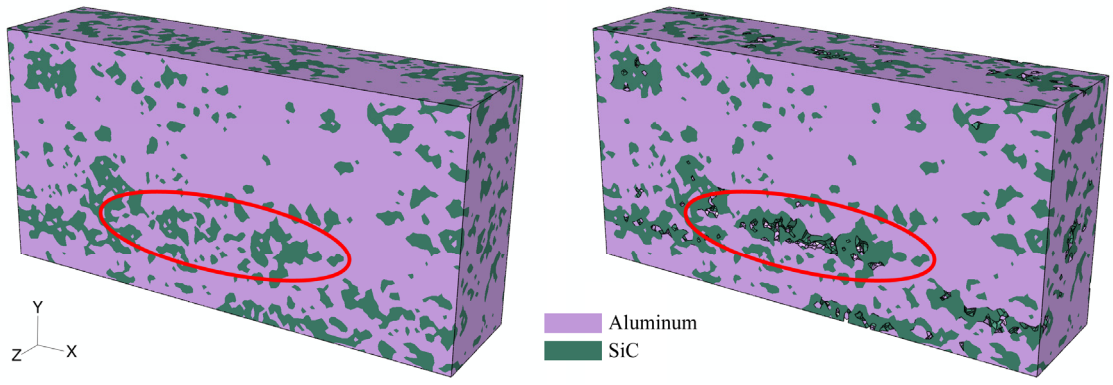

(a) (b)

Figure 5.30: 400 μm x 200 μm x 100 μm volume of the 8.1 PSR microstructure (a) without and (b) with the porosity incorporated in the model

The models were analyzed for mechanical response under uniaxial loading along the extrusion direction. The boundary conditions and the material constitutive models (including the brittle cracking model for SiC) used were the same as that described earlier for the 2.0 PSR microstructure. It may be noted that though the porosity was incorporated in the model, no damage models were specified for the aluminum matrix since this work concerns the mechanical response under small strains where the predominant damage mechanism is assumed to be SiC particle cracking. Figure 5.31 shows the computed stress-strain curves for the 8.1 PSR microstructure with and without the porosity along with experimental results. As can be observed from the figure, the simulated curve is in good agreement with the experimental data when porosity is included in the model. The discontinuities (or kinks) observed in the plastic flow regime arise from the removal of elements (representing cracked SiC material points) from the model.

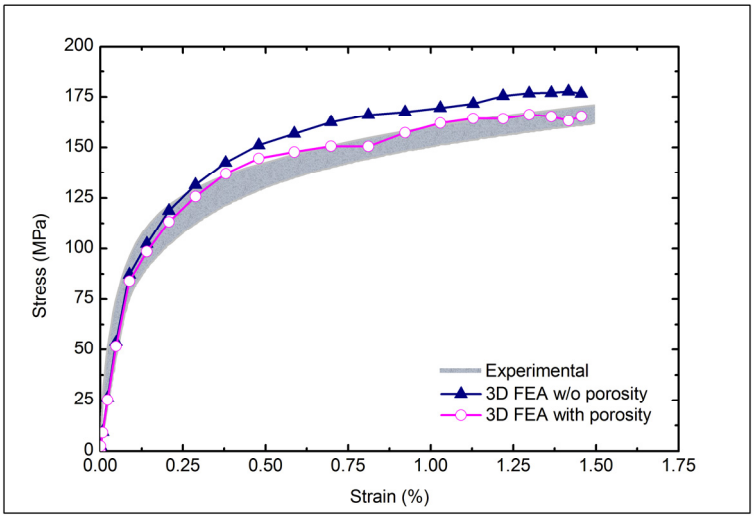

Figure 5.31: Comparison between experimental and 3D FE simulation results for uniaxial loading of 8.1 PSR DRA composite

Further analyses were carried out on a larger volume of 500 μm x 200 μm x 100 μm as well as another realization of 400 μm x 200 μm x 100 μm volume. Figure 5.32 shows that the stress-strain curves predicted by all the models fall within the range of experimental data. Similarly, Figures 5.33 and 5.34 show that the maximum principal stress and equivalent plastic strain distributions in SiC and aluminum matrix in all the three models are also in good agreement. Hence a 400 μm x 200 μm x 100 μm volume may be considered an RVE for uniaxial loading simulations of the 8.1 PSR microstructure.

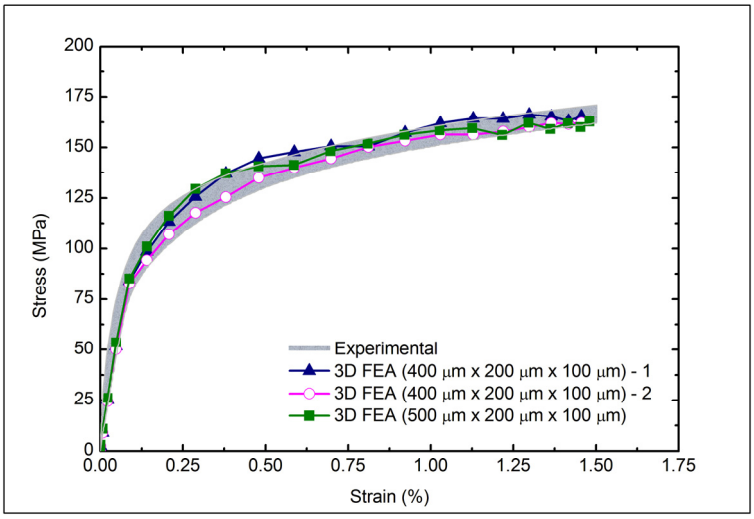

Figure 5.32: Computed stress-strain curves for two different realizations of 400 μm x 200 μm x 100 μm volumes and one 500 μm x 200 μm x 100 μm volume of 8.1 PSR microstructure

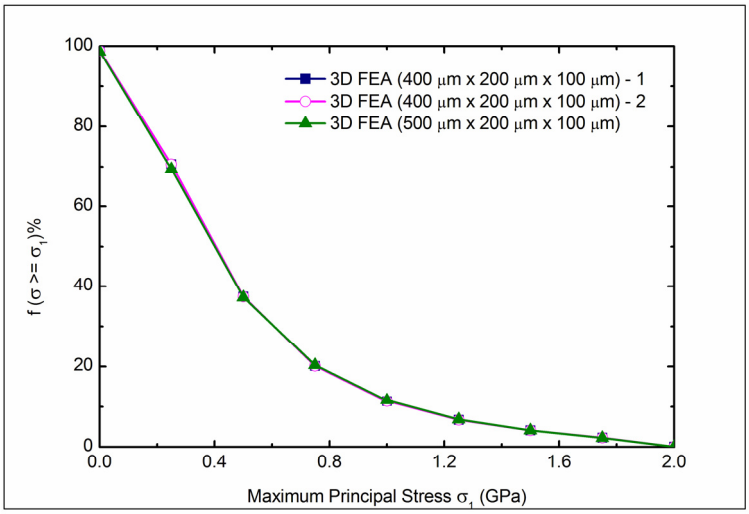

Figure 5.33: Complimentary cumulative maximum principal stress distributions in SiC particles for two different realizations of 400 μm x 200 μm x 100 μm volumes and one 500 μm x 200 μm x 100 μm volume of 8.1 PSR microstructure

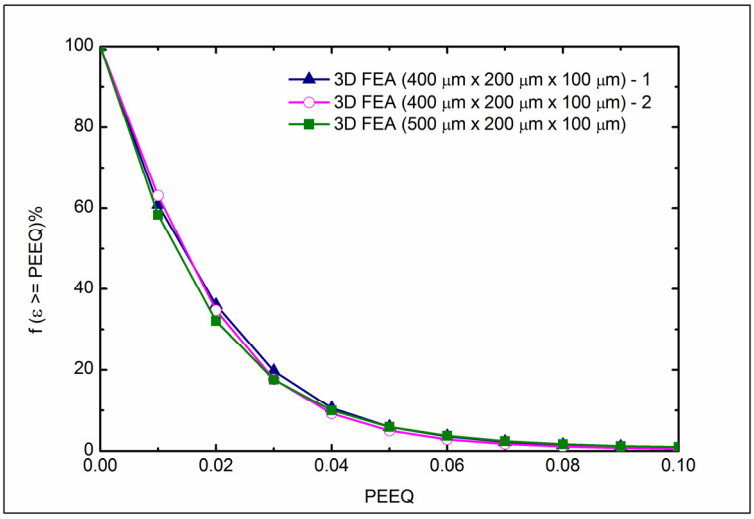

Figure 5.34: Complimentary cumulative equivalent plastic strain distributions in the matrix for two different realizations of 400 μm x 200 μm x 100 μm volumes and one 500 μm x 200 μm x 100 μm volume of 8.1 PSR microstructure

5.4.4.1 Comparison with 2.0 PSR Microstructure

As shown previously in Chapter 4, the macroscopic stress-strain behavior of the powder metallurgy processed DRA composites is affected by the particle size ratio of aluminum and SiC powders. It was also shown earlier that 2D plane-stress analyses of 2.0 and 8.1 PSR microstructures fail to capture the differences in stress-strain behavior of these composites. It is of interest to investigate whether or not the 3D analyses bring out these differences. Figure 5.35 show the stress-strain curves predicted by 400 μm x 200 μm x 100 μm volumes of 2.0 PSR and 8.1 PSR microstructures. Note that while the 8.1 PSR microstructures were evaluated with and without porosity, the effect of porosity was not considered for the 2.0 PSR microstructure since experimental studies have shown that the amount of porosity in 2.0 PSR microstructure is negligible. It may be noted that while porosity needed to be included in the 8.1 PSR models in order to match the experimental results, stress-strain curves for 2.0 and 8.1 PSR microstructure show difference even

without incorporating porosity. Figures 5.36 and 5.37 show the complementary cumulative distributions of maximum principal stress in the SiC particles and equivalent plastic strain in the matrix for all the three models, respectively.

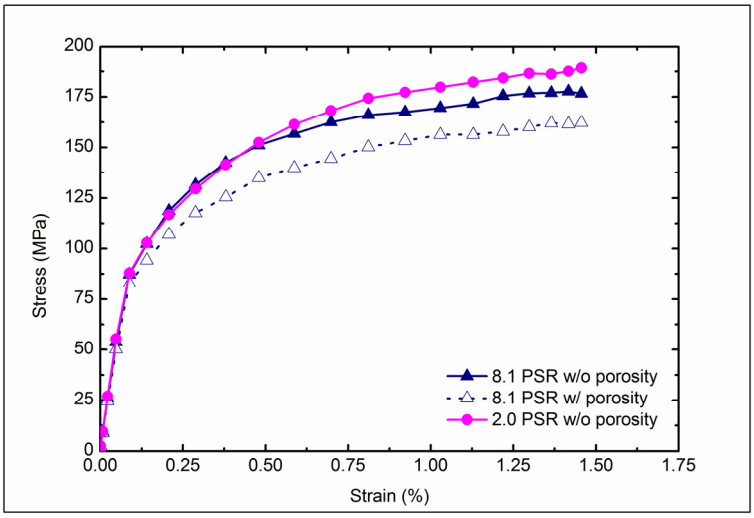

Figure 5.35: Stress-strain curves predicted by 400 μm x 200 μm x 100 μm volumes of 2.0 PSR and 8.1 PSR microstructures

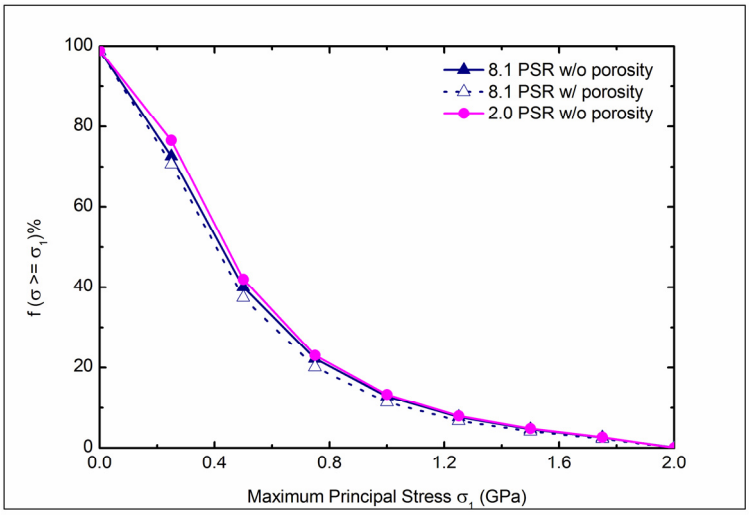

Figure 5.36: Complementary cumulative distributions of maximum principal stress in SiC particles from 3D analyses of 2.0 PSR and 8.1 PSR microstructures

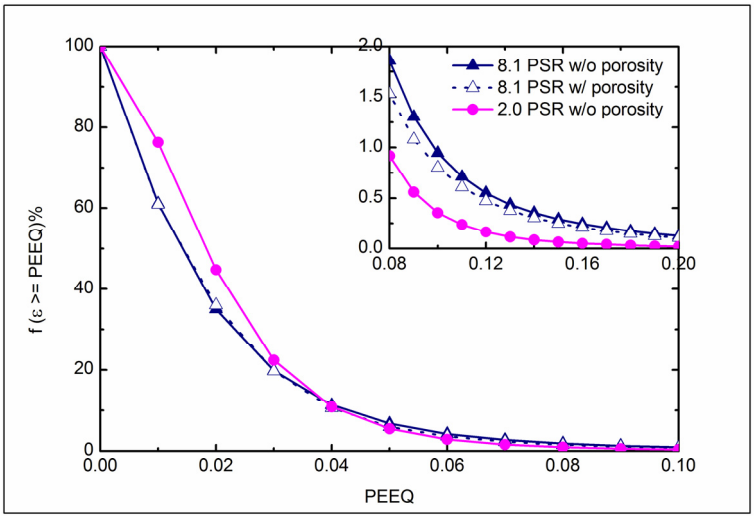

Figure 5.37: Complementary cumulative distributions of equivalent plastic strain in the matrix from 3D analyses of 2.0 PSR and 8.1 PSR microstructures

Though the stress distribution in the particles are similar for both 2.0 and 8.1 PSR microstructures, marked difference can be observed in the plastic strain distribution in the matrix. While the matrix has yielded completely in all the three cases, the percentage of matrix material points above a given value of plastic strain is much lower for the 8.1 PSR microstructure compared to the 2.0 PSR microstructure at lower values of strain (< 0.03). Also, the distribution curves cross over beyond plastic strain value of ~ 0.03 with the 8.1 PSR microstructure exhibiting more strained material points at higher values of equivalent plastic strain. This may be explained as follows: the overall plastic flow in the matrix is expected to be easier in the 8.1 PSR microstructure because of the presence of particle free regions in the 8.1 PSR microstructure along the extrusion direction resulting from the clustering of SiC particles and consequently, the overall strain hardening in the matrix is less for the 8.1 PSR microstructure. But the clustering of particles also results in localized straining of the matrix within the clustered regions compared to the 2.0 PSR microstructure where the SiC particles are more uniformly distributed. This explains why

the 8.1 PSR model exhibits more strained material points at higher values of equivalent plastic strain. Similar behavior is observed on looking at the von Mises stress distribution in the matrix for the three models, as shown in Figure 5.38.

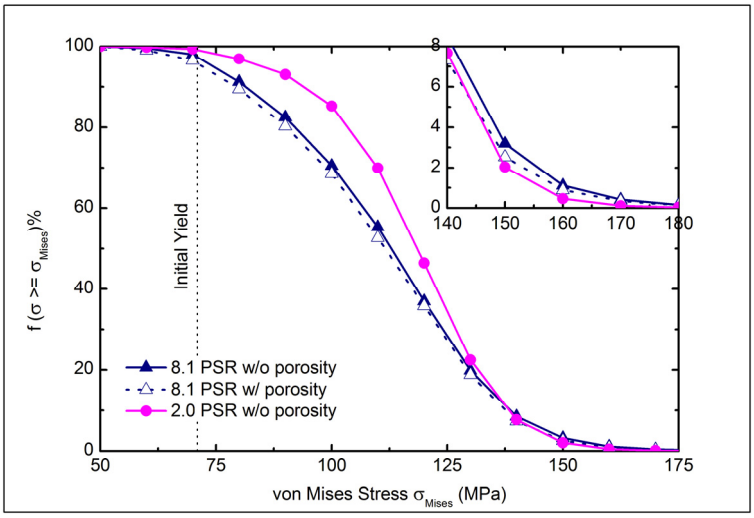

Figure 5.38: Complementary cumulative distributions of von Mises stress in the matrix from 3D analyses of 2.0 PSR and 8.1 PSR microstructures

Figure 5.36 suggests that the stress distribution in the SiC particles for the 8.1 PSR microstructure is similar to that for the 2.0 PSR microstructure. In order to verify this, failed tensile test samples of 8.1 PSR composite were sectioned along the extrusion direction and were observed under optical microscope. Figures 5.39a and 5.39b show optical micrographs of an 8.1 PSR sample at high and low magnifications, respectively. The cracked SiC particles are highlighted in the high magnification image. Note that the volume fraction of the cracked particles is of the same order as that observed in the 2.0 PSR microstructure, shown earlier in Figure 5.14. Also, the low magnification image reveals that the pores in the SiC cluster regions have grown considerably in the failed

samples, suggesting that the porosity and pore growth are important factors in the deformation of these materials.

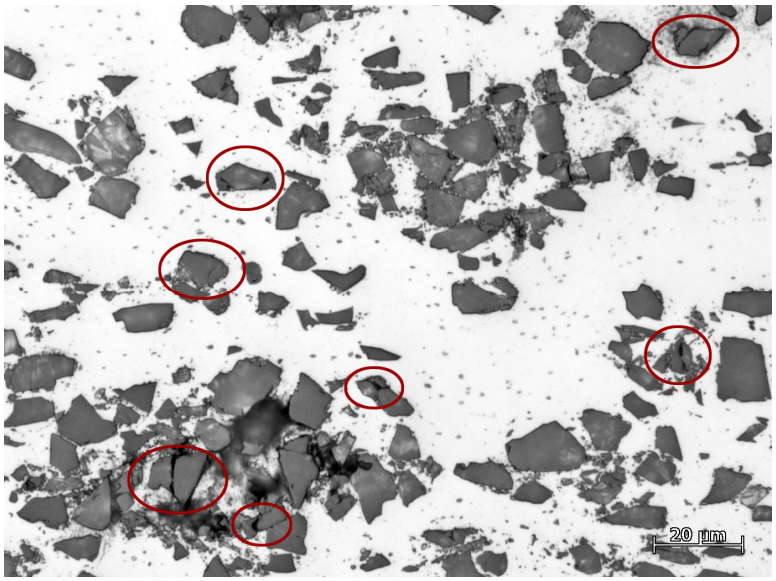

(a)

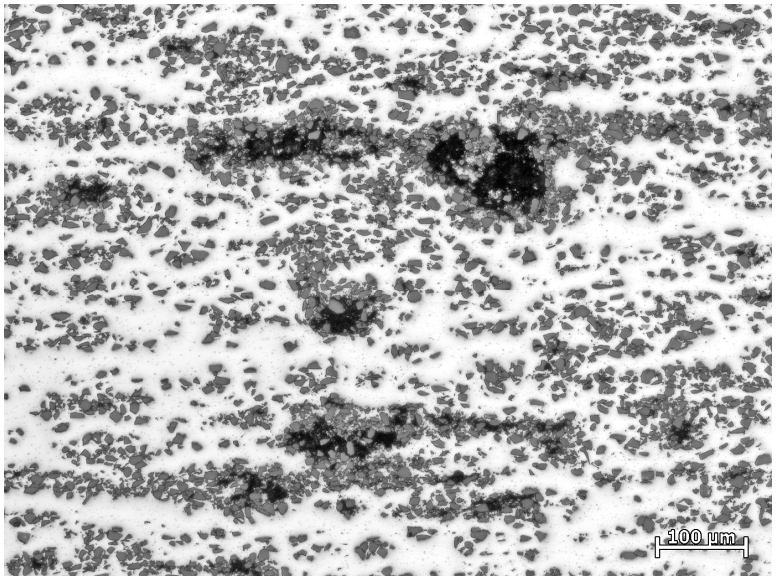

(b)

Figure 5.39: Optical micrographs of failed 8.1 PSR tensile test sample at (a) high magnification and (b) low magnification

Figures 5.40a and 5.40b show the SEM images of the fracture surface of an 8.1 PSR sample. The fracture surface of 8.1 PSR sample was observed to be rougher compared to 2.0 PSR sample. This may be attributed to the presence of porosity in the sample. No particle pullout was observed in the 8.1 PSR sample and the composite failure is seen to be dominated by the ductile fracture of the matrix, similar to the 2.0 PSR sample.

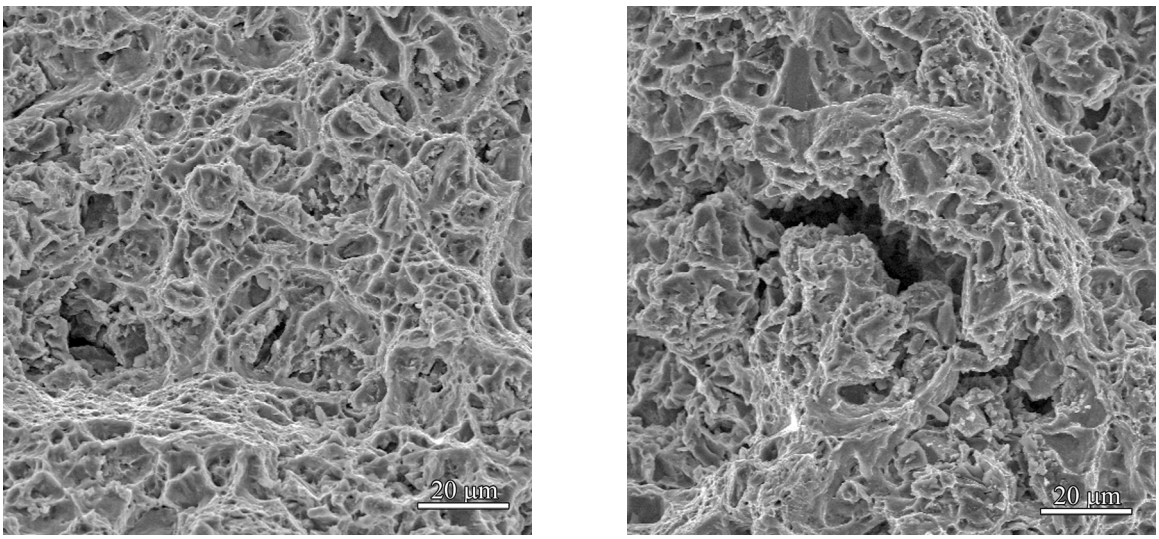

(a) (b)

Figure 5.40: SEM images of the fracture surface of failed 8.1 PSR tensile test specimen

5.4.4 FE Analysis of 3.1 PSR DRA Microstructure

Three-dimensional FE simulation of uniaxial loading along the extrusion direction was performed on a 400 μm x 200 μm x 100 μm volume of the 3.1 PSR microstructure. The FE mesh is shown in Figure 5.41. Density measurements, as shown earlier in chapter 4, have shown that the 3.1 PSR composite contains 3-4% of porosity. Porosity was incorporated in the FE model in the same way as described for the 8.1 PSR microstructure in the previous section. The boundary conditions and the material

constitutive models (including the brittle cracking model for SiC) used were the same as that described earlier for the 2.0 PSR microstructure. The computed stress-strain curve is in good agreement with the experimental results, as shown in Figure 5.42.

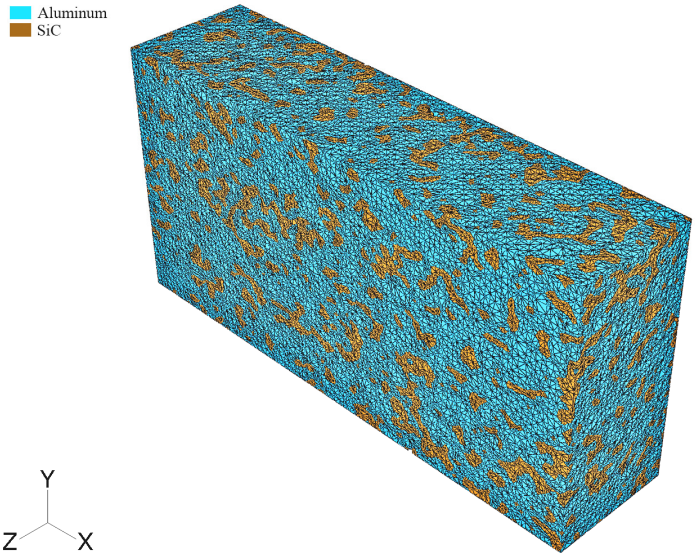

Figure 5.41: FE mesh of a 400 μm x 200 μm x 100 μm volume of 3.1 PSR microstructure

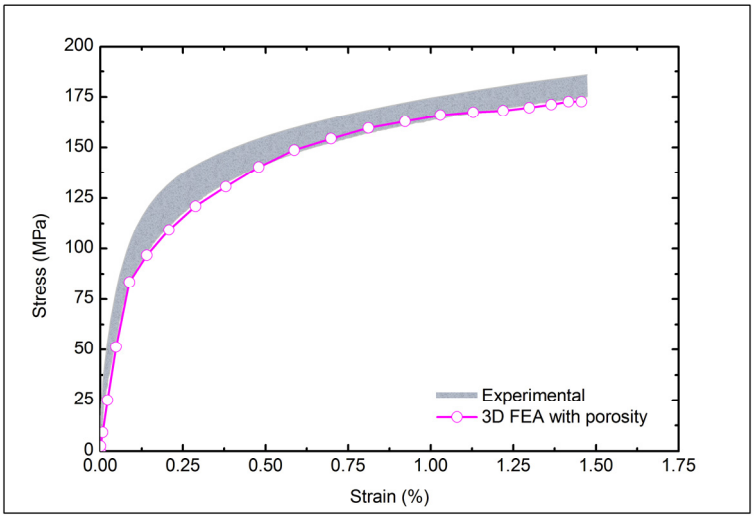

Figure 5.42: Comparison between experimental and 3D FE simulation results for uniaxial loading of 3.1 PSR DRA composite

5.4.5 FE Analysis of Ti-6Al-4V-1B Microstructure

Serial-sectioning of the Ti-6Al-4V-1B alloy, as mentioned earlier, was performed in a direction normal to the extrusion axis and 75 sections (with approximately 0.7 μm space between successive sections) were available for 3D modeling. This limits the thickness along the extrusion direction to ~ 52 μm and accordingly, a 52 μm x 52 μm x 52 μm volume was chosen for finite element analysis. The 3D microstructure was meshed with quadratic interpolation tetrahedral elements (C3D10M) using Simpleware. The mesh contained 889150 elements and over 6 million degrees of freedom. Figure 5.43 shows the FE mesh.

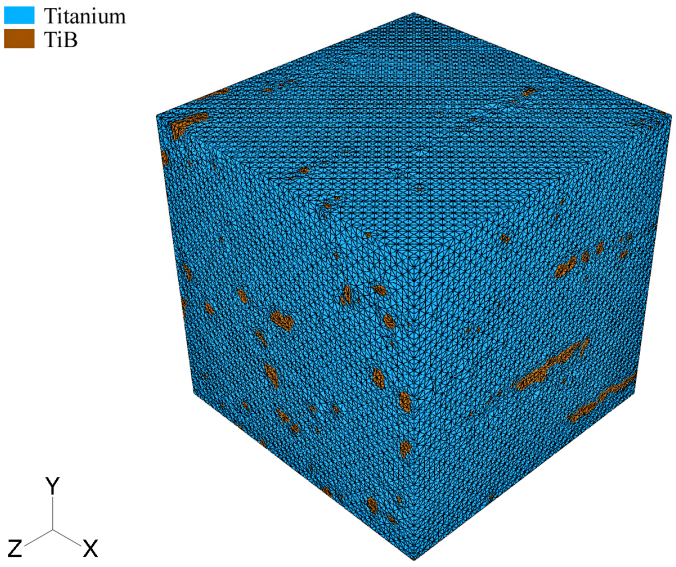

Figure 5.43: FE mesh of a 52 μm x 52 μm x 52 μm volume of extruded Ti-6Al-4V-1B microstructure

The TiB whiskers were assumed to be perfectly elastic with density $\rho = 4.51 \times 10^{-6}$ $\mu g/\mu m^3$, Young's modulus E = 466 GPa, and Poisson's ratio $\nu = 0.15$. Dr. Tamirisakandala and his colleagues at AFRL have recently estimated the TiB fracture

strength using whisker fragmentation analysis as 5.04±1.71 GPa [134]. Accordingly, the brittle cracking constitutive behavior for TiB was added to the model with a TiB tensile strength of 5 GPa. The Ti-6Al-4V matrix was assigned the constitutive properties deduced from microindentation, as discussed in Chapter 3 ($E = 115\ GPa$, $\nu = 0.33$, $\sigma_y =$ 1025 MPa, $n = 0.1$) and density $\rho = 4.5 \times 10^{-6}$ μg/μm^3. The interface between the matrix and the whiskers was assumed to be perfect. Uniaxial loading along the extrusion direction was simulated by fixing the displacements along all the three directions on one *X*-*Y* plane and applying a non-zero displacement boundary condition along the *Z* axis on the other *X*-*Y* plane. Figure 5.44 shows that the computed stress-strain curve from the model is in good agreement with the experimental data.

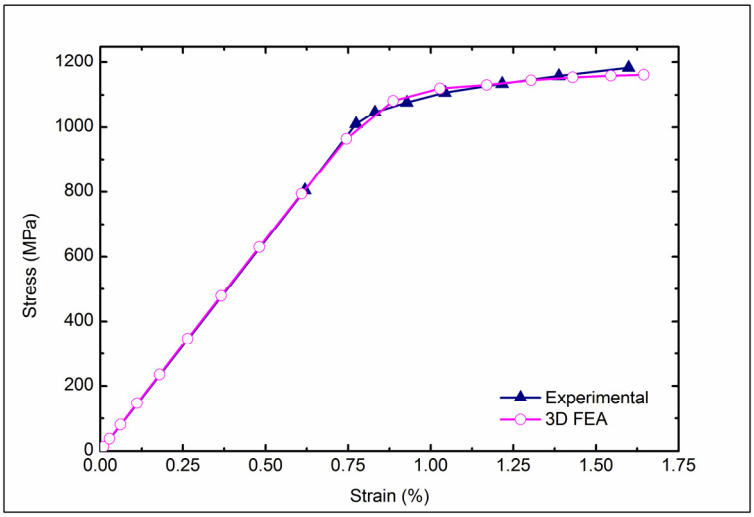

Figure 5.44: Comparison between experimental and 3D FE simulation results for uniaxial loading of extruded Ti-6Al-4V-1B alloy

5.5 Summary

Three-dimensional microstructures of DRA composites and Ti-6Al-4V-1B alloy reconstructed previously using montage serial-sectioning technique were used to

investigate the micromechanical behavior of these materials. Three different powder metallurgy processed DRA samples were considered, with varying matrix to reinforcement particle size ratios of 2.0, 3.1, and 8.1. A two-point correlation functions based methodology was developed to determine the 3D RVE size for the computational models. The microstructures were incorporated in finite element based micromechanical models to investigate the deformation behavior of these materials under uniaxial loading. Quasi-static analyses were carried out using Abaqus/Explicit finite element code. Cracking of SiC particles was found to affect the mechanical properties of DRA composites. A simple Rankine criterion was used to model SiC cracking in these materials. For DRA composites having high matrix to reinforcement particle size ratio, the SiC particles exhibit clustering and the clustering inhibits material densification in the clustered regions. Finite element analyses of 2.0, 3.1, and 8.1 PSR microstructures along with experimental observations suggested that the poorer mechanical response of higher PSR composites is primarily due to the presence of porosity caused by the clustering of SiC particles, rather than the clustering itself. Extruded samples with high PSR value exhibit bands of clustered and particle-free regions and FE analyses suggested that such particle-free regions aid the plastic flow in the matrix. The computed stress-strain curves for all the three DRA samples and the Ti-6Al-4V-1B alloy were found to be in good agreement with the experimental data.

CHAPTER 6

PARAMETRIC STUDIES USING REALISTIC MICROSTRUCTURES

6.1 Introduction

Previous chapters described in detail the incorporation of real microstructures in finite element analyses to study the mechanical response of composite materials. An evident disadvantage of microstructure simulations using real microstructural fields of view is their inability to provide any information on how to improve the properties of a given material. In other words, such simulations based on a real microstructural cutout are useful only for mimicking the mechanical response of a material that already exists. Parametric studies using realistic phase geometries are necessary for real microstructure simulations to be of more useful in material development studies. While it is relatively straight forward to conduct parametric studies using idealized microstructures involving simplistic phase morphologies and isotropic uniform random distribution, it is quite challenging to incorporate the complex morphological and spatial aspects of real material microstructures in such models. Consequently, no such parametric studies have been reported in the literature to the best of author's knowledge. Systematic methodologies for realizing 2D [96-98] and 3D [99] computer simulated microstructures using realistic microstructural feature morphologies, which are statistically similar to real microstructures, have been developed recently by other researchers in author's group at Georgia Tech. Incorporation of these 'virtual' microstructures in the finite element based methodologies developed as part of this research will enable a true "materials by design"

approach for material development. This chapter demonstrates the usefulness of the technique through micromechanical analyses of virtual microstructures of Ti-6Al-4V-1B alloys in 2D and those of DRA composites in 3D. A brief introduction to the methodology for simulating realistic microstructures is given in section 6.1. The following sections describe the micromechanical simulations of such computer simulated 2D and 3D microstructures.

6.2 Computer Simulation and FE Analysis of Realistic Microstructures

The set of spatial (*X, Y, Z*) coordinates of the pixels/voxels comprising a distinct microstructural feature (a particle, whisker, etc.) in a 2D/3D digital microstructure contains complete detailed information on the morphology and geometry of that feature. Once the information on the spatial coordinates of a microstructural feature is captured, an exact replica of that feature can be reproduced at any desired location in the simulation space. Therefore, such sets of (*X, Y, Z*) coordinate points of large number of features (~ few thousands) from representative digital images of a real microstructure can serve as a library of realistic feature images for simulations of the corresponding realistic microstructures. The feature images in the library can be then used to create a desired ensemble of particles/features having any other specified size distribution and volume fraction. Statistical descriptors such as the two-point correlation functions and lineal path probability functions for the simulated microstructure are computed and compared with the experimentally measured functions for the real microstructure. The feature locations in the simulation are changed using Monte-Carlo based techniques till the statistical descriptors for the simulated microstructure are in agreement with that for the corresponding real microstructure. This leads to a realistic simulated microstructure

having realistic complex feature morphologies similar to those in the corresponding real microstructures, and specified size distribution, spatial arrangement, and volume fraction of the microstructural features. Once the simulation model is validated and the model parameters are correlated with processing parameters (such as reinforcement volume fraction, size distribution, and extrusion ratio/temperature), it is possible to generate virtual microstructures of alloys that have been processed differently than those from which the original data sets were obtained. Further details of the methodology are given elsewhere [96, 97, 124].

6.2.1 Two-dimensional Simulations

Figures 6.1a and 6.1b show small sections of the real and simulated 2D microstructures of blind die compacted and extruded pre-alloyed Ti-6Al-4V-1B alloy with the metallographic plane parallel to the extrusion axis. Results given in Figure 6.2 show that there is a good agreement between the two-point correlation functions for the real and the simulated microstructures, demonstrating the statistical similarity of the two microstructures. Though not shown here, other statistical descriptors such as lineal path probability functions of the simulated microstructures were also matched with that of the real microstructure.

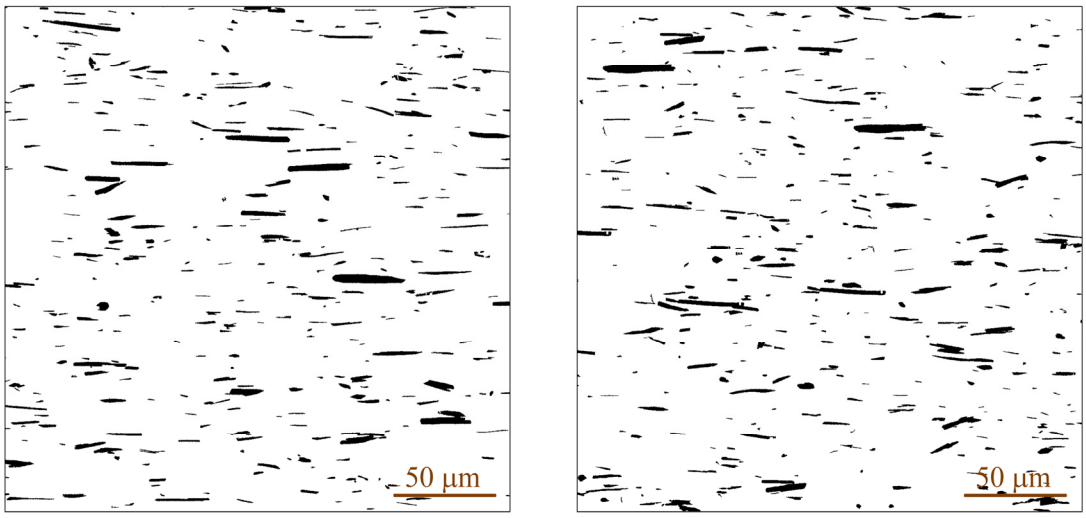

(a) (b)

Figure 6.1: (a) Real and (b) simulated 2D microstructures of blind die compacted and extruded pre-alloyed Ti-6Al-4V-1B alloy

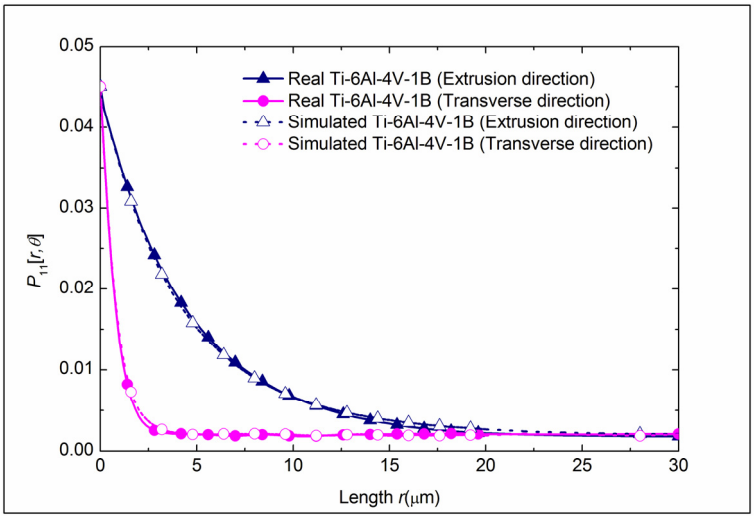

Figure 6.2: Two-point correlation functions for the real and the simulated microstructures of Ti-6Al-4V-1B microstructures shown in Figure 6.1

Uniaxial loading simulation was carried on 500 µm x 500 µm images of the real and simulated microstructures along the extrusion direction. The model specifications

(material constitutive properties, mesh size, boundary conditions, etc.) were the same as those used in the 2D micromechanical simulations detailed in Chapter 4. Figures 6.3 and 6.4 show that the stress/strain distributions in the real and simulated microstructures are in good agreement with each other, demonstrating that the simulated microstructure mimics the micromechanical response of the real microstructure.

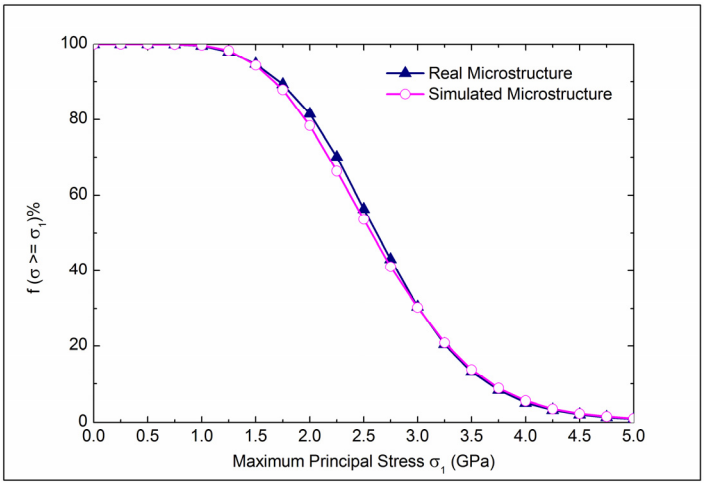

Figure 6.3: Complementary cumulative distribution of maximum principal stress in the SiC particles for real and simulated microstructures of Ti-6Al-4V-1B alloy

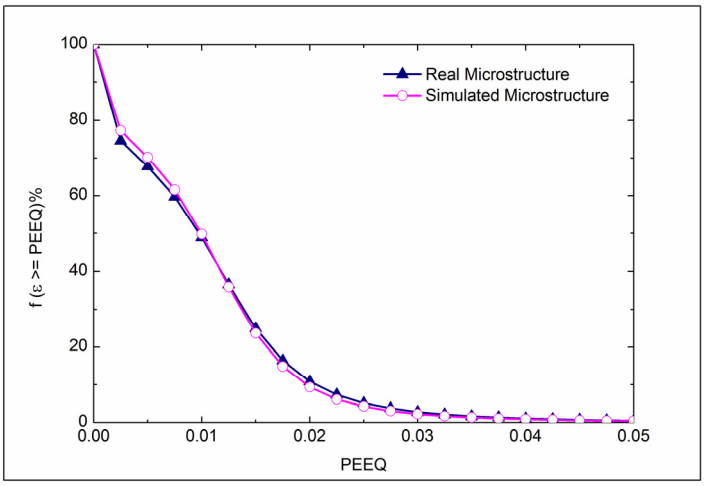

Figure 6.4: Complementary cumulative distribution of equivalent plastic strain in the matrix for real and simulated microstructures of Ti-6Al-4V-1B alloy

The TiB whiskers, having a high aspect ratio, are amenable to rotation during processing such as extrusion and the extent of rotation of the whiskers is dependent on processing parameters such as extrusion temperature and extrusion ratio. Previous research conducted by Dr. Scott Lieberman and Dr. Harpreet Singh has resulted in quantification of the volume fraction, size distribution and spatial arrangements of TiB whiskers in nine different specimens with varying extrusion parameters [122] and the establishment of relationships between extrusion parameters and simulation parameters [124]. These relationships have been utilized to create virtual microstructures of boron modified Ti-alloys with extrusion conditions different than the given real microstructures. Figures 6.5a through 6.5c show three virtual microstructures representing three different processing conditions. Figure 6.5a is the same as figure 6.1b which represents a simulated Ti-6Al-4V-1B microstructure extruded at 1100°C with an extrusion ratio of 16.5:1. Figure 6.5b is a virtual uniform random isotropic microstructure that might have resulted had the material been not extruded after blind die compaction. Similarly, Figure 6.5c shows a virtual microstructure where the TiB whiskers are only partially aligned along the extrusion direction. FE simulations of uniaxial loading along the longitudinal direction were carried on 500 μm x 500 μm images of these virtual microstructures.

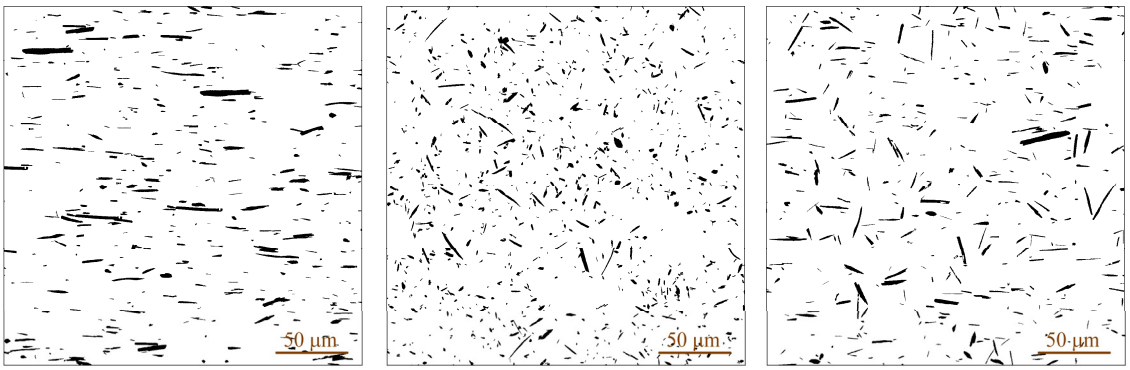

(a) (b) (c)

Figure 6.5: Virtual microstructures of Ti-6Al-4V-1B alloy with (a) aligned (b) randomly oriented and (c) partially aligned TiB whiskers

Figure 6.6 gives the complementary cumulative maximum principal stress distribution in the TiB whiskers for the three microstructures. It is clear from the figure that the TiB whiskers are most effective as a reinforcing phase when aligned parallel to the loading direction.

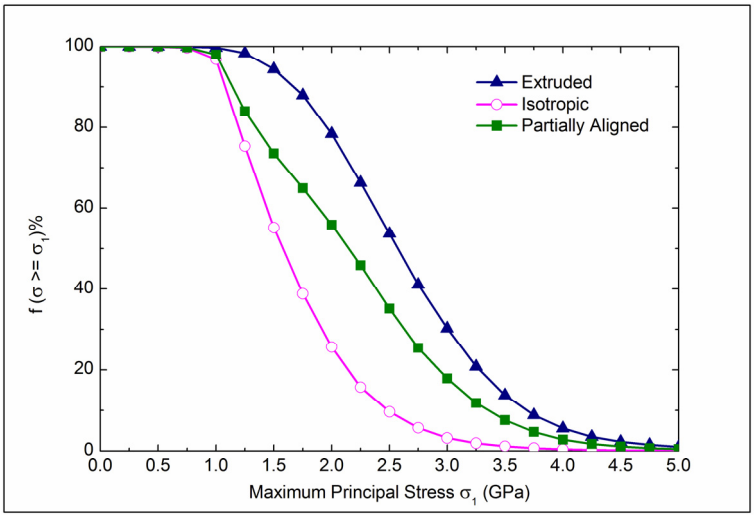

Figure 6.6: Complementary cumulative distribution of maximum principal stress in TiB whiskers for the virtual microstructures shown in Figure 6.5

The complementary cumulative equivalent plastic strain distribution in the titanium matrix for the three microstructures is shown in Figure 6.7. It may be seen that while the matrix deformation is more uniform when the microstructure is isotropic, the extruded microstructure exhibits more localized high strain regions. The matrix flow behavior is further illustrated in Figure 6.8, which shows the contour plots of equivalent plastic strain distribution in the matrix region for approximately the same area in all the three simulated microstructures.

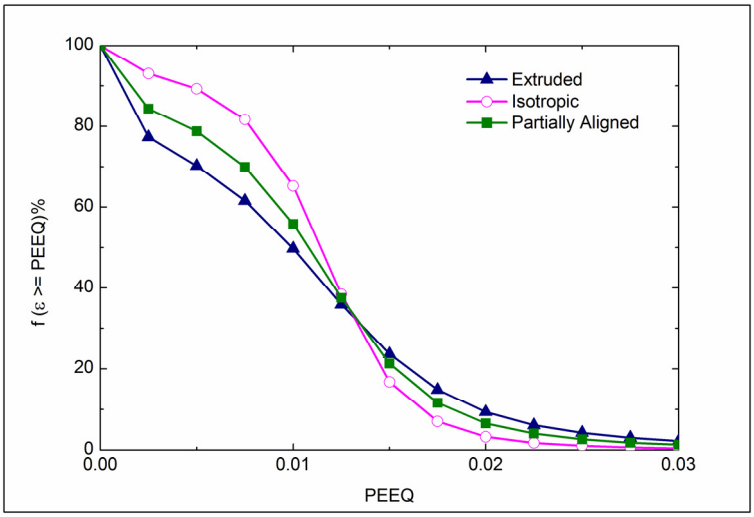

Figure 6.7: Complementary cumulative distribution of equivalent plastic strain in the matrix for the virtual microstructures shown in Figure 6.5

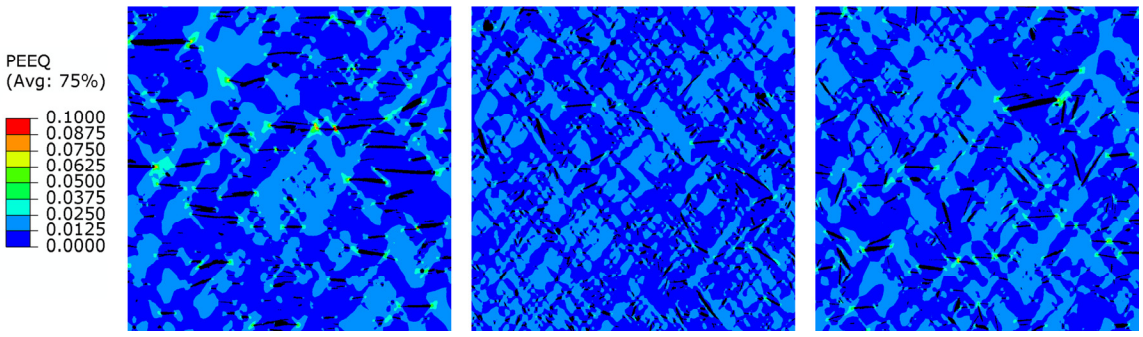

(a) (b) (c)

Figure 6.8: Contour plots of equivalent plastic strain in the matrix for the virtual microstructures of Ti-6Al-4V-1B alloy with (a) aligned (b) randomly oriented and (c) partially aligned TiB whiskers

6.2.2 Three-dimensional Simulations

The methodology for realistic microstructure simulations has been recently extended to 3D space [99]. Figure 6.9 shows a 200 μm x 200 μm x 200 μm volume of simulated microstructure of extruded 2.0 PSR DRA composite containing 28% SiC particles as the reinforcement phase.

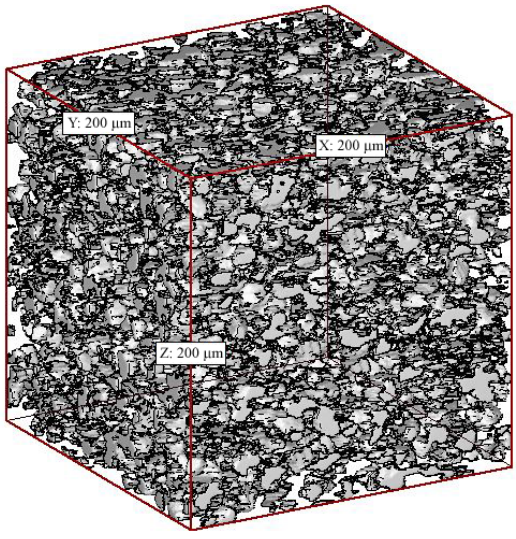

Figure 6.9: Simulated microstructure of extruded 2.0 PSR DRA composite containing 28% SiC particles as the reinforcement phase

Two-point correlation functions along the extrusion and transverse directions (averaged over 20 sections along the thickness direction *Z*) for the real and simulated 2.0 PSR microstructures are given in Figure 6.10, showing the statistical similarity between the two microstructures.

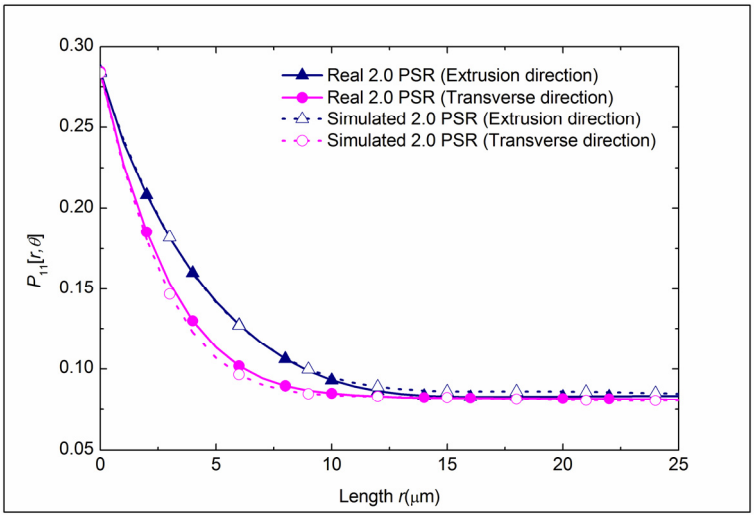

Figure 6.10: Two-point correlation functions for real and simulated microstructural volumes of 2.0 PSR DRA composite

Uniaxial loading simulation of a 400 μm x 200 μm x 100 μm volume of the simulated microstructure along the extrusion direction was carried out and the results were compared with that of a real 2.0 PSR microstructural volume of 400 μm x 200 μm x 100 μm. The material constitutive properties and other model details such as the mesh size and boundary conditions used were the same as those given in the previous chapter. The computed stress-strain curve for the simulated microstructure is in good agreement with that for the real microstructure, as shown in Figure 6.11. Similarly, the stress and strain distributions in the real and simulated microstructures are also in agreement with

each other, as illustrated in Figures 6.12 and 6.13. This shows that the 3D simulation model captures the statistical and micromechanical behavior of the real microstructure.

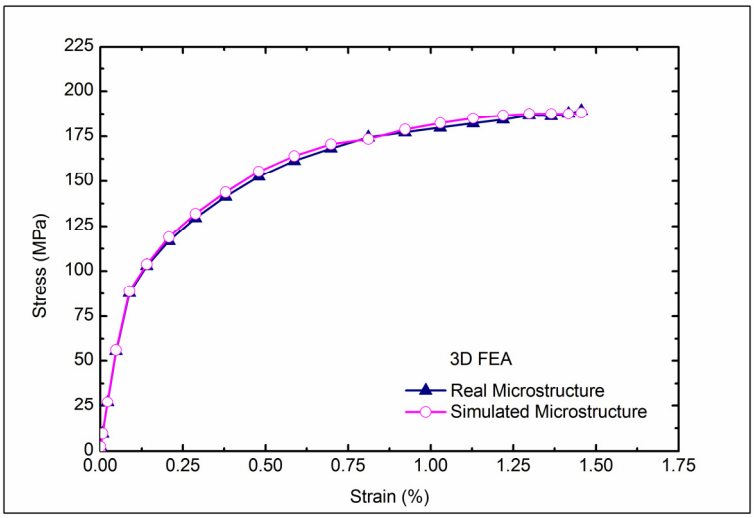

Figure 6.11: Computed stress-strain curves for real and simulated 2.0 PSR DRA microstructural volumes

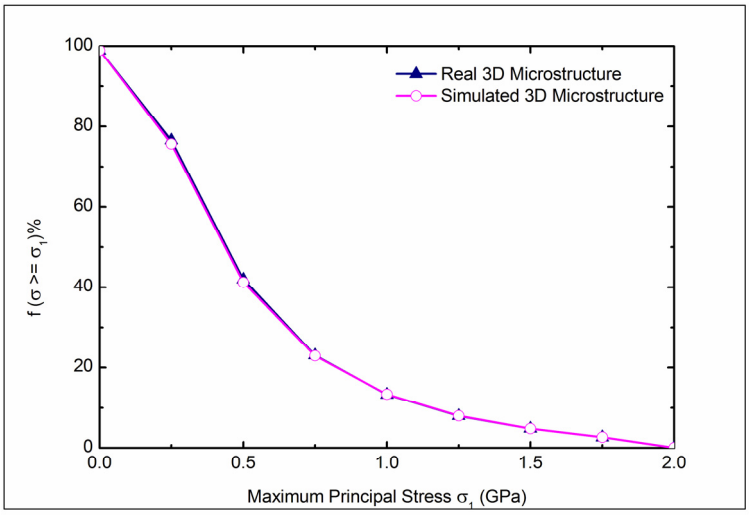

Figure 6.12: Complementary cumulative distribution of maximum principal stress in SiC particles for real and simulated 2.0 PSR DRA microstructural volumes

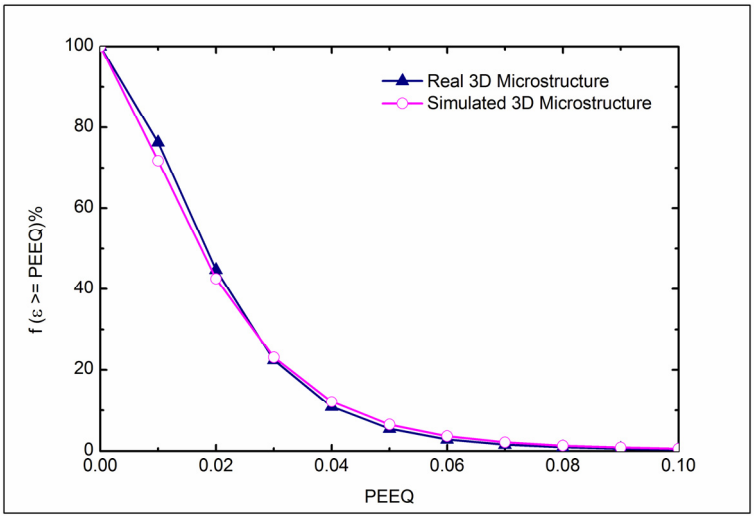

Figure 6.13: Complementary cumulative distribution of maximum principal stress in SiC particles for real and simulated 2.0 PSR DRA microstructural volumes

The simulation parameters can now be varied to create 'virtual' microstructures that may result from changes in the processing parameters. In order to demonstrate this, five different 2.0 PSR microstructures were simulated with varying volume fractions of SiC particles, ranging from 10% to 30% at increments of 5. Figures 6.14a and 6.14b show the simulated volumes containing 10% and 30% SiC, respectively. The simulated volumes were of size 200 μm x 200 μm x 200 μm. The ability to simulate any required volume size is another advantage of such realistic simulation models. For highly heterogeneous microstructures with long-range spatial correlations, one among the current limitations in reconstructing the 3D microstructures is the effort involved in the reconstruction of large amount of volumes (the number of polishing cycles involved in a serial-sectioning procedure, for example). Once a simulation model is validated, it can be used to create microstructural volumes of any size that may be required to be considered a microstructural RVE.

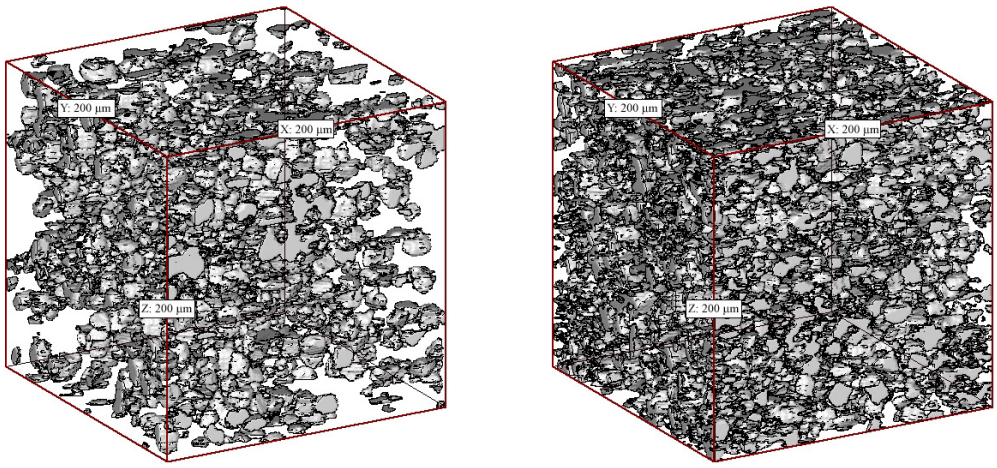

(a) (b)

Figure 6.14: Simulated microstructural volumes of 2.0 PSR DRA composite containing (a) 10% SiC and (b) 30% SiC particles

All the five simulated microstructural volumes were incorporated in finite element models to simulate the micromechanical behavior of these composites. Figures 6.15a through 6.15e show the FE mesh for the five different volumes.

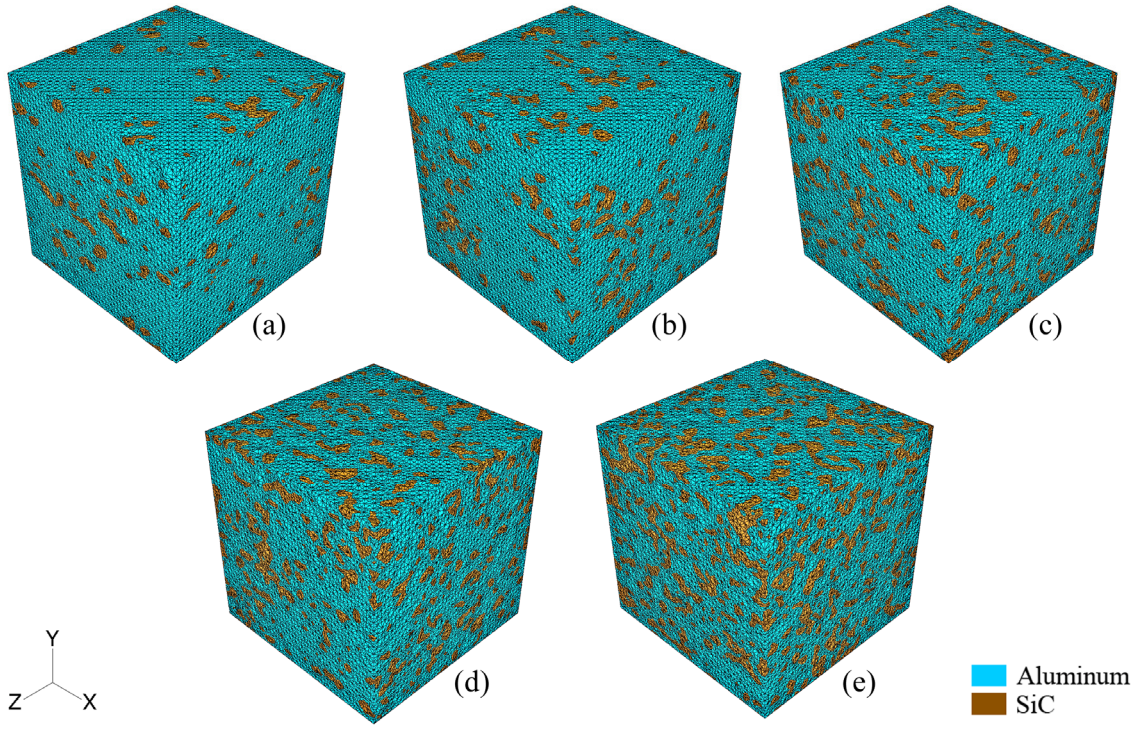

Figure 6.15: FE mesh for simulated microstructural volumes containing (a) 10% (b) 15% (c) 20% (d) 25% and (e) 30% SiC particles

The computed stress-strain curves for uniaxial loading along the extrusion direction for all the models are illustrated in Figure 6.16. Figure 6.17 shows the contour plot of maximum principal stress in the SiC particles for the composite containing 30% SiC particles. The Young's modulus and 0.2% yield strength values for the five models are given in Table 6.1. As expected, the modulus and yield strength values of the composite increases with increase in SiC particulate volume fraction. Higher matrix strain-hardening is observed initially for composites with higher SiC volume fraction because of localized high strain regions but the strain-hardening rate approaches that of the unreinforced matrix when strains are in the regime of fully developed plastic flow.

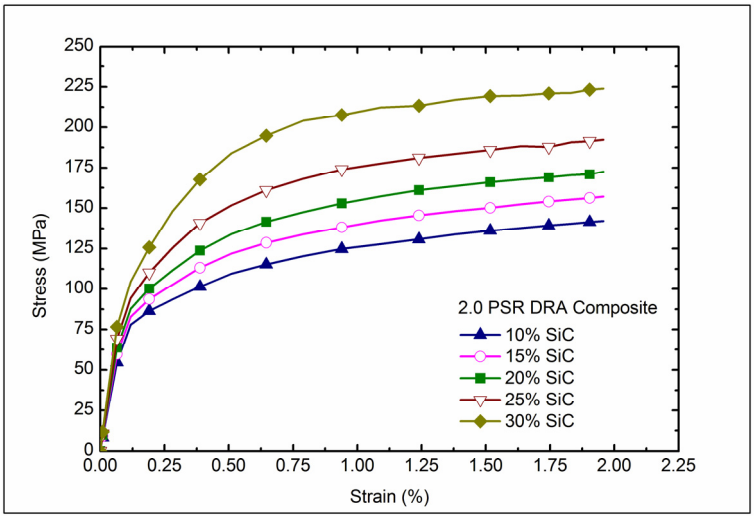

Figure 6.16: Computed stress-strain curves for the simulated microstructural volumes shown in Figure 6.15

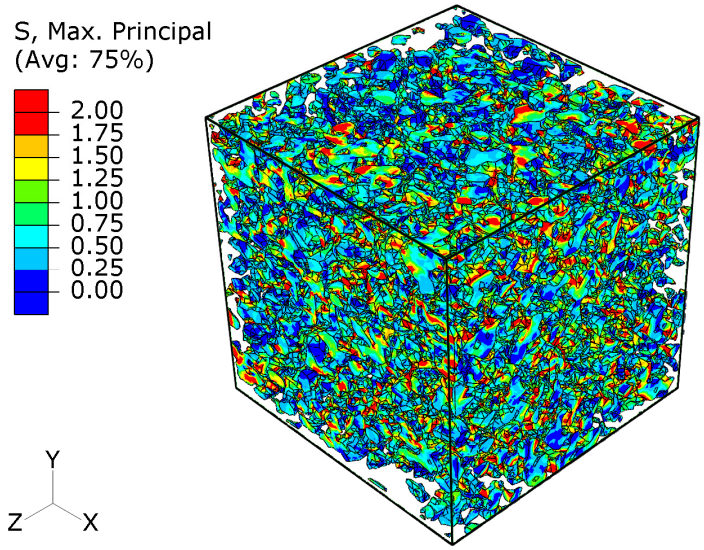

Figure 6.17: Contour plot of maximum principal stress (GPa) in SiC particles for the composite containing 30% SiC particles

Table 6.1: Computed modulus and yield strength values from 3D FE simulations of virtual microstructures with varying SiC volume fractions

V_f (SiC) %	Elastic Modulus (GPa)	Yield Strength (Mpa)
10	87	90
15	95	98
20	102	107
25	111	118
30	124	140

6.3 Summary

A novel simulation-based materials design methodology for two-phase heterogeneous materials was demonstrated. Simulation models incorporating realistic phase morphologies and/or spatial distributions of the reinforcement phase have been developed by colleagues at Georgia Tech. Statistical similarity of the simulated microstructures with the corresponding real microstructures is guaranteed by matching statistical descriptors such as two-point correlation and lineal-path probability functions. The 2D and 3D simulated microstructures were analyzed for micromechanical response using finite element based techniques developed as a part of this research and were compared with that of the corresponding real microstructures. The simulated microstructures are shown to have a micromechanical response similar to the corresponding real microstructures. Parameters in the simulation model were varied to create 'virtual' microstructures that represent changes in the processing parameters of these materials. These virtual microstructures were incorporated in finite element models to predict their macroscopic behavior. Such parametric studies are shown to provide useful input for materials design.

CHAPTER 7

CONCLUSIONS

7.1 Summary and Significant Results

Micromechanical behavior of two-phase heterogeneous materials having anisotropic non-uniform microstructures exhibiting long-range spatial distributions of the order of few hundreds of microns was investigated as part of this research. Two materials systems were considered: DRA composites containing SiC particles as reinforcement and boron modified titanium alloys containing *in situ* formed TiB whiskers. The material samples used in this research were produced via powder metallurgy route which were subsequently compacted and extruded. Three distinct DRA samples were considered, each with a different matrix to reinforcement particle size ratio. Most of the reported work on predictive models for such composite materials have been limited to using uniform random isotropic microstructures and poorly assumed constitutive properties of individual phases. This research involved use of instrumented indentation, stereological techniques, image analysis, statistical descriptors, and finite element based modeling tools for more realistic and accurate predictions of the mechanical response of these materials.

Microindentation technique was employed to deduce the constitutive properties of different microstructural phases under investigation in this study. Spherical indentation with high penetration depth to indenter radius ratio along with finite element based reverse analysis was used to determine the elastic-plastic constitutive properties of Ti-6Al-4V matrix in Ti-6Al-4V-1B alloy and Al-6061 matrix in DRA composites. Effect of

indenter tip geometry and friction between the indenter and the specimen on the load-displacement curve was looked into. Small additions of boron to titanium alloys were found to alter the microstructure, and thereby the constitutive properties, of the matrix. The spherical indentation response of the Ti-6Al-4V matrix region was shown to be different from that of an unreinforced alloy of similar composition and processing. Elastic modulus of the TiB whiskers was estimated using Oliver-Pharr method from the load-displacement curve obtained using Vickers pyramidal indenter.

Large area high resolution montage images captured using optical microscope were used for 2D plane-stress micromechanical studies. Two-point correlation functions were employed to arrive at a statistically representative volume element for the microstructures under investigation. Real microstructures of DRA composites and Ti-6Al-4V-1B alloy were incorporated in finite element based uniaxial loading simulation of these materials. Material constitutive properties deduced using microindentation were used to model the deformation behavior of individual microstructural phases. Effect of mesh density and boundary conditions on the mechanical response of the FE models was investigated in detail. It was observed that while the 2D FE simulations were sensitive to the anisotropy of the microstructures as well as first order microstructural properties such as volume fraction of the reinforcement phase, the spatial arrangement of the reinforcement phase did not significantly affect the computed macroscopic response. Comparison with experimental tensile test data revealed that the 2D analyses underestimate the yield stress of the composite material in all cases. While qualitative observations may be made using 2D plane-stress simulations of discontinuously

reinforced composites, the usefulness of such simulations for quantitative information was found to be limited.

Three-dimensional microstructures previously reconstructed using montage serial sectioning technique were used in this research for realistic 3D micromechanical modeling. A two-point correlation functions based methodology was developed to determine the 3D RVE size for the computational models. The 3D microstructures were incorporated in finite element models preserving the complex geometry and spatial distribution of the real microstructures. Observation of failed samples of DRA composites showed evidence of brittle cracking of the SiC particles. A simple Rankine criterion was used to model SiC cracking in these materials. For DRA composites with high PSR values, the SiC particles exhibit clustering and the clustering inhibits material densification in the clustered regions. Finite element analyses of 2.0, 3.1, and 8.1 PSR microstructures along with experimental observations suggested that the poorer mechanical response of higher PSR composites is primarily due to the presence of porosity caused by the clustering of SiC particles, rather than the clustering itself. Extruded samples with high PSR value exhibit bands of clustered and particle-free regions and FE analyses suggested that such particle-free regions aid the plastic flow in the matrix. The computed stress-strain curves for all the three DRA samples and the Ti-6Al-4V-1B alloy were found to be in good agreement with the experimental data.

Finite element based parametric studies were carried out on realistic virtual microstructures created using simulation models developed by colleagues at Georgia Tech. By correlating the simulation parameters with process parameters, it was demonstrated that such parametric studies provide useful input for materials design.

7.2 Recommendations for Future Research

As with any other model, the simulation models outlined in this research are approximations of naturally occurring physical phenomena and can always be made better and more realistic. Through the course of this research, potential areas were identified as requiring further investigation.

7.2.1 Damage Initiation, Accumulation, and Failure

Current research focused on the deformation behavior of discontinuously reinforced composite materials under small strains (less than 2%). 3D simulations revealed that damage mechanisms such as brittle cracking of the reinforcement phase and the amount of porosity present in the material need to be incorporated in the models in order to match the experimental results. Though the simulation results were in good agreement with the experimental data with the addition of a simplified brittle cracking constitutive behavior for the SiC particles and element removal from the FE mesh where porosity is present, further refinement of the model is required for simulating damage initiation and growth leading to failure in these materials. This is non-trivial, requiring extensive experimental studies and coupling of deformation mechanisms in the matrix and the reinforcement phases. Observation of failed samples has shown evidence of pore growth in DRA composites with high PSR values, which was not considered in this research. Crystal plasticity-based constitutive models may also need to be included when modeling damage initiation and growth.

7.2.2 Indentation Modeling with Realistic 3D Microstructures

Microindentation using spherical tip coupled with FE simulation of the indentation process was shown as a viable technique for determining the constitutive

properties of small microstructural volumes earlier in this thesis. The procedure may be extended to deduce the global constitutive properties of multi-phase materials. This requires modeling of the indentation process in 3D with realistic 3D microstructural volumes as opposed to 2D axisymmetric modeling employed for individual phases. Preliminary studies have been carried out and Figure 7.1 shows the FE model for spherical indentation of a DRA composite containing 20% SiC particles.

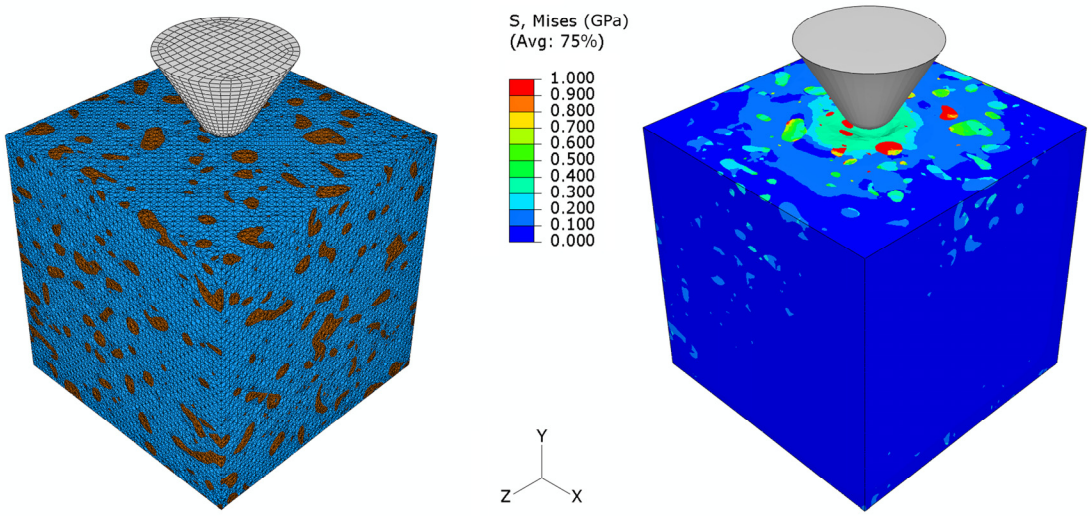

Figure 7.1: FE model for spherical indentation of a DRA composite containing 20% SiC particles

Localized large deformations experienced during indentation process can lead to decohesion at the matrix/particle interface which was not considered in above shown model. It is also of interest to investigate how the inclusions in a material affect the load-displacement curve. This may depend on a number of factors such as the ratio of average inclusion size to indenter tip radius, penetration depth, and volume fraction of the inclusions along with the vicinity of the inclusions to the indented region.

REFERENCES

[1] J. D. Eshelby, "The Determination of the Elastic Field of an Ellipsoidal Inclusion, and Related Problems," *Proceedings of the Royal Society of London Series a-Mathematical and Physical Sciences,* vol. 241, pp. 376-396, 1957.

[2] J. Qu and M. Cherkaoui, *Fundamentals of micromechanics of solids*. Hoboken, N.J.: Wiley, 2006.

[3] S. Schmauder, "Computational mechanics," *Annual Review of Materials Research,* vol. 32, p. 437, 2002.

[4] D. Raabe, "Challenges in computational materials science," *Advanced Materials,* vol. 14, p. 639, 2002.

[5] L. Mishnaevsky Jr and S. Schmauder, "Continuum mesomechanical finite element modeling in materials development: A state-of-the-art review," *Applied Mechanics Reviews,* vol. 54, p. 49, 2001.

[6] A. Needleman, "Computational mechanics at the mesoscale," *Acta Materialia,* vol. 48, p. 105, 2000.

[7] A. M. Gokhale and S. Yang, "Application of image processing for simulation of mechanical response of multi-length scale microstructures of engineering alloys," *Metallurgical and Materials Transactions A: Physical Metallurgy and Materials Science,* vol. 30, p. 2369, 1999.

[8] J. Fish and K. Shek, "Multiscale analysis of composite materials and structures," *Composites Science and Technology,* vol. 60, p. 2547, 2000.

[9] F. G. Rammerstorfer, A. F. Plankensteiner, F. D. Fischer, and T. Antretter, "Hierarchical models for simulating the mechanical behavior of heterogeneous materials: An approach to high speed tool steel," *Materials Science & Engineering A: Structural Materials: Properties, Microstructure and Processing,* vol. A259, p. 73, 1999.

[10] A. Zaoui, "Continuum micromechanics: Survey," *Journal of Engineering Mechanics,* vol. 128, p. 808, 2002.

[11] T. Mura, *Micromechanics of defects in solids*, 2nd, rev. ed. Dordrecht, Netherlands: Kluwer Academic Publishers, 1987.

[12] R. Hill, "The elastic behaviour of a crystalline aggregate," *Proceedings of the Physical Society. Section A,* vol. 65, p. 354, 1952.

[13] R. Hill, "Elastic Properties of Reinforced Solids - Some Theoretical Principles," *Journal of the Mechanics and Physics of Solids,* vol. 11, pp. 357-372, 1963.

[14] S. Nemat-Nasser and M. Hori, *Micromechanics : overall properties of heterogeneous materials*, 2nd rev. ed. Amsterdam: Elsevier, 1999.

[15] E. Sanchez-Palencia, *Non-homogenous media and vibration theory*. Berlin ; New York: Springer-Verlag, 1980.

[16] W. J. Drugan and J. R. Willis, "Micromechanics-based nonlocal constitutive equation and estimates of representative volume element size for elastic composites," *Journal of the Mechanics and Physics of Solids,* vol. 44, p. 497, 1996.

[17] Z. Shan and A. M. Gokhale, "Representative volume element for non-uniform micro-structure," *Computational Materials Science,* vol. 24, p. 361, 2002.

[18] T. Kanit, S. Forest, I. Galliet, V. Mounoury, and D. Jeulin, "Determination of the size of the representative volume element for random composites: statistical and numerical approach," *International Journal of Solids and Structures,* vol. 40, pp. 3647-3679, Jun-Jul 2003.

[19] J. Zeman and M. Sejnoha, "From random microstructures to representative volume elements," *Modelling and Simulation in Materials Science and Engineering,* vol. 15, pp. S325-S335, Jun 2007.

[20] D. F. Adams, "Inelastic analysis of a unidirectional composite subjected to transverse normal loading," *Journal of Composite Materials,* vol. 4, p. 310, 1970.

[21] J. R. Brockenbrough, S. Suresh, and H. A. Wienecke, "Deformation of metal-matrix composites with continuous fibers. Geometrical effects of fiber distribution and shape," *Acta Metallurgica et Materialia,* vol. 39, p. 735, 1991.

[22] S. Jansson, "Homogenized nonlinear constitutive properties and local stress concentrations for composites with periodic internal structure," *International Journal of Solids and Structures,* vol. 29, p. 2181, 1992.

[23] D. B. Zahl, S. Schmauder, and R. M. McMeeking, "Transverse strength of metal matrix composites reinforced with strongly bonded continuous fibers in regular arrangements," *Acta Metallurgica et Materialia,* vol. 42, p. 2983, 1994.

[24] G. Bao, J. W. Hutchinson, and R. M. McMeeking, "Particle reinforcement of ductile matrices against plastic flow and creep," *Acta Metallurgica et Materialia,* vol. 39, p. 1871, 1991.

[25] D. Fang, H. Qi, and S. Tu, "Elastic and plastic properties of metal-matrix composites: geometrical effects of particles," *Computational Materials Science,* vol. 6, p. 303, 1996.

[26] Z. Li, S. Schmauder, A. Wanner, and M. Dong, "Expressions to characterize the flow behavior of particle-reinforced composites based on axisymmetric unit cell models," *Scripta Metallurgica et Materialia,* vol. 33, p. 1289, 1995.

[27] S. Qin, C. Chen, G. Zhang, W. Wang, and Z. Wang, "Effect of particle shape on ductility of SiCp reinforced 6061 Al matrix composites," *Materials Science and Engineering A: Structural Materials: Properties, Microstructure and Processing,* vol. 272, p. 363, 1999.

[28] M. Sautter, C. Dietrich, M. H. Poech, S. Schmauder, and H. F. Fischmeister, "Finite element modelling of a transverse-loaded fibre composite. Effects of section size and net density," *Computational Materials Science,* vol. 1, p. 225, 1993.

[29] M. Dong and S. Schmauder, "Modeling of metal matrix composites by a self-consistent embedded cell model," *Acta Materialia,* vol. 44, p. 2465, 1996.

[30] L. Farrissey, S. Schmauder, M. Dong, E. Soppa, M. H. Poech, and P. McHugh, "Investigation of the strengthening of particulate reinforced composites using different analytical and finite element models," *Computational Materials Science,* vol. 15, p. 1, 1999.

[31] M. H. Poech, "Deformation of two-phase materials. Application of analytical elastic solutions to plasticity," *Scripta Metallurgica et Materialia,* vol. 27, p. 1027, 1992.

[32] G. Bao, "Damage due to fracture of brittle reinforcements in a ductile matrix," *Acta Metallurgica et Materialia,* vol. 40, p. 2547, 1992.

[33] O. van der Sluis, P. J. G. Schreurs, W. A. M. Brekelmans, and H. E. H. Meijer, "Overall behaviour of heterogeneous elastoviscoplastic materials: Effect of microstructural modelling," *Mechanics of Materials,* vol. 32, p. 449, 2000.

[34] V. Kouznetsova, W. A. M. Brekelmans, and F. P. T. Baaijens, "Approach to micro-macro modeling of heterogeneous materials," *Computational Mechanics,* vol. 27, p. 37, 2001.

[35] C. R. Chen, S. Y. Qin, S. X. Li, and J. L. Wen, "Finite element analysis about effects of particle morphology on mechanical response of composites," *Materials Science and Engineering A: Structural Materials: Properties, Microstructure and Processing,* vol. 278, p. 96, 2000.

[36] A. Borbely and H. Biermann, "Finite element investigation of the effect of particle distribution on the uniaxial stress-strain behavior of particulate-reinforced metal-matrix composites," *Advanced Engineering Materials,* vol. 2, p. 366, 2000.

[37] J. Segurado, C. Gonzalez, and J. Llorca, "A numerical investigation of the effect of particle clustering on the mechanical properties of composites," *Acta Materialia,* vol. 51, p. 2355, 2003.

[38] L. L. Mishnaevsky Jr, "Three-dimensional numerical testing of microstructures of particle reinforced composites," *Acta Materialia,* vol. 52, p. 4177, 2004.

[39] H. Shen and C. J. Lissenden, "3D finite element analysis of particle-reinforced aluminum," *Materials Science and Engineering A,* vol. 338, p. 271, 2002.

[40] V. V. Bhanu Prasad, B. V. R. Bhat, Y. R. Mahajan, and P. Ramakrishnan, "Structure-property correlation in discontinuously reinforced aluminium matrix composites as a function of relative particle size ratio," *Materials Science and Engineering A,* vol. 337, p. 179, 2002.

[41] S.-J. Hong, H.-M. Kim, D. Huh, B. S. Chun, and C. Suryanarayana, "Effect of clustering on the mechanical properties of SiC particulate-reinforced aluminum alloy 2024 metal matrix composites," *Materials Science and Engineering A,* vol. 347, p. 198, 2003.

[42] J. E. Spowart and D. B. Miracle, "The influence of reinforcement morphology on the tensile response of 6061/SiC/25p discontinuously-reinforced aluminum," *Materials Science and Engineering a-Structural Materials Properties Microstructure and Processing,* vol. 357, pp. 111-123, Sep 25 2003.

[43] J. Y. Pastor, J. Llorca, P. Poza, I. de Francisco, R. I. Merino, and J. I. Pena, "Mechanical properties of melt-grown Al2O3-ZrO2(Y2O3) eutectics with different microstructure," *Journal of the European Ceramic Society,* vol. 25, pp. 1215-1223, 2005.

[44] H. Fischmeister, J. O. Hjalmered, B. Karlsson, G. Linden, and B. Sundstrom, "Plastic deformation of two-phase materials with coarse microstructure," *Institute of Metals (London), Monograph and Report Series,* vol. 1, p. 621, 1973.

[45] M. H. Poech, H. F. Fischmeister, D. Kaute, and R. Spiegler, "FE-modelling of the deformation behaviour of WC-Co alloys," *Computational Materials Science,* vol. 1, p. 213, 1993.

[46] C. Dietrich, M. H. Poech, H. F. Fischmeister, and S. Schmauder, "Stress and strain partitioning in a Ag-Ni fibre composite under transverse loading. Finite element modelling and experimental study," *Computational Materials Science,* vol. 1, p. 195, 1993.

[47] J. R. Brockenbrough, W. H. Hunt, Jr., and O. Richmond, "Reinforced material model using actual microstructural geometry," *Scripta Metallurgica et Materialia,* vol. 27, p. 385, 1992.
[48] S. Ghosh, K. Lee, and S. Moorthy, "Multiple scale analysis of heterogeneous elastic structures using homogenization theory and Voronoi cell finite element method," *International Journal of Solids and Structures,* vol. 32, p. 27, 1995.
[49] S. Ghosh, Z. Nowak, and K. Lee, "Quantitative characterization and modeling of composite microstructures by Voronoi cells," *Acta Materialia,* vol. 45, p. 2215, 1997.
[50] S. Ghosh, Z. Nowak, and K. Lee, "Tessellation-based computational methods for the characterization and analysis of heterogeneous microstructures," *Composites Science and Technology,* vol. 57, p. 1187, 1997.
[51] T. Steinkopff and M. Sautter, "Simulating the elasto-plastic behavior of multiphase materials by advanced finite element techniques part I: a rezoning technique and the multiphase element method," *Computational Materials Science,* vol. 4, p. 10, 1995.
[52] T. Steinkopff and M. Sautter, "Simulating the elasto-plastic behavior of multiphase materials by advanced finite element techniques part II: simulation of the deformation behavior of Ag-Ni composites," *Computational Materials Science,* vol. 4, p. 15, 1995.
[53] J. Wulf, T. Steinkopff, and H. F. Fischmeister, "Fe-simulation of crack paths in the real microstructure of an Al(6061)/SiC composite," *Acta Materialia,* vol. 44, p. 1765, 1996.
[54] Mishnaevsky, Jr., N. Lippmann, and S. Schmauder, "Computational modeling of crack propagation in real microstructures of steels and virtual testing of artificially designed materials," *International Journal of Fracture,* vol. 120, p. 581, 2003.
[55] S. J. Hollister and N. Kikuchi, "Homogenization theory and digital imaging: a basis for studying the mechanics and design principles of bone tissue," *Biotechnology and Bioengineering,* vol. 43, p. 586, 1994.
[56] K. Terada, T. Miura, and N. Kikuchi, "Digital image-based modeling applied to the homogenization analysis of composite materials," *Computational Mechanics,* vol. 20, p. 331, 1997.
[57] Z. Q. Yue, S. Chen, and L. G. Tham, "Finite element modeling of geomaterials using digital image processing," *Computers and Geotechnics,* vol. 30, p. 375, 2003.
[58] P. Louis and A. M. Gokhale, "Application of image analysis for characterization of spatial arrangements of features in microstructure," *Metallurgical and Materials Transactions A: Physical Metallurgy and Materials Science,* vol. 26A, p. 1449, 1995.
[59] Z. Shan and A. M. Gokhale, "Micromechanics of complex three-dimensional microstructures," *Acta Materialia,* vol. 49, p. 2001, 2001.
[60] Z. Shan and A. M. Gokhale, "Digital image analysis and microstructure modeling tools for microstructure sensitive design of materials," *International Journal of Plasticity,* vol. 20, p. 1347, 2004.
[61] N. Chawla, V. V. Ganesh, and B. Wunsch, "Three-dimensional (3D) microstructure visualization and finite element modeling of the mechanical

behavior of SiC particle reinforced aluminum composites," *Scripta Materialia,* vol. 51, p. 161, 2004.

[62] G. Geandier, A. Hazotte, S. Denis, A. Mocellin, and E. Maire, "Microstructural analysis of alumina chromium composites by X-ray tomography and 3-D finite element simulation of thermal stresses," *Scripta Materialia,* vol. 48, p. 1219, 2003.

[63] S. A. Langer, Fuller E.R, Jr., and W. C. Carter, "OOF: An image-based finite-element analysis of material microstructures," *Computing in Science and Engineering,* vol. 3, p. 15, 2001.

[64] S. A. Langer, A. Reid, S.-I. Haan, and R. E. Garcia, "The OOF2 Manual," *http://www.ctcms.nist.gov/oof/oof2man/index.html*, 2005.

[65] A. Saigal, E. R. Fuller, Jr., S. A. Langer, W. C. Carter, M. H. Zimmerman, and K. T. Faber, "Effect of interface properties on microcracking of iron titanate," *Scripta Materialia,* vol. 38, p. 1449, 1998.

[66] C. H. Hsueh, P. F. Becher, E. R. Fuller, Jr., S. A. Langer, and W. C. Carter, "Surface-roughness induced residual stresses in thermal barrier coatings: computer simulations," *Materials Science Forum,* vol. 308-311, p. 442, 1999.

[67] A. Saigal, E. R. Fuller Jr, and S. Jahanmir, "Modeling of residual stresses and mechanical behavior of glass-infiltrated spinel ceramic composites," San Diego, CA, United States, 2001, p. 643.

[68] A. Saigal and Fuller E.R, Jr., "Analysis of stresses in aluminum-silicon alloys," *Computational Materials Science,* vol. 21, p. 149, 2001.

[69] A. Zimmermann, W. C. Carter, and E. R. Fuller, Jr., "Damage evolution during microcracking of brittle solids," *Acta Materialia,* vol. 49, p. 127, 2001.

[70] N. Chawla, B. V. Patel, M. Koopman, K. K. Chawla, R. Saha, B. R. Patterson, E. R. Fuller, and S. A. Langer, "Microstructure-based simulation of thermomechanical behavior of composite materials by object-oriented finite element analysis," *Materials Characterization,* vol. 49, p. 395, 2002.

[71] A. R. Boccaccini, J. L. Spino, and V. Cannillo, "Hermetic glass bodies with controlled porosity: Processing and properties," Cocoa Beach, FL, United States, 2002, p. 191.

[72] V. Cannillo, C. Leonelli, T. Manfredini, M. Montorsi, and A. R. Boccaccini, "Computational Simulations for the Assessment of the Mechanical Properties of Glass with Controlled Porosity," *Journal of Porous Materials,* vol. 10, p. 189, 2003.

[73] M. Bartsch, U. Schulz, J.-M. Dorvaux, O. Lavigne, E. R. Fuller Jr, and S. A. Langer, "Simulating thermal response of EB-PVD thermal barrier coating microstructures," Cocoa Beach, FL, United States, 2003, p. 549.

[74] Z. Wang, A. Kulkarni, S. Deshpande, T. Nakamura, and H. Herman, "Effects of pores and interfaces on effective properties of plasma sprayed zirconia coatings," *Acta Materialia,* vol. 51, p. 5319, 2003.

[75] E. J. Minay, A. R. Boccaccini, P. Veronesi, V. Cannillo, and C. Leonelli, "Processing of novel glass matrix composites by microwave heating," *Journal of Materials Processing Technology,* vol. 155-156, p. 1749, 2004.

[76] A. R. Boccaccini, V. Cannillo, C. Leonelli, and P. Veronesi, "Porous glasses with controlled porosity: Processing and modelling of mechanical properties," Istanbul, Turkey, 2004, p. 2243.
[77] R. E. Garcia, Y.-M. Chiang, W. C. Carter, P. Limthongkul, and C. M. Bishop, "Microstructural modeling and design of rechargeable lithium-ion batteries," *Journal of the Electrochemical Society,* vol. 152, pp. 255-263, 2005.
[78] M. G. D. V. Cuppari, R. M. Souza, and A. Sinatora, "Effect of hard second phase on cavitation erosion of Fe-Cr-Ni-C alloys," *Wear,* vol. 258, p. 596, 2005.
[79] A. L. Geiger and J. A. Walker, "The Processing and Properties of Discontinuously Reinforced Aluminum Composites," *Jom-Journal of the Minerals Metals & Materials Society,* vol. 43, pp. 8-15, Aug 1991.
[80] A. Slipenyuk, V. Kuprin, Y. Milman, J. E. Spowart, and D. B. Miracle, "The effect of matrix to reinforcement particle size ratio (PSR) on the microstructure and mechanical properties of a P/M processed AlCuMn/SiCp MMC," *Materials Science and Engineering A-Structural Materials Properties Microstructure and Processing,* vol. 381, pp. 165-170, Sep 15 2004.
[81] A. Isalak, *Ferrous Powder Metallurgy*. Cambridge: Cambridge International Science Publishing, 1997.
[82] R. R. Fard and F. Akhlaghi, "Effect of extrusion temperature on the microstructure and porosity of A356-SiCp composites," *Journal of Materials Processing Technology,* vol. 187, pp. 433-436, Jun 12 2007.
[83] V. V. B. Prasad, B. V. R. Bhat, Y. R. Mahajan, and P. Ramakrishnan, "Effect of extrusion parameters on structure and properties of 2124 aluminum alloy matrix composites," *Materials and Manufacturing Processes,* vol. 16, pp. 841-853, 2001.
[84] T. B. Massalski, "Binary Alloy Phase Diagrams," 2nd ed: ASM International, 1990, p. 547.
[85] C. Schuh and D. C. Dunand, "Whisker alignment of Ti-6Al-4V/TiB composites during deformation by transformation superplasticity," *International Journal of Plasticity,* vol. 17, pp. 317-340, 2001.
[86] S. Tamirisakandala, B. V. Vedam, and R. B. Bhat, "Recent advances in the deformation processing of titanium alloys," *Journal of Materials Engineering and Performance,* vol. 12, pp. 661-673, Dec 2003.
[87] S. Tamirisakandala, R. B. Bhat, V. A. Ravi, and D. B. Miracle, "Powder metallurgy Ti-6Al-4V-xB alloys: Processing, microstructure, and properties," *Jom,* vol. 56, pp. 60-63, May 2004.
[88] S. Tamirisakandala, R. B. Bhat, J. S. Tiley, and D. B. Miracle, "Grain refinement of cast titanium alloys via trace boron addition," *Scripta Materialia,* vol. 53, pp. 1421-1426, Dec 2005.
[89] S. Torquato, "Statistical description of microstructures," *Annual Review of Materials Research,* vol. 32, pp. 77-111, 2002.
[90] A. Tewari and A. M. Gokhale, "Nearest-neighbor distances between particles of finite size in three-dimensional uniform random microstructures," *Materials Science and Engineering a-Structural Materials Properties Microstructure and Processing,* vol. 385, pp. 332-341, Nov 15 2004.
[91] A. Tewari, A. M. Gokhale, J. E. Spowart, and D. B. Miracle, "Quantitative characterization of spatial clustering in three-dimensional microstructures using

two-point correlation functions," *Acta Materialia,* vol. 52, pp. 307-319, Jan 19 2004.

[92] P. B. Corson, "Correlation-Functions for Predicting Properties of Heterogeneous Materials .1. Experimental Measurement of Spatial Correlation-Functions in Multiphase Solids," *Journal of Applied Physics,* vol. 45, pp. 3159-3164, 1974.

[93] Y. Bhandari, S. Sarkar, M. Groeber, M. D. Uchic, D. M. Dimiduk, and S. Ghosh, "3D polycrystalline microstructure reconstruction from FIB generated serial sections for FE analysis," *Computational Materials Science,* vol. 41, pp. 222-235, Dec 2007.

[94] H. Singh and A. M. Gokhale, "Visualization of three-dimensional microstructures," *Materials Characterization,* vol. 54, pp. 21-29, Jan 2005.

[95] S. I. Lieberman, A. M. Gokhale, and S. Tamirisakandala, "Reconstruction of three-dimensional microstructures of TiB whiskers in powder processed Ti-6Al-4V-1B alloys," *Materials Characterization,* vol. 58, pp. 527-533, Jun 2007.

[96] H. Singh, A. M. Gokhale, Y. Mao, and J. E. Spowart, "Computer simulations of realistic microstructures of discontinuously reinforced aluminum alloy (DRA) composites," *Acta Materialia,* vol. 54, pp. 2131-2143, May 2006.

[97] H. Singh, Y. Mao, A. Sreeranganathan, and A. M. Gokhale, "Application of digital image processing for implementation of complex realistic particle shapes/morphologies in computer simulated heterogeneous microstructures," *Modelling and Simulation in Materials Science and Engineering,* vol. 14, pp. 351-363, Apr 2006.

[98] S. I. Lieberman, H. Singh, Y. Mao, A. Sreeranganathan, A. M. Gokhale, S. Tamirisakandala, and D. B. Miracle, "The microstructural characterization and simulation of titanium alloys modified with boron," *Jom,* vol. 59, pp. 59-63, Jan 2007.

[99] Y. Mao and A. M. Gokhale, "Unpublished Research," Atlanta: Georgia Institute of Technology, 2008.

[100] S. Tamirisakandala, R. B. Bhat, D. J. McEldowney, and D. B. Miracle, "Strength Modeling of a Titanium Alloy Modified with Boron and Boron+Carbon," in *Materials Science and Technology*, Chicago, IL, United States, 2003, pp. 185-194.

[101] J. L. Hay and G. M. Pharr, "Instrumented Indentation Testing," in *ASM Handbook Volume 8: Mechanical Testing and Evaluation*, H. Kuhn and D. Medlin, Eds. Ohio: ASM International, 2000, pp. 232-243.

[102] Y. T. Cheng and C. M. Cheng, "Scaling, dimensional analysis, and indentation measurements," *Materials Science & Engineering R-Reports,* vol. 44, pp. 91-149, AUG 1 2004.

[103] X. Chen, N. Ogasawara, M. Zhao, and N. Chiba, "On the uniqueness of measuring elastoplastic properties from indentation: The indistinguishable mystical materials," *Journal of the Mechanics and Physics of Solids,* vol. 55, pp. 1618-1660, 2007.

[104] Z. H. Gan, G. Q. Yu, Z. W. Zhao, C. M. Tan, and B. K. Tay, "Mechanical properties of zirconia thin films deposited by filtered cathodic vacuum arc," *Journal of the American Ceramic Society,* vol. 88, pp. 2227-2229, Aug 2005.

[105] A. E. Giannakopoulos and S. Suresh, "Determination of elastoplastic properties by instrumented sharp indentation," *Scripta Materialia,* vol. 40, pp. 1191-1198, APR 23 1999.
[106] M. Dao, N. Chollacoop, K. J. Van Vliet, T. A. Venkatesh, and S. Suresh, "Computational modeling of the forward and reverse problems in instrumented sharp indentation," *Acta Materialia,* vol. 49, pp. 3899-3918, NOV 14 2001.
[107] Z. Shan and A. M. Gokhale, "Utility of micro-indentation technique for characterization of the constitutive behavior of skin and interior microstructures of die-cast magnesium alloys," *Materials Science and Engineering A,* vol. 361, p. 267, 2003.
[108] Y. P. Cao, X. Q. Qian, and N. Huber, "Spherical indentation into elastoplastic materials: Indentation-response based definitions of the representative strain," *Materials Science and Engineering a-Structural Materials Properties Microstructure and Processing,* vol. 454, pp. 1-13, Apr 25 2007.
[109] Y. T. Cheng and C. M. Cheng, "Can stress-strain relationships be obtained from indentation curves using conical and pyramidal indenters?," *Journal of Materials Research,* vol. 14, pp. 3493-3496, SEP 1999.
[110] K. K. Tho, S. Swaddiwudhipong, Z. S. Liu, K. Zeng, and J. Hua, "Uniqueness of reverse analysis from conical indentation tests," *Journal of Materials Research,* vol. 19, pp. 2498-2502, Aug 2004.
[111] S. Swaddiwudhipong, K. K. Tho, Z. S. Liu, and K. Zeng, "Material characterization based on dual indenters," *International Journal of Solids and Structures,* vol. 42, pp. 69-83, Jan 2005.
[112] *Abaqus Documentation*: Dassault Systèmes, 2007.
[113] K. D. Bouzakis, N. Michailidis, and G. Erkens, "Thin hard coatings stress-strain curve determination through a FEM supported evaluation of nanoindentation test results," *Surface & Coatings Technology,* vol. 142, pp. 102-109, Jul 2001.
[114] Y. Huang, S. Qu, K. C. Hwang, M. Li, and H. Gao, "A conventional theory of mechanism-based strain gradient plasticity," *International Journal of Plasticity,* vol. 20, pp. 753-782, 2004.
[115] M. J. Puttock and E. G. Thwaite, "Elastic compression of spheres and cylinders at point and line contact," *National Standards Laboratory Technical Paper No. 25*: Commonwealth Scientific and Industrial Research Organization, Australia, 1969.
[116] A. K. Bhattacharya and W. D. NIX, "Finite-Element Simulation of Indentation Experiments," *International Journal of Solids and Structures,* vol. 24, pp. 881-891, 1988.
[117] N. Chollacoop, M. Dao, and S. Suresh, "Depth-sensing instrumented indentation with dual sharp indenters," *Acta Materialia,* vol. 51, pp. 3713-3729, Aug 1 2003.
[118] M. Beghini, L. Bertini, and V. Fontanari, "Evaluation of the stress-strain curve of metallic materials by spherical indentation," *International Journal of Solids and Structures,* vol. 43, pp. 2441-2459, Apr 2006.
[119] Z. H. Xu and D. Rowcliffe, "Finite element analysis of substrate effects on indentation behaviour of thin films," *Thin Solid Films,* vol. 447, pp. 399-405, Jan 30 2004.

[120] S. Gorsse and D. B. Miracle, "Mechanical properties of Ti-6Al-4V/TiB composites with randomly oriented and aligned TiB reinforcements," *Acta Materialia,* vol. 51, pp. 2427-2442, May 23 2003.
[121] K. B. Panda and K. S. R. Chandran, "First principles determination of elastic constants and chemical bonding of titanium boride (TiB) on the basis of density functional theory," *Acta Materialia,* vol. 54, pp. 1641-1657, Apr 2006.
[122] S. I. Lieberman, "Microstructural Characterization, Visualization, and Simulation of Ti-B Materials," Ph.D. Dissertation, Georgia Institute of Technology, Atlanta, 2007.
[123] *Engineered Materials Handbook Vol. 4: Ceramics and Glasses*. Metals Park, Ohio: ASM International, 1991.
[124] H. Singh, "Computer Simulations of Realistic Microstructures: Implications for Simulation based Materials Design," Ph.D. Dissertation, Georgia Institute of Technology, Atlanta, 2008.
[125] S. Swaminathan, S. Ghosh, and N. J. Pagano, "Statistically equivalent representative volume elements for unidirectional composite microstructures: Part I - Without damage," *Journal of Composite Materials,* vol. 40, pp. 583-604, 2006.
[126] J. E. Spowart, "Unpublished Research," Air Force Research Laboratory, 2008.
[127] "Simpleware - converting 3D images into numerical models (http://www.simpleware.com)," 2008.
[128] A. Abdul-Aziz, G. Limbert, P. G. Young, and T. Beresford-West, "Using ABAQUS with 3D Imaging Techniques for Material Characterization," in *Abaqus Users' Conference*, Paris, France, 2007.
[129] C. E. Catlett, "TeraGrid: Analysis of Organization, System Architecture, and Middleware Enabling New Types of Applications," *HPC and Grids in Action*, L. Grandinetti, Ed. Amsterdam, 2007.
[130] P. M. Singh and J. J. Lewandowski, "Effects of Heat-Treatment and Reinforcement Size on Reinforcement Fracture during Tension Testing of a Sic(P) Discontinuously Reinforced Aluminum-Alloy," *Metallurgical Transactions a-Physical Metallurgy and Materials Science,* vol. 24, pp. 2531-2543, Nov 1993.
[131] R. G. Munro, "Material properties of a sintered alpha-SiC," *Journal of Physical and Chemical Reference Data,* vol. 26, pp. 1195-1203, Sep-Oct 1997.
[132] D. B. Miracle, S. L. Donaldson, and ASM International. Handbook Committee., *Composites*. Material Park, Ohio: ASM International, 2001.
[133] A. Kelly, R. W. Cahn, and M. B. Bever, *Concise encyclopedia of composite materials*, Rev. ed. Oxford, England ; New York: Pergamon, 1994.
[134] S. Tamirisakandala, "Unpublished Research," Air Force Research Laboratory, 2008.